A Fourier-Hermite Study of Dissipation in 1+1-D Models of Fusion Plasmas

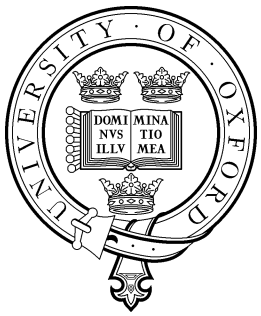

Jared Dunnmon

Oriel College

University of Oxford

A thesis submitted for the degree of

MSc. in Mathematical Modelling and Scientific Computing

Trinity 2012

Abstract

This study investigates dissipation in fusion plasmas confined by strong magnetic fields, as described by 5-D gyrokinetic theory. We first derive a reduced model for the dynamics parallel to the magnetic field in both physical and velocity spaces. This model closely resembles the classic one-dimensional Vlasov-Poisson system, but replaces Poisson's law with the quasineutrality condition relevant to multi-species fusion plasmas. We construct a numerical model using a truncated Fourier-Hermite representation, validate it against existing results for the Vlasov-Poisson system, and then apply it to fusion plasmas. Similarities and differences between the classic and fusion cases are assessed. We then investigate the effect of unsteady forcing by a neutral particle beam, representing both an actual tokamak energy source and a model for turbulence in the omitted dimensions perpendicular to the magnetic field. We find that even small amplitude forcing may substantially affect the long-time behavior, which may have important consequences in the design of efficient fusion reactors.

Acknowledgements

The author would first like to thank the many colleagues and mentors without whom this work would not have been possible. Joseph Parker's help in working through the reduction of low dimensional plasma models to Hermite space and appropriately implementing hypercollisions was critical to the success of this thesis. Moreover, the importance of Ian Abel's assistance in conceptualizing various collision operators and understanding a number of the finer points of plasma physics cannot be understated. This work is also heavily indebted to Edmund Highcock for the many hours he spent explaining the function and computational implementation of the gyrokinetic model.

The author would also like to thank the Rhodes Trust for its generous funding during both the term-time and dissertation periods. The opportunity pursue this course of study and have the chance to devote several months of time solely to this dissertation has been truly remarkable.

Finally, and most importantly, the author would like to express his gratitude to Paul Dellar, who advised this project and provided many particularly useful insights on the various ways in which the difficult physics of plasma systems can be accurately encapsulated in formal mathematical frameworks. The amount of time, effort, and intellectual energy that Paul has devoted to supporting this work is most sincerely appreciated.

Contents

List of Figures

Chapter 1

Introduction and Fundamentals

One deuterium nucleus fusing with one tritium nucleus releases 2.818×10^{-12} J of energy. One could therefore power a 1 GW generating plant with 1 kilogram of widely available hydrogen fuel per day (Wesson, 1997). Unfortunately, a fusing plasma must be maintained at temperatures around 10^8 K for the particles' kinetic energy to overcome their mutual electrostatic repulsion. Such temperatures cannot be survived by any material wall. The most common fusion reactor, the tokamak, confines the plasma using strong magnetic fields generated by both toroidal and poloidal coils. The particles are then confined to tight helical paths around the magnetic field lines within the toroidal metal shell of the tokamak. Fusion power scales as the plasma pressure, but maintaining confinement is limited by the ratio β of the fluid to magnetic pressures, which is defined as,

$$\beta \equiv \frac{8\pi n_0 k_B T_s}{B_0^2}, \tag{1.1}$$

for a particular charged species s with equilibrium particle number density n_0, temperature T_s, mean magnetic field strength B_0, and the Boltzmann constant k_B (Huba, 2009).[1] Current technology enforces distinct limits on both achievable β and reactor efficacy.

The enormous temperature difference between the core plasma and the metal walls of the tokamak tends to drive large outward heat fluxes away from the core, despite the confining magnetic field (Wesson, 1997). These losses are greatly enhanced by the turbulence that inevitably arises in tokamaks. Finding ways to suppress turbulence within tokamaks has thus become an important research goal for the fusion community. A promising method by which turbulence has been experimentally mitigated is through the development of internal transport barriers (ITBs) caused by well-ordered toroidal flow with a velocity shear in a direction perpendicular to that

[1]Symbol definitions used consistently throughout the manuscript are summarized in Appendix A.

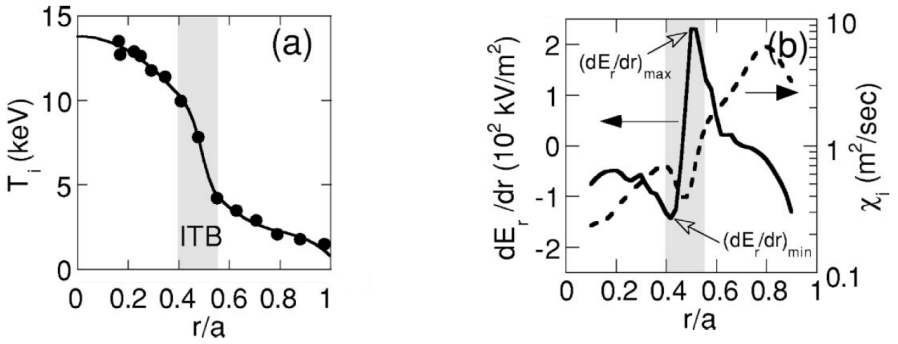

Figure 1.1: Experimental data showing an internal transport barrier (Miura et al., 2003). $1\text{eV}/k_B \sim 10^4$ K and k_B is the Boltzmann constant.

of the magnetic field lines. Figure 1.1, reproduced and slightly modified from Miura et al. (2003), shows the appearance of an ITB within the Japanese JT-60 tokamak.

These experimental data show that the substantial temperature gradient indicative of an ITB coincides with a large reversal in the gradient of the electric field. Unfortunately, current theoretical models of turbulent plasmas have not determined the mechanism by which ITBs form and evolve. The fusion community therefore puts significant effort into developing computational models for fusion plasmas instead, but at present even relatively simple flux-tube scale simulations may require hundreds of thousands of core hours.

1.1 Kinetic Theory and the Vlasov Equation

Plasmas are insufficiently collisional to justify a fluid description, and solving Newton's Second Law for N particles becomes impractical when $N \sim 10^{26}$ as in real systems. The species distribution function $f_s(\mathbf{x}, \mathbf{v}, t)$ offers a statistical description by giving the number density of particles at position $\mathbf{x}$ and time t that move with velocity $\mathbf{v}$. The number of particles $\mathrm{d}N_s$ in an element of six dimensional position-velocity phase space $\mathrm{d}\mathbf{x}\mathrm{d}\mathbf{v}$ is therefore (e.g. Dendy, 1993; Schroeder, 2000),

$$\mathrm{d}N_s = f_s(\mathbf{x}, \mathbf{v}, t)\mathrm{d}\mathbf{x}\mathrm{d}\mathbf{v}. \tag{1.2}$$

We now consider a plasma particle of a particular species s with charge q_s, mass m_s, position vector $\mathbf{x}$, and velocity vector $\mathbf{v}$ interacting with a magnetic field $\mathbf{B}$ and electric field $\mathbf{E}$. The equations of motion for the particle are,

$$\frac{\mathrm{d}\mathbf{x}}{\mathrm{d}t} = \mathbf{v}, \quad \frac{\mathrm{d}\mathbf{v}}{\mathrm{d}t} = \frac{\mathbf{F}_{EM}}{m_s} = \frac{q_s}{m_s}\left(\mathbf{E} + \frac{\mathbf{v} \times \mathbf{B}}{c}\right), \tag{1.3}$$

in Gaussian units (e.g. Griffiths, 1999) where $\mathbf{F}_{EM}$ is the Lorentz force exerted on the particle and c is the speed of light. The Vlasov equation for collisionless plasmas is equivalent to observing that $\mathrm{d}f_s/\mathrm{d}t = 0$ along a characteristic, so,

$$\frac{\mathrm{d}f_s}{\mathrm{d}t} = \frac{\partial f_s}{\partial t} + \frac{\mathrm{d}\mathbf{x}}{\mathrm{d}t} \cdot \nabla f_s + \frac{\mathrm{d}\mathbf{v}}{\mathrm{d}t} \cdot \nabla_{\mathbf{v}} f_s = 0, \tag{1.4}$$

where ∇ represents the spatial gradient and $\nabla_{\mathbf{v}}$ represents the gradient with respect to particle velocity. Substituting (1.3) into (1.4) gives the Vlasov equation as in (1.5) below,

$$\frac{\partial f_s}{\partial t} + \mathbf{v} \cdot \nabla f_s + \frac{q_s}{m_s}\left(\mathbf{E} + \frac{\mathbf{v} \times \mathbf{B}}{c}\right) \cdot \nabla_{\mathbf{v}}\, f_s = 0. \tag{1.5}$$

1.2 Collisional Plasma and the VFP Equation

In reality, all plasmas are at least weakly collisional. We therefore extend the Vlasov equation (1.5) to include a general collisionality $C[f_s]$,

$$\frac{\partial f_s}{\partial t} + \mathbf{v} \cdot \nabla f_s + \frac{q_s}{m_s}\left(\mathbf{E} + \frac{\mathbf{v} \times \mathbf{B}}{c}\right) \cdot \nabla_{\mathbf{v}}\, f_s = C[f_s]. \tag{1.6}$$

An original form of this operator was derived by Landau (1936) to describe small angle, long-range binary Coulomb interactions between Maxwellian electrons (subscript e) and an ion species (subscript i). Writing $f_i \equiv F_0 + \delta f_{1i}$ with δf_{1i} a small deviation from a background Maxwellian distribution function F_0 gives the Landau collision operator as,[2]

$$C[\delta f_{1i}] = \frac{\partial}{\partial \mathbf{v}} \cdot \int K(\mathbf{v} - \mathbf{v}')\left(\frac{1}{m_i} f_e(\mathbf{v}') \frac{\partial}{\partial \mathbf{v}} \delta f_{1i}(\mathbf{v}) - \frac{1}{m_e} \delta f_{1i}(\mathbf{v}) \frac{\partial}{\partial \mathbf{v}'} f_e(\mathbf{v}')\right) \mathrm{d}\mathbf{v}', \tag{1.7}$$

where $K(\mathbf{v} - \mathbf{v}') = (2\pi q_e^2 q_i^2 \log\Lambda / m_i)(I - \hat{\mathbf{g}}\hat{\mathbf{g}})/|\mathbf{g}|$ with $\log\Lambda$ the Coulomb logarithm,[3] $\mathbf{g} = \mathbf{v} - \mathbf{v}'$, and $\hat{\mathbf{g}}$ the analogous unit vector (e.g. Parker and Dellar, 2012). Equation (1.7) can be simplified in a single dimension using the well-known Fokker-Planck operator to give (Lénard and Bernstein, 1958; Parker and Dellar, 2012),

$$C[\delta f_{1i}] = \frac{\partial}{\partial v}\left(\mathcal{D}(f_e) \frac{\partial}{\partial v} \delta f_{1i} - \mathcal{F}(f_e) \delta f_{1i}\right), \tag{1.8}$$

where $\mathcal{D}$ is a diffusion coefficient and $\mathcal{F}$ is a friction coefficient. The first term in the collision operator represents the tendency of collisions to widen the range of velocities

[2] The reader is referred to (1.20) for an explicit definition Maxwellian distribution function.

[3] The Coulomb logarithm term expresses the relative efficacy of small and large angle collisions. More details on this parameter can be found in Huba (2009).

occupied by the plasma particles while the second term represents the movement of all particle velocities towards the mean particle velocity (Liboff, 2003; Thomas et al., 2012). When $C[f_s]$ for a general charged species s is defined in the form of (1.8), the resulting form of (1.6) is known as the Vlasov-Fokker-Planck (VFP) equation. The VFP equation is important in contemporary plasma physics because it represents a reasonably tractable model for the time evolution of a collisional distribution function.

Generally, $\mathcal{D}$ and $\mathcal{F}$ are complicated integral expressions that make the Fokker-Planck version of the analytic Landau collision operator difficult to work with. A useful simplification proposed by Lénard and Bernstein (1958) puts $\mathcal{D} = \nu/2$ and $\mathcal{F} = -\nu v$ with an overall collision frequency ν such that (1.8) becomes,

$$C[\delta f_{1i}] = \nu \frac{\partial}{\partial v}\left(v\delta f_{1i} + \frac{1}{2}\frac{\partial \delta f_{1i}}{\partial v}\right). \tag{1.9}$$

Dougherty (1964) further adjust the Lénard-Bernstein operator to conserve both momentum and energy,

$$C[f_i] = \nu \frac{\partial}{\partial v}\left((v - u[f_i])\, f_i + T[f_i]\frac{\partial f_i}{\partial v}\right), \tag{1.10}$$

where the bulk velocity u and temperature T are defined below for a general charged species s in terms of moments of the distribution function (Parker and Dellar, 2012),

$$u[f_s] = \frac{1}{n}\int_{-\infty}^{\infty} v f_s \mathrm{d}v, \quad T[f_s] = \frac{1}{n}\int_{-\infty}^{\infty} (v-u)^2 f_s \mathrm{d}v, \quad n[f_s] = \int_{-\infty}^{\infty} f_s \mathrm{d}v. \tag{1.11}$$

Finally, the linearized version of this Dougherty operator is (Parker and Dellar, 2012),

$$C[\delta f_{1i}] = \nu \frac{\partial}{\partial v}\left(\frac{1}{2}\frac{\partial \delta f_{1i}}{\partial v} + v\delta f_{1i} + T[\delta f_{1i}]\frac{\partial F_0}{\partial v} - u[\delta f_{1i}]F_0\right). \tag{1.12}$$

We will use a linearized Dougherty collision operator of the form (1.12) in all the computational models we present here.

1.3 Landau Damping

The Vlasov and VFP equations are quite important for a number of reasons, and motivate the present study by means of a classic prediction about dissipation in plasmas. A 20^{th} century analysis of the Vlasov equation by Landau (1946) reveals that the electric field within a plasma decays in time, even in the apparent absence of collisions. This phenomenon is so important in understanding plasma dissipation that we present a brief derivation in the original style of Landau (1946). We consider

a single-species electron plasma with a background of immobile heavy ions to provide overall charge neutrality. Under this assumption that ions are quite massive and therefore fixed with respect to the small electrons, we realize that electron plasma waves will dominate the high frequency dynamics of this system. We also assume classical electrostatic coupling of the Vlasov equation to Poisson's law for an electric field (Chen, 1984). This oft-studied closure is known as the Vlasov-Poisson (V-P) system. The theory of Landau damping in this system has been studied extensively, most notably in the 170 page paper "On Landau Damping" by Mouhot and Villani (2011) that establishes the functional-analytic machinery for the collisionless limit.

1.3.1 Collisionless Landau Damping

To begin, we wish to analyze the behavior of a perturbation δf_{1e} to a background electron distribution function F_0. We assume that the zeroth order components of the electric field and magnetic field, $\mathbf{E}_0$ and $\mathbf{B}_0$, are negligible. Working in a single dimension allows us to write the linearized distribution function as,

$$f_e(x, v, t) = F_0(v, t) + \delta f_{1e}(x, v, t), \tag{1.13}$$

where δf_{1e} is an $O(\epsilon)$ perturbation to the normalized equilibrium distribution function F_0 with $\epsilon \ll 1$. The cross product term in (1.5) vanishes in a single dimension in both position and velocity space, henceforth referred to as a "1+1-D" framework, so we can write the linearized Vlasov equation for electrons as,

$$\frac{\partial \delta f_{1e}}{\partial t} + v\frac{\partial \delta f_{1e}}{\partial z} - \frac{eE_z}{m_e}\frac{\partial F_0}{\partial v} = 0, \tag{1.14}$$

where e is the electron charge modulus, E_z is the parallel electric field, and $q_e = -e$. We consider plane waves in the z direction such that (Chen, 1984),

$$\delta f_{1e} \sim e^{i(kz-\omega t)}, \tag{1.15}$$

where k is the wavenumber and ω the frequency. Combining (1.14) and (1.15) gives,

$$-i\omega\delta f_{1e} + ikv\delta f_{1e} = \frac{eE_z}{m_e}\frac{\partial F_0}{\partial v}, \tag{1.16}$$

which immediately leads to an expression for δf_{1e},

$$\delta f_{1e} = \frac{ieE_z}{m_e}\frac{\partial F_0}{\partial v}\frac{1}{\omega - kv}. \tag{1.17}$$

We now express the electrostatic coupling through Poisson's law as (Chen, 1984),

$$\nabla \cdot E_z = \frac{\partial E_z}{\partial z} = ikE_z = -4\pi e n_{1e} = -4\pi e \int_{-\infty}^{\infty} \delta f_{1e} \mathrm{d}v, \tag{1.18}$$

where n_{1e} is the perturbed electron particle density. Combining (1.17) and (1.18) and taking F_0 as normalized such that $n_0 = \int_{-\infty}^{\infty} F_0 \mathrm{d}v = 1$ then gives,

$$1 = -\frac{4\pi n_0 e^2}{k m_e} \int_{-\infty}^{\infty} \frac{\partial F_0/\partial v}{\omega - kv} \mathrm{d}v = \frac{\omega_p^2}{k^2} \int_{-\infty}^{\infty} \frac{\partial F_0/\partial v}{v - \frac{\omega}{k}} \mathrm{d}v, \tag{1.19}$$

where we take $\omega_p \equiv \sqrt{4\pi n_0 e^2/m_e}$ as the electron plasma frequency (Chen, 1984; Huba, 2009). We also define F_0 as the Maxwellian distribution F_M,

$$F_0 \equiv F_M = \sqrt{\frac{m_e}{2\pi k_B T_e}} e^{-m_e v^2/2k_B T_e} = \frac{1}{v_{th_e}} \pi^{-1/2} e^{-v^2/v_{th_e}^2}. \tag{1.20}$$

This Maxwellian distribution is normalized with respect to the electron thermal velocity $v_{th_e} = \sqrt{2k_B T_e/m_e}$.[4] Evaluating the integral in (1.19) requires a great deal of care due to the singularity at $v = \omega/k$ and the fact that ω may be complex. Effectively, we must integrate along the entirety of the real v axis, but must also deform this path below the pole to form the Landau contour. The exact reasons for this contour choice, which involve the effect of collisions and ensuring continuity of the dispersion relation, are discussed in the following section.

A useful tool in working with integrals of the form (1.19) is the plasma dispersion function,

$$Z(\zeta) = \frac{1}{\sqrt{\pi}} \int_{-\infty}^{\infty} \frac{e^{-x^2}}{x - \zeta} \mathrm{d}x, \tag{1.21}$$

which has been studied extensively in the literature in the context of Hilbert transforms (Fried and Conte, 1961; Huba, 2009). Combining (1.19) and (1.20) while changing variables to $u \equiv v/v_{th_e}$ and $\zeta \equiv \omega/kv_{th_e}$ allows us to express (1.19) in terms of the dispersion function as,[5]

$$1 = \left(\frac{\omega_p^2}{k^2 v_{th_e}^2}\right) \left(-2\left[1 + \zeta Z(\zeta)\right]\right). \tag{1.22}$$

The dispersion relation (1.22) can be solved numerically, which will become useful in later validating our computational model of electrostatically coupled Vlasov systems. It is also instructive to look at a series approximation for the weak damping

[4] Many define v_{th_s} for a general charged species s as we do here, but others take $v_{th_s} = \sqrt{k_B T_s/m_s}$, which leads to differences by a factor of two between our results and some of those in the literature.

[5] Details of expressing (1.19) using the plasma dispersion function may be found in Appendix B.1.

regime that characterizes many plasmas. We therefore assume that $|\zeta| \gg 1$ and that $|\mathrm{Im}(\omega)| \ll |\mathrm{Re}(\omega)|$, which allows us to utilize a known asymptotic expansion of $Z(\zeta)$ for $|\zeta| \gg 1$ and $|\mathrm{Im}(\zeta)| < |\mathrm{Re}(\zeta)^{-1}|$ (Fried and Conte, 1961; Huba, 2009),

$$Z(\zeta) = i\pi^{1/2} e^{-\zeta^2} - \zeta^{-1} \left(1 + \frac{1}{2\zeta^2} + \frac{3}{4\zeta^4} + ...\right). \tag{1.23}$$

Truncating the expansion after the first three terms and performing further manipulations detailed in Appendix B.2 yields the following well-known results (Chen, 1984),

$$\mathrm{Re}(\omega) \approx \sqrt{\omega_p^2 + \frac{3}{2} k^2 v_{th_e}^2}, \tag{1.24a}$$

$$\mathrm{Im}(\omega) \equiv \gamma \approx -\pi^{1/2} \omega_p \left(\frac{\omega_p}{k v_{th_e}}\right)^3 e^{-\omega_p^2/k^2 v_{th_e}^2} e^{-3/2}. \tag{1.24b}$$

Because the sign of the growth rate γ is negative, we reach the distinctly counterintuitive conclusion that electron plasma waves are always damped even in the apparent absence of collisions. This phenomenon, formally known as "Landau damping," is critically important both in understanding basic plasma dynamics and in assessing the accuracy of our plasma models in later sections.

1.3.2 Landau Damping with Krook Collisions

An important adjustment to the analysis of Section 1.3.1 occurs when we we assume collisions with neutral particles. We can write a simplified collision operator in the Krook framework as (Bhatnagar et al., 1954),

$$C[f_e] = \nu \left(f_n - f_e\right), \tag{1.25}$$

where f_n is the distribution function of neutral particles and ν is a constant collision frequency. When we assume that $f_n = F_0 = F_M$, take $f_e = F_0 + \delta f_{1e}$, and substitute (1.25) into (1.6), we arrive at the following equation describing the collisional plasma,

$$\frac{\partial \delta f_{1e}}{\partial t} + \mathbf{v} \cdot \nabla \delta f_{1e} + \frac{q_e}{m_e} \left(\mathbf{E} + \frac{\mathbf{v} \times \mathbf{B}}{c}\right) \cdot \nabla_{\mathbf{v}} \ (F_0 + \delta f_{1e}) = -\nu \delta f_{1e}. \tag{1.26}$$

We can see that the analysis to determine the frequency and growth rate resultant from collisional Landau damping will differ from that in Section 1.3.1 by the additional term $-\nu \delta f_{1e}$. The reader can find a full analysis of this case in the work of Platzman and Buchsbaum (1961). To summarize, the Krook collision term causes the dispersion relation to become (Platzman and Buchsbaum, 1961),

$$1 = \frac{\omega_p^2}{k^2} \int_{-\infty}^{\infty} \frac{\partial F_0 / \partial v}{v - \frac{\omega}{k} - \frac{i\nu}{k}} \mathrm{d}v, \tag{1.27}$$

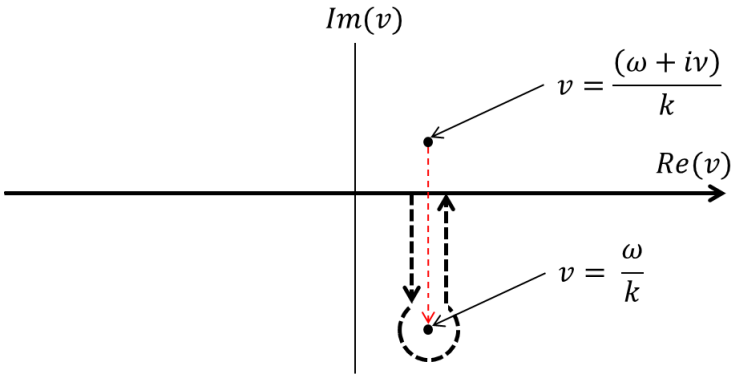

Figure 1.2: The Landau contour and collisional pole shifting. The bold black line indicates the path while the pole is above the real axis while the dashed line indicates the contour extension when the pole is below the real axis. The red arrow indicates the small collisionality limit as $\nu \to 0$.

which effectively shifts the integral pole from $v = \omega/k$ to $v = (\omega + i\nu)/k$, as shown in Fig. 1.2, along with the analogous Landau contours. The Landau contour is always on the same side of the pole as enforced by a physical argument requiring continuity of the dispersion relation under continuous variation of the collision frequency (Lifshitz and Pitaevskii, 1981). This contour goes under rather than over the pole to yield physically relevant decaying modes as opposed to growing modes. Thus, while the Landau contour ensures continuity of the dispersion relation with collisionality, it also destroys system reversibility because the time-reversed system requires a different contour going over the pole. This conclusion represents one of the most powerful, yet intuitively difficult results in plasma physics.

The weakly collisional limit $\nu \to 0$ represents a vexing physical question because a full analysis of linear Landau damping (e.g. Platzman and Buchsbaum, 1961) indicates that this limit represents a singular perturbation. In other words, the plasma actually behaves quite differently under the assumption of zero collisions as opposed to when one takes the small collisionality limit. This has a number of repercussions for numerical models. As collisionality tends to zero, arbitrarily fine structures develop in velocity space to the point that they cannot be resolved on a particular fixed velocity space grid. Hence, discrete numerical approximations require that any structures finer than the shortest resolved scales be eliminated by a minimum level of collisionality (Ng et al., 2006; Parker and Dellar, 2012).

Fortunately, our Fokker-Planck based collision operator ensures that our solution is both continuous and well resolved. Firstly, because $C[f_s] \sim \nu(\partial^2 f_s/\partial v^2)$ in the Fokker-Planck case for a general charged species s, we know that fine velocity space

scales in f_s are diffused out by the second derivative term. More specifically, a boundary layer of width $\nu^{1/2}$ will form in velocity space, within which collisions still have $O(1)$ effects even as $\nu \to 0$ (Ng et al., 2006). This operator thus mimics the behavior of integrating over the Landau contour by ensuring continuity of the dispersion relation with respect to collisionality.

1.4 Gyrokinetics, Forcing, and Multiple Species

Landau damping theory was originally formulated for the single species electron plasma described by the V-P system, and good numerical benchmark solutions exist for this case (e.g. Heath et al., 2012). We therefore use these results to validate the numerical model we develop here before turning to a similar but slightly different system relevant to two-species fusion plasmas. All multi-species analyses we present in this study consider a simple, yet very relevant two-species ion-electron plasma where the ion charge q_i is defined as $q_i = -q_e = e$. We focus on this type of plasma because it inevitably forms as hydrogen fuels undergo nuclear fusion. We also assume that electrons in such a plasma are adiabatic and thus follow a Boltzmann distribution $f_e = F_0 e^{-q_e \Phi / k_B T_e}$ with Φ the electric potential (Hae-Kwan, 2011). Such assumptions will become crucial as we work to create simple, yet precise models of fusion plasmas.

We formulate our model for simple two-species fusion plasmas by reducing the common 5-D gyrokinetic model for multidimensional plasmas to a single dimension in both position and velocity space. This approach is motivated by the proposition that plasma forcing by interaction with fast-moving neutral particles might be able to mitigate the development of turbulence and cause ITBs to form. Investigating this idea in full 5-D gyrokinetics, however, can be both computationally expensive and complicated enough that the fundamental physical interpretations may become difficult to formulate. The current study attempts to mathematically investigate how neutral particle forcing affects energy dissipation in plasmas by looking at a reduction of the gyrokinetic model in a single velocity dimension and a single space dimension, which we refer to as the "1+1-D" model. As we will show, appropriate simplification and normalization of the gyrokinetic modeling equations results in a 1+1-D framework that is well described by an electrostatic Vlasov system. It is hoped that investigating the dynamics of such a 1+1-D system for a simple two-species plasma will give useful preliminary insight into how neutral particle forcing might affect the behavior of a full 5-D gyrokinetic simulation and, importantly, if such a forcing mechanism might potentially represent a method by which ITBs can be established in tokamak reactors.

Chapter 2

The Gyrokinetic Model

While the single-species 1+1-D V-P system is used in classical studies of Landau damping, a more complex model is necessary to describe multi-species fusion plasmas. Gyrokinetic theory represents a contemporary framework for understanding the behavior of multidimensional plasmas that is made computationally tractable through filtering out the fastest of three characteristic timescales and by reducing the dimensionality of the system from six (three velocity and three position) to five (two velocity and three position) in phase space. The derivation of this gyrokinetic model requires consideration of motions on several different scales. The concept of gyroaveraging over fast-timescale Larmor gyrations about the magnetic field lines is central to the idea of gyrokinetics. Much of the original mathematical work on this technique represents an application of the earlier guiding-center theory due to Littlejohn (1983).

In this chapter, we present a brief derivation of the Gyrokinetic-Maxwell (GK-M) system describing the time evolution of an electromagnetically coupled multidimensional plasma. We show that reducing the GK-M system for a simple two-species plasma to an electrostatic 1+1-D framework in the direction parallel to the magnetic field gives a system similar to the V-P system whose behavior we can investigate using the numerical models we work with in the majority of this study. The formalism in the following presentation is heavily indebted to that of Howes et al. (2006). The author has chosen to maintain notational similarity to Howes et al. (2006) because these exact statements were used by Numata et al. (2010) in the development of the commonly used AstroGK gyrokinetic code.[1] The gyrokinetic model is originally due to Frieman and Chen (1982), while Howes et al. (2006) and Abel et al. (2012) present significant work in the context of astrophysical plasmas and tokamak reactors, respec-

[1]Note that the author spent a significant amount of time learning to use AstroGK during this study and intends to use the results presented here to inform further work in AstroGK at a later date.

tively. Krommes (2012) contains a thorough survey of these models detailing theory, numerics, and physical consequences.

2.1 Assumptions and Ordering

An important aspect of the gyrokinetic description of a plasma is the basic physical assumptions we make about the system and how well these assumptions apply to the actual situations we hope to model. Gyrokinetic theory arises in a distinguished limit in which many dimensionless ratios scale with a single small parameter ϵ.

2.1.1 Fundamental Physical Assumptions

A single charged particle of species s in a strong magnetic field will gyrate around the magnetic field lines at a distance defined by the Larmor radius (or gyroradius) ρ_s and a rate described by the gyrofrequency (or cyclotron frequency) Ω_s. Gyrokinetics describes the motion of many weakly collisional charged particles in a strong magnetic field, and requires several formal assumptions. Firstly, we define a "strong" magnetic field to be one for which the gyroradius is much smaller than a characteristic macroscopic device length L,

$$\rho_s \equiv \frac{v_{th_s}}{\Omega_s} \ll L, \tag{2.1}$$

where ρ_s is expressed in terms of the thermal velocity v_{th_s}, the gyrofrequency, and the mean magnetic field strength B_0,

$$v_{th_s} = \sqrt{2k_B T_s/m_s}, \quad \Omega_s = q_s B_0/m_s c. \tag{2.2}$$

The second important physical assumption is that the frequency ω of turbulent fluctuations is much slower than the gyrofrequency,

$$\omega \ll \Omega_s. \tag{2.3}$$

The assumptions of (2.1) and (2.3) are the underpinnings of the gyrokinetic model. Specifically, they allow us to separate the fast system evolution due to gyromotion from the slower evolution of the parallel fluctuating quantities by averaging out the gyromotion (Abel et al., 2012). This simplification both eliminates many fast timescale dynamics and permits a reduction from a six dimensional position-velocity phase space to a five dimensional space with three position dimensions and two velocity dimensions (Frieman and Chen, 1982; Howes et al., 2006).

2.1.2 The Gyrokinetic Ordering

We now define a specific set of orderings with respect to physical parameters that allows us to derive gyrokinetic theory as a distinguished limit from the VFP equation. Each order of expansion of the VFP equation in ϵ will reveal important information about the plasma under consideration, and ultimately the "gyrokinetic equation" will arise from the highest order terms we consider here. We first order the spatial length scales in a manner that separates gyromotion from slower system dynamics. We define a the small parameter ϵ such that,

$$\epsilon = \frac{\rho_s}{l_0} \ll 1, \tag{2.4}$$

where l_0 represents the characteristic wavelength of fluctuations in the direction parallel to the magnetic field lines (Howes et al., 2006). In the case of a tokamak reactor, l_0 may be taken to be the minor radius of the torus (Abel et al., 2012). The same parameter ϵ also governs the temporal scaling between the fastest two timescales under consideration here. Taking the timescale ω of turbulent fluctuations to be defined by the thermal velocity v_{th_s} and the length scale l_0, (2.1), (2.3), and (2.4) give,

$$\omega \sim \frac{v_{th_s}}{l_0} \sim \Omega_s \frac{\rho_s}{l_0} \sim \epsilon \Omega_s. \tag{2.5}$$

The timescale of the turbulent fluctuations is thus $O(\epsilon)$ compared to the gyrofrequency of spiraling around magnetic field lines. The third, and slowest, timescale in this problem determines the rate at which changes to the equilibrium distribution function occur. This timescale, τ, is set by the rate of overall heat transfer on the device scale, as governed by the turbulent thermal diffusivity α. We follow Abel et al. (2012) and estimate $\alpha \sim \rho_s^2 \omega$ using a mixing length argument,[2]

$$\frac{1}{\tau} \sim \frac{\alpha}{l_0^2} \sim \frac{\rho_s^2 \omega}{l_0^2} \sim \frac{\omega}{\Omega_s} \left(\frac{\rho_s}{l_0}\right)^2 \Omega_s \sim \epsilon^2 \omega \sim \epsilon^3 \Omega_s. \tag{2.6}$$

We now expand the distribution function into a spatially homogeneous equilibrium portion (denoted by the subscript zero) and parts that fluctuate at the turbulent frequency ω with successively smaller amplitudes in ϵ. We denote fluctuating quantities by the prefix δ and quantities of $O(\epsilon^n)$ by a subscript n. The expansion for f_s in the relatively simple case characterized by a homogeneous equilibrium ($\nabla F_0 = 0$) and a constant mean magnetic field ($\mathbf{B}_0 = \mathrm{B}_0 \hat{\mathbf{z}}$) in a periodic box is thus,

$$f_s(\mathbf{x}, \mathbf{v}, t) = F_0(\mathbf{v}, t) + \delta f_{1s}(\mathbf{x}, \mathbf{v}, t) + \delta f_{2s}(\mathbf{x}, \mathbf{v}, t) + \ldots \,. \tag{2.7}$$

[2]This estimate ultimately comes from the concept of gyro-Bohm diffusion as discussed by Dimits et al. (2000). The ϵ order of the heating timescale is checked in Appendix B of Howes et al. (2006).

The electromagnetic fields may be similarly decomposed into equilibrium and fluctuating parts, but the order of these fluctuations is as yet undetermined. We represent the fluctuating parts using a scalar potential Φ and a vector potential $\mathbf{A}$,

$$\mathbf{B}(\mathbf{x},t) = \mathbf{B}_0 + \delta\mathbf{B}(\mathbf{x},t) = B_0\hat{\mathbf{z}} + \nabla\times\mathbf{A}, \tag{2.8}$$

$$\mathbf{E}(\mathbf{x},t) = \mathbf{E}_0 + \delta\mathbf{E}(\mathbf{x},t) = \delta\mathbf{E}(\mathbf{x},t) = -\nabla\Phi - \frac{1}{c}\frac{\partial\mathbf{A}}{\partial t}, \tag{2.9}$$

where $\hat{\mathbf{z}}$ is the direction parallel to the magnetic field lines and we have assumed $\mathbf{E}_0 = 0$ (Howes et al., 2006). This representation automatically satisfies the two homogeneous Maxwell equations and conveniently transforms the remaining ones. Moreover, assuming that the background electric field $\mathbf{E}_0$ is zero reflects the behavior of many real systems. We also impose the Coulomb gauge condition $\nabla\cdot\mathbf{A} = 0$.

2.1.3 Formal Statement of Gyrokinetic Assumptions

We now utilize the gyrokinetic ordering developed above to precisely define the assumptions that form the basis of this modeling framework. To ensure small fluctuations about the equilibrium of any quantity in the system, we assume that,

$$\frac{\delta f_{1s}}{F_0} \sim \frac{\delta\mathbf{B}}{B_0} \sim \frac{\delta\mathbf{E}}{(v_{th_s}/c)B_0} \sim \epsilon. \tag{2.10}$$

Effectively, the above definition states that the fluctuating portion of the distribution function or magnetic field is of $O(\epsilon)$ compared to the background equilibrium quantity. The electric field is treated as in Abel et al. (2012), where the scaling $\delta\mathbf{E}/(B_0 v_{th_s}/c) \sim O(\epsilon)$ results naturally from the form of the Lorentz force in (1.3). Next, we require the equilibrium distribution function to vary on a long time scale as set by the characteristic heating time of the system, which (2.6) shows to be of $O(\epsilon^2)$ relative to ω,

$$\frac{1}{F_0}\frac{\partial F_0}{\partial t} \sim O\left(\frac{1}{\tau}\right) \sim \epsilon^2\omega. \tag{2.11}$$

We also require all fluctuating quantities to vary with the turbulent frequency ω,

$$\omega \sim \frac{1}{\delta f_{1s}}\frac{\partial\delta f_{1s}}{\partial t} \sim \frac{1}{|\delta\mathbf{B}|}\frac{\partial\delta\mathbf{B}}{\partial t} \sim \frac{1}{|\delta\mathbf{E}|}\frac{\partial\delta\mathbf{E}}{\partial t} \sim \frac{v_{th_s}}{l_0} \sim \epsilon\Omega_s. \tag{2.12}$$

The ordering of ω at $O\left(v_{th_s}/l_0\right)$ is a direct consequence of (2.5). This ordering ensures that turbulent fluctuations are slow compared to the fast gyromotion that will ultimately be averaged out, but fast compared to the thermal transport timescale that defines the evolution of the equilibrium.

The existence of a strong magnetic field causes significant anisotropy about the magnetic field lines. In particular, turbulence will develop in such a way that the characteristic length scale of fluctuations along the magnetic field lines is significantly longer than that of fluctuations perpendicular to the magnetic field. We define these assumptions in terms of parallel and perpendicular wavenumbers, $k_\parallel$ and $k_\perp$, since $k_\perp$ should be on the order of the inverse gyroradius, ρ_s, while $k_\parallel$ should be on the order of the inverse of the turbulent length scale l_0. Thus, following Howes et al. (2006), we order $k_\parallel$ and $k_\perp$ as,

$$k_\parallel \sim \frac{\hat{\mathbf{z}} \cdot \nabla \delta f_s}{\delta f_s} \sim \frac{\hat{\mathbf{z}} \cdot \nabla \delta \mathbf{B}}{|\delta \mathbf{B}|} \sim \frac{\hat{\mathbf{z}} \cdot \nabla \delta \mathbf{E}}{|\delta \mathbf{E}|} \sim \frac{1}{l_0}, \tag{2.13}$$

$$k_\perp \sim \frac{\hat{\mathbf{z}} \times \nabla \delta f_s}{\delta f_s} \sim \frac{\hat{\mathbf{z}} \times \nabla \delta \mathbf{B}}{|\delta \mathbf{B}|} \sim \frac{\hat{\mathbf{z}} \times \nabla \delta \mathbf{E}}{|\delta \mathbf{E}|} \sim \frac{1}{\rho_s}, \tag{2.14}$$

where $\hat{\mathbf{z}}$ represents the unit vector along the mean magnetic field lines. Comparing (2.13) and (2.14) shows that parallel fluctuations have $O(\epsilon)$ wavenumbers with respect to perpendicular wavenumbers,

$$\frac{k_\parallel}{k_\perp} \sim \frac{\rho_s}{l_0} \sim \epsilon. \tag{2.15}$$

Again, this assumption will become crucially important in allowing us to eventually reduce the order of the dynamical system by averaging out the gyromotion. A final useful assumption is that all collision frequencies ν for quantities that vary on $O(1)$ in velocity (e.g. the Maxwellian distribution) are comparable to ω,

$$\nu \sim \omega \sim \epsilon \Omega_s, \tag{2.16}$$

so the collisionality in a gyrokinetic system occurs on the turbulent timescale. This completes our formal statement of the gyrokinetic ordering, the key results being,

$$\frac{\rho_s}{l_0} \sim \frac{\omega}{\Omega_s} \sim \frac{\delta f_{1s}}{F_0} \sim \frac{\delta \mathbf{B}}{B_0} \sim \frac{\delta \mathbf{E}}{(v_{th_s}/c) B_0} \sim \frac{k_\parallel}{k_\perp} \sim \epsilon \ll 1. \tag{2.17}$$

This ordering will allow us to extract the gyrokinetic modeling equations as a distinguished limit from the Vlasov equation.

2.2 Maxwell's Equations and Simplification

We now use the above orderings to write down Maxwell's equations in the form that is best suited to the gyrokinetic framework after making several simplifying assumptions. We choose, for instance, to neglect spatial scales upon which charge

separation occurs. Physically, this means that we require the perpendicular length scale to be large compared to the Debye length $\lambda_{De} = \sqrt{k_B T_e / 4\pi n_e e^2}$, which is the scale on which charges are shielded (Chen, 1984; Howes et al., 2006). Thus, we formally require,

$$k_\perp^2 \lambda_{De}^2 \ll 1. \tag{2.18}$$

Similarly, we prescribe a non-relativistic system such that,

$$\frac{v_{th_s}^2}{c^2} \ll 1. \tag{2.19}$$

Assumptions (2.18) and (2.19) are generally satisfied in modern fusion systems (Abel et al., 2012). We also define the charge density $\hat{\rho}$, which represents the total charge per unit physical volume, and the total current density $\hat{\mathbf{j}}$, which represents the total current per unit of physical volume, using integrals of f_s (Abel et al., 2012),

$$\hat{\rho} = \sum_s q_s \int f_s \mathrm{d}^3\mathbf{v}, \tag{2.20}$$

$$\hat{\mathbf{j}} = \sum_s q_s \int f_s \mathbf{v} \mathrm{d}^3\mathbf{v}. \tag{2.21}$$

Invoking (2.19), we then state the non-relativistic pre-Maxwell equations as,

$$\nabla \cdot \mathbf{E} = 4\pi\hat{\rho}, \tag{2.22a}$$

$$\nabla \cdot \mathbf{B} = 0, \tag{2.22b}$$

$$\frac{\partial \mathbf{B}}{\partial t} = -c\nabla \times \mathbf{E}, \tag{2.22c}$$

$$\nabla \times \mathbf{B} = \frac{4\pi}{c}\hat{\mathbf{j}}. \tag{2.22d}$$

It is next convenient to rewrite (2.22a) – (2.22d) in terms of the electromagnetic field definitions (2.8) and (2.9). In the case of (2.22a), we recall that the background electric field $\mathbf{E}_0 = 0$ and realize that the specification of a charge neutral equilibrium plasma implies that $\hat{\rho}_0 = \sum_s q_s n_{0s} = 0$, where n_{0s} represents the equilibrium particle number density of a particular charged species s, with n_s itself defined in (1.11). We also simplify our analysis from hence forth by invoking our model case of a rudimentary two-species ion-electron plasma where $q_i = -q_e = e$, which means that we can take $n_{0e} = n_{0i} = n_0$. Hence, we can simplify (2.22a) as follows, where the $O(\epsilon)$ fluctuating charge density can be written as $\sum_s q_s \delta n_s$ in terms of the particle number density fluctuations δn_s,

$$\nabla \cdot \mathbf{E} = \nabla \cdot (\mathbf{E}_0 + \delta\mathbf{E}) = 4\pi \left(\sum_s q_s n_{0s} + \sum_s q_s \delta n_s \right) = 4\pi\hat{\rho},$$

$$\nabla \cdot \delta\mathbf{E} = 4\pi \sum_s q_s \delta n_s = 4\pi\delta\hat{\rho},$$
$$\nabla^2\Phi = -4\pi(\delta\hat{\rho}_e + \delta\hat{\rho}_i), \tag{2.23}$$

where we have used $\mathbf{E}_0 = 0$ and realized that the second term in (2.9) vanishes in (2.23) due to the Coulomb gauge. We now invoke our adiabatic electron assumption from Section 1.4 such that n_e follows the Boltzmann distribution $n_e = n_0 e^{-q_e\Phi/k_B T_e}$, which yields,

$$-4\pi\delta\hat{\rho}_e = -4\pi q_e n_0 \left(e^{-q_e\Phi/k_B T_e} - 1\right) \approx \frac{4\pi n_0 e^2}{k_B T_e}\Phi \approx \frac{1}{\lambda_{De}^2}\Phi. \tag{2.24}$$

Now, using the gyrokinetic ordering of (2.17), the assumption of (2.18), and the fact that $\nabla^2\Phi \sim (k_\perp^2 + k_\parallel^2)\Phi$, we can write the ratio of terms on either side of (2.23) as (Howes et al., 2006),

$$\frac{\nabla^2\Phi}{-4\pi\hat{\rho}_e} \sim \frac{k_\perp^2\lambda_{De}^2(1+\epsilon^2)\Phi}{\Phi} = k_\perp^2\lambda_{De}^2(1+\epsilon^2) \sim k_\perp^2\lambda_{De}^2 \ll 1. \tag{2.25}$$

Analyzing (2.25) further in terms of the ion plasma frequency $\omega_{pi} = \sqrt{4\pi n_i q_i^2/m_i} \approx \sqrt{4\pi n_0 e^2/m_i}$, where $\omega_{pi}/\Omega_i \sim 1/\epsilon$ in real tokamaks, gives (Wesson, 1997),

$$\frac{\nabla^2\Phi}{-4\pi\delta\hat{\rho}_e} \sim k_\perp^2\lambda_{De}^2 \sim \frac{1}{\rho_i^2}\frac{k_B T_e}{4\pi n_0 e^2} \approx \frac{1}{\rho_i^2}\frac{k_B T_i}{4\pi n_0 e^2} = \frac{\Omega_i^2}{v_{th_i}^2}\frac{m_i v_{th_i}^2/2}{4\pi n_0 e^2} \sim \frac{\Omega_i^2}{\omega_{pi}^2} \sim \epsilon^2, \tag{2.26}$$

where we have used (2.1) and the instructive simplification $T_i \approx T_e$. The result (2.26) implies that the $\nabla^2\Phi$ term on the left hand side of (2.23) is $O(\epsilon^2)$ compared with the $-4\pi\delta\hat{\rho}_e$ term on the right hand side. The two terms $-4\pi\delta\hat{\rho}_e$ and $-4\pi\delta\hat{\rho}_i$ must then cancel to the first two orders in ϵ, giving the quasineutrality condition,

$$\hat{\rho} = \hat{\rho}_0 + \delta\hat{\rho} = 0, \tag{2.27}$$

that approximates Poisson's law in gyrokinetic plasmas. In addition to the quasineutrality condition, the definition of the electric and magnetic fields in terms of the vector potential $\mathbf{A}$ and scalar electric potential Φ in (2.8) and (2.9) automatically satisfies (2.22b) and (2.22c). We can then define a simplified gyrokinetic formulation of Maxwell's electromagnetic field equations for the variables $\mathbf{A}, \Phi, \delta\mathbf{B}$, and $\delta\mathbf{E}$,

$$\hat{\rho} = \delta\hat{\rho} = 0, \tag{2.28a}$$
$$\delta\mathbf{B} = \nabla \times \mathbf{A}, \tag{2.28b}$$
$$\delta\mathbf{E} = -\nabla\Phi - \frac{1}{c}\frac{\partial\mathbf{A}}{\partial t}, \tag{2.28c}$$
$$\nabla \times \delta\mathbf{B} = \frac{4\pi}{c}\delta\hat{\mathbf{j}}. \tag{2.28d}$$

We will soon simplify this model further by considering the electrostatic limit where $\beta \to 0$ and neglect behavior dependent on $\mathbf{A}$ and $\delta\mathbf{B}$.

2.3 Guiding Center Coordinates & Gyroaveraging

It is at this point helpful to define a new set of coordinates that allows us to easily perform a gyroaverage in terms of the position $\mathbf{R}$ of the guiding center about which a given particle gyrates and the absolute position $\mathbf{r}$ of the particle itself. These two positions are related by (Littlejohn, 1983; Howes et al., 2006),

$$\mathbf{r} = \mathbf{R} - \frac{\mathbf{v} \times \hat{\mathbf{z}}}{\Omega_s}. \tag{2.29}$$

The absolute position is simply the gyration position of the particle with respect to the guiding center added to the absolute position of that guiding center. We express the particle velocity $\mathbf{v}$ in terms of a velocity $v_\parallel$ parallel to that of the guiding center, a velocity $v_\perp$ perpendicular to that of the guiding center, and a gyrophase angle θ,

$$\mathbf{v} = v_\parallel \hat{\mathbf{z}} + v_\perp(\cos\theta\hat{\mathbf{x}} + \sin\theta\hat{\mathbf{y}}), \tag{2.30}$$

where $\hat{\mathbf{x}}$ and $\hat{\mathbf{y}}$ represent the two Cartesian directions perpendicular to the magnetic field (Howes et al., 2006). We define the two ring averages of a function $a(\mathbf{r}, \mathbf{v}, t)$ as,

$$\langle a(\mathbf{r}, \mathbf{v}, t)\rangle_{\mathbf{R}} = \frac{1}{2\pi}\int a\left(\mathbf{R} - \frac{\mathbf{v} \times \hat{\mathbf{z}}}{\Omega_s}, \mathbf{v}, t\right) \mathrm{d}\theta, \tag{2.31}$$

$$\langle a(\mathbf{R}, \mathbf{v}, t)\rangle_{\mathbf{r}} = \frac{1}{2\pi}\int a\left(\mathbf{r} + \frac{\mathbf{v} \times \hat{\mathbf{z}}}{\Omega_s}, \mathbf{v}, t\right) \mathrm{d}\theta. \tag{2.32}$$

In (2.31) we keep $\mathbf{R}$, $v_\parallel$, and $v_\perp$ constant, while in (2.32) we keep $\mathbf{r}$, $v_\parallel$, and $v_\perp$ constant. Figure 2.1, reproduced from Howes et al. (2006), nicely presents this framework visually under the assumption that the particle drifts at a speed $u_\perp$, that the parallel length scale is $l_\parallel$, and that the difference between the position of $\mathbf{B}_0$ and $\mathbf{B}$ is $l_\perp$.

2.4 The Quasineutral Gyrokinetic Equations

We now summarize the results of substituting our expansions of f_s, $\mathbf{E}$, and $\mathbf{B}$ from (2.7) – (2.9) into the VFP equation (1.6) and arrive at the gyrokinetic modeling equations for a particular charged species s. A more detailed derivation of these results can be found in Appendix C. In gyrokinetic coordinates, where $\mathbf{v}$ is defined by the coordinates $(v_\parallel, v_\perp, \theta)$ with $|\mathbf{v}| \equiv \sqrt{v_\perp^2 + v_\parallel^2}$, we can write the VFP terms of zeroth order in ϵ with respect to the leading order quantity $\Omega_s F_0$ as (Howes et al., 2006),

$$\frac{\partial F_0}{\partial \theta} = 0. \tag{2.33}$$

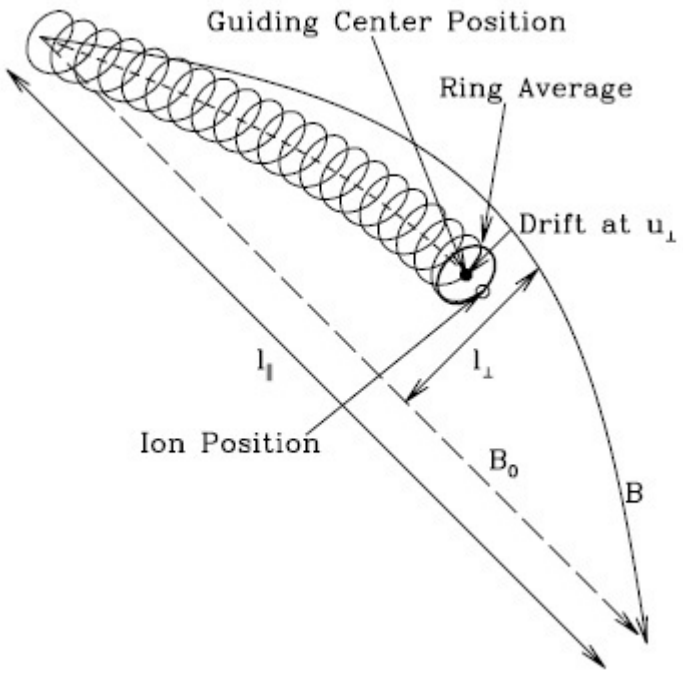

Figure 2.1: Ring-centered coordinates and the gyroaverage (Howes et al., 2006).

Physically, (2.33) implies that the background equilibrium distribution function F_0 is independent of the gyrophase angle θ. Considering first order terms in ϵ both constrains F_0 to be Maxwellian and allows us to write (Howes et al., 2006),

$$\mathbf{v}_\perp \cdot \nabla \delta f_{1s} - \Omega_s \frac{\partial \delta f_{1s}}{\partial \theta} = -\mathbf{v} \cdot \nabla \left(\frac{q_s \Phi}{k_B T_s} \right) F_0. \tag{2.34}$$

Howes et al. (2006) show that the particular solution to this problem is $\delta f_{ps} = -\left(q_s \Phi / k_B T_s\right) F_0 + O(\epsilon^2 F_0)$, meaning that $\delta f_{1s} = -(q_s \Phi / k_B T_s) F_0 + h_s$, where h_s represents the solution to the homogeneous problem,

$$\mathbf{v}_\perp \cdot \nabla h_s - \Omega_s \left(\frac{\partial h_s}{\partial \theta} \right)_{\mathbf{r}} = -\Omega_s \left(\frac{\partial h_s}{\partial \theta} \right)_{\mathbf{R}} = 0. \tag{2.35}$$

We can thus write f_s as,

$$f_s = F_0(|\mathbf{v}|, \epsilon^2 t) e^{-q_s \Phi(\mathbf{r},t)/k_B T_s} + h_s(\mathbf{R}, |\mathbf{v}|, v_\perp, t) + \delta f_{2s} ... \, , \tag{2.36}$$

under the realization that $1 - q_s \Phi / k_B T_s = \exp\left(-q_s \Phi / k_B T_s\right) + O(\epsilon^2)$ and that terms of $O(\epsilon^2)$ can be incorporated into δf_{2s}. Finally, at $O(\epsilon^2)$ we obtain an evolution equation for the modified distribution function perturbation $h_s = \delta f_{1s} + (q_s \Phi / k_B T_s) F_0$ in terms of the gyroaverage $\langle \chi \rangle_{\mathbf{R}}$ of the gyrokinetic potential $\chi = \Phi - \mathbf{v} \cdot \mathbf{A}/c$,

$$\frac{\partial h_s}{\partial t} + v_\parallel \hat{\mathbf{z}} \cdot \frac{\partial h_s}{\partial \mathbf{R}} + \frac{c}{B_0} \left\{ \langle \chi \rangle_{\mathbf{R}}, h_s \right\} - \left(\frac{\partial h_s}{\partial t} \right)_{coll} = \frac{q_s}{k_B T_s} \frac{\partial \langle \chi \rangle_{\mathbf{R}}}{\partial t} F_0, \tag{2.37}$$

in which $(\partial h_s/\partial t)_{coll}$ represents the effects of collisions and nonlinear effects arise through the Poisson bracket (Howes et al., 2006),

$$\{\langle\chi\rangle_{\mathbf{R}}, h_s\} = \hat{\mathbf{z}} \cdot \left(\frac{\partial \langle\chi\rangle_{\mathbf{R}}}{\partial \mathbf{R}} \times \frac{\partial h_s}{\partial \mathbf{R}} \right). \tag{2.38}$$

Importantly, h_s evolves on a much faster timescale than the background distribution F_0, which changes only on the slow overall heating timescale. Solving (2.37) for each charged species s gives a reasonable description of how a multidimensional plasma evolves in time.

At this point, we still need to close the model by relating χ to Maxwell's equations. We can accomplish this in the electrostatic regime relevant for low β plasmas by simply coupling (2.37) to the quasineutrality assumption (2.28a). To state the quasineutrality condition (2.28a) in terms of gyrokinetic variables, we multiply the distribution function (2.36) for each species by the charge q_s, integrate over all velocity space, and sum over all charged species s. Expanding the exponential term in (2.36) and dropping terms of $O(\epsilon^2)$ or greater yields,

$$\hat{\rho} = \sum_s q_s \int f_s \mathrm{d}^3\mathbf{v} = \sum_s \left[-\frac{q_s^2 n_0}{k_B T_s} \Phi + q_s \int h_s \left(\mathbf{r} + \frac{\mathbf{v} \times \hat{\mathbf{z}}}{\Omega_s}, \mathbf{v}, t \right) \mathrm{d}^3\mathbf{v} \right] = 0, \tag{2.39}$$

where the background terms have, as expected, canceled due to overall charge neutrality. Taking the gyroaverage of (2.39) then gives the appropriate equation with which to couple the gyrokinetic equation itself. Hence, we can state the Gyrokinetic-Quasineutral (GK-Q) system as,

$$\frac{\partial h_s}{\partial t} + v_\parallel \hat{\mathbf{z}} \cdot \frac{\partial h_s}{\partial \mathbf{R}} + \frac{c}{B_0} \{\langle\chi\rangle_{\mathbf{R}}, h_s\} - \left(\frac{\partial h_s}{\partial t} \right)_{coll} = \frac{q_s}{k_B T_s} \frac{\partial \langle\chi\rangle_{\mathbf{R}}}{\partial t} F_0, \tag{2.40}$$

$$\sum_s \left[-\frac{q_s^2 n_0}{k_B T_s} \Phi + q_s \int \langle h_s \rangle_{\mathbf{r}} \mathrm{d}^3\mathbf{v} \right] = 0. \tag{2.41}$$

2.5 1+1-D Version of the GK-Q System

We now propose a simplified GK-Q system with only parallel dimensions. We consider the electrostatic limit of our simple two-species plasma consisting of electrons and a single ion species with one parallel dimension in both position and velocity space. We may thus drop the $\parallel$ subscripts from (2.40) and (2.41). In a single dimension, the "gyroaverage" of a quantity becomes the quantity itself, so the angle brackets may be removed from the GK-Q system. For low β, we can neglect $\partial \mathbf{A}/\partial t$ in the perturbed

electric field because the magnetic field will be strong enough to resist distortion by the plasma. Moreover, the Poisson bracket of (2.38) contains a cross product that evaluates to zero in one dimension. We may thus rewrite the GK-Q system for the single ion species under these assumptions as,

$$\frac{\partial h_i}{\partial t} + v\frac{\partial h_i}{\partial z} - \frac{q_i}{k_B T_i}\frac{\partial \Phi}{\partial t}F_0 = \left(\frac{\partial h_i}{\partial t}\right)_{coll}, \tag{2.42}$$

$$\sum_s \left[-\frac{q_s^2 n_0}{k_B T_s}\Phi + q_s \int_{-\infty}^{\infty} h_s \mathrm{d}v\right] = 0. \tag{2.43}$$

Substituting $h_i = \delta f_{1i} + (q_i\Phi/k_B T_i)F_0$ into (2.42), recalling that collisions do not affect the equilibrium distribution function, and invoking $E = -\nabla\Phi$ yields,

$$\begin{aligned}
\frac{\partial \delta f_{1i}}{\partial t} + \frac{q_i}{k_B T_i}\frac{\partial \Phi}{\partial t}F_0 + v\frac{\partial}{\partial z}\left(\delta f_{1i} + \frac{q_i\Phi}{k_B T_i}F_0\right) - \frac{q_i}{k_B T_i}\frac{\partial \Phi}{\partial t}F_0 &= \left(\frac{\partial \delta f_{1i}}{\partial t}\right)_{coll}, \\
\frac{\partial \delta f_{1i}}{\partial t} + v\frac{\partial \delta f_{1i}}{\partial z} - v\frac{q_i E}{k_B T_i}F_0 &= \left(\frac{\partial \delta f_{1i}}{\partial t}\right)_{coll}, \\
\frac{\partial \delta f_{1i}}{\partial t} + v\frac{\partial \delta f_{1i}}{\partial z} + \frac{q_i E}{m_i}\frac{\partial F_0}{\partial v} &= \left(\frac{\partial \delta f_{1i}}{\partial t}\right)_{coll},
\end{aligned} \tag{2.44}$$

where we have used $\partial F_0/\partial v = -(m_i v/k_B T_i)F_0$ for Maxwellian F_0. We next explicitly invoke the adiabatic electron assumption from Section 1.4 such that the electrons follow a Boltzmann distribution,

$$f_e = F_0 + \delta f_{1e} + O(\epsilon^2) = F_0 e^{-q_e\Phi/k_B T_e} = F_0 - \frac{q_e\Phi}{k_B T_e}F_0 + O(\epsilon^2), \tag{2.45}$$

which implies that $\delta f_{1e} = -(q_e\Phi/k_B T_e)F_0$ and therefore that $h_e = 0$. We may thus simplify (2.43) using this result along with the previous assumptions that $q_i = -q_e$ and $n_0 = \int_{-\infty}^{\infty} F_0 \mathrm{d}v = 1$,

$$\begin{aligned}
\frac{q_e^2}{k_B T_e} &= q_i \int_{-\infty}^{\infty}\left(h_i - \frac{q_i\Phi}{k_B T_i}F_0\right)\mathrm{d}v = q_i\int_{-\infty}^{\infty}\delta f_{1i}\mathrm{d}v, \\
\frac{q_i}{k_B T_i} &= \eta\int_{-\infty}^{\infty}\delta f_{1i}\mathrm{d}v,
\end{aligned} \tag{2.46}$$

in terms of the temperature ratio $\eta \equiv T_e/T_i$. Thus, we can rewrite the 1+1-D GK-Q system as,

$$\frac{\partial \delta f_{1i}}{\partial t} + v\frac{\partial \delta f_{1i}}{\partial z} + \frac{q_i E}{m_i}\frac{\partial F_0}{\partial v} = \left(\frac{\partial \delta f_{1i}}{\partial t}\right)_{coll}, \tag{2.47}$$

$$E = -\frac{\partial \Phi}{\partial z}, \quad \frac{q_i}{k_B T_i}\Phi = \eta\int_{-\infty}^{\infty}\delta f_{1i}\mathrm{d}v. \tag{2.48}$$

The electrostatic GK-Q model in a single parallel dimension therefore reduces to a collisional Vlasov-Quasineutral (V-Q) system consisting of a linearized collisional Vlasov equation coupled to the quasineutrality condition.

Chapter 3

A 1+1-D Fourier-Hermite Model of a Quasineutral Plasma

In this section, we develop a numerical model of a collisional, unforced 1+1-D V-Q system using a Fourier-Hermite expansion of the perturbed distribution function.

3.1 Construction of a Collisionless Numerical Model

To begin, we recall the collisionless Vlasov equation for a single species s,

$$\frac{\partial f_s}{\partial t} + \mathbf{v} \cdot \nabla f_s + \frac{q_s}{m_s}\left(\mathbf{E} + \frac{\mathbf{v} \times \mathbf{B}}{c}\right) \cdot \nabla_{\mathbf{v}} f_s = 0. \tag{3.1}$$

We now write the distribution function as $f_s = F_0 + \delta f_{1s}$ for a perturbation δf_{1s}. Since $\mathbf{v} \parallel \mathbf{B}$, the one dimensional version of (3.1) is,

$$\frac{\partial \delta f_{1s}}{\partial t} + v\frac{\partial \delta f_{1s}}{\partial z} + \frac{q_s E}{m_s}\frac{\partial \delta f_{1s}}{\partial v} = -\frac{q_s E}{m_s}\frac{\partial F_0}{\partial v}, \tag{3.2}$$

where z is the parallel spatial coordinate, v is the parallel velocity coordinate, and t is time. We now normalize (3.2) using gyrokinetic variables and consider the ion behavior within our two-species ion-electron plasma with background Maxwellian distributions for both species,

$$t' = \omega t; \quad v' = v/v_{th_i}; \quad z' = z/l_0; \quad E' = (q_i l_0/k_B T_i)E. \tag{3.3}$$

The appropriate gyrokinetic normalization of E is implied by that of the electric potential, which naturally scales as $\Phi \to (q_i/k_B T_i)\Phi$ from (2.48) (Ganesh et al., 2010). Because $E = -\partial\Phi/\partial z$ and z is normalized by l_0, the natural scaling for the electric field becomes $E \to (q_i l_0/k_B T_i)E$. The dimensionless form of (3.2) is thus,

$$\frac{\partial \delta f_{1i}}{\partial t'} + \frac{v_{th_i}}{l_0\omega}v'\frac{\partial \delta f_{1i}}{\partial z'} + \frac{k_B T_i}{m_i v_{th_i} l_0 \omega}E'\frac{\partial \delta f_{1i}}{\partial v'} = -\frac{k_B T_i}{m_i v_{th_i} l_0 \omega}E'\frac{\partial F_0}{\partial v'}. \tag{3.4}$$

We now enforce several important conditions on the multiplicative constants in (3.4). We choose the frequency scale such that $\omega = v_{th_i}/l_0$. Thus, taking $q_i = -q_e = e$ in our simple plasma as in Section 2.5 gives,

$$\frac{k_B T_i}{m_i v_{th_i} l_0 \omega} = \frac{m_i v_{th_i}^2/2}{m_i v_{th_i}^2} = \frac{1}{2}. \tag{3.5}$$

Using these scalings and dropping the primes from our normalized variables, we recover a normalized Vlasov equation for a quasineutral fusion plasma,

$$\frac{\partial \delta f_{1i}}{\partial t} + v\frac{\partial \delta f_{1i}}{\partial z} + \frac{1}{2}E\frac{\partial \delta f_{1i}}{\partial v} = -\frac{1}{2}E\frac{\partial F_0}{\partial v}. \tag{3.6}$$

In the full gyrokinetic framework, we replaced Poisson's law (2.22a) with the quasineutrality assumption of (2.28a). We must now appropriately express this condition in a single dimension. Equation (2.28a) implies that summing over all charged species s gives,

$$\delta\hat{\rho} = \sum_s q_s \int_{-\infty}^{\infty} \delta f_{1s} \mathrm{d}v = e\int_{-\infty}^{\infty} \delta f_{1i}\mathrm{d}v - e\int_{-\infty}^{\infty} \delta f_{1e}\mathrm{d}v = e\left(\delta n_i - \delta n_e\right) = 0. \tag{3.7}$$

We may therefore explicitly take $\delta n_i = \delta n_e$ from (3.7). At this point, we again invoke the adiabatic electron assumption of (2.45) to write,

$$\frac{\delta f_{1e}}{F_0} = \frac{e\Phi}{k_B T_e}, \tag{3.8}$$

which becomes the following in terms of $\eta = T_e/T_i$ under our normalization of Φ,

$$\eta \delta f_{1e} = \Phi F_0. \tag{3.9}$$

Integrating (3.9) over v therefore gives,

$$\eta \delta n_e = \Phi, \tag{3.10}$$

since F_0 integrates to unity in velocity space. Combining (3.7) and (3.10) gives,

$$\Phi = \eta\delta n_e = \eta\delta n_i = \eta\int_{-\infty}^{\infty} \delta f_{1i}\mathrm{d}v. \tag{3.11}$$

The left hand side of (3.11) has no Laplacian, as Poisson's law normally does, as a result of quasineutrality and the fact that the parallel wavelengths are very long compared to λ_{De} (Belli and Hammett, 2005; Pueschel et al., 2010). We take $\eta = 1$ in the following numerical work to simplify comparisons amongst different sets of results,

but we retain it generally in theoretical work for completeness.[1] Equations (3.6) and (3.11) give the dimensionless 1+1-D V-Q description of a fusion plasma that will be the subject of our following analysis. Encouragingly, these expressions, summarized below in (3.12) – (3.13), resemble the undriven model of Pueschel et al. (2010) and the electrostatic limit of the model in Belli and Hammett (2005),

$$\frac{\partial \delta f_{1i}}{\partial t} + v\frac{\partial \delta f_{1i}}{\partial z} + \frac{1}{2}E\frac{\partial \delta f_{1i}}{\partial v} = -\frac{1}{2}E\frac{\partial F_0}{\partial v}, \tag{3.12}$$

$$E = -\frac{\partial \Phi}{\partial z}, \quad \Phi = \eta \int_{-\infty}^{\infty} \delta f_{1i} \mathrm{d}v. \tag{3.13}$$

It is at this point important to realize that in many situations, the normalized electric field is assumed to be small such that $|E(\partial \delta f_{1i}/\partial v)| \ll 1$, meaning that the last term on the left hand side of (3.12) could reasonably be neglected. More formally, our gyrokinetic ordering indicates that the linear terms in (3.12) are all $O(\epsilon)$. The nonlinear term $E(\partial \delta f_{1i}/\partial v)$ is a bit more complex in that it is $O(\epsilon^2)$ provided that $\partial \delta f_{1i}/\partial v$ varies smoothly in v on $O(1)$ scales, but can become much larger depending on the level of collisionality in the system. In the present collisionless case, for instance, δf_{1i} can develop arbitrarily fine scale structure in v, meaning that $\partial \delta f_{1i}/\partial v$ can become arbitrarily large. We will later implement collisionality to mitigate this issue by smoothing fine scales in v, but this analysis motivates us to retain the electrostatic nonlinearity given that it can become quite large indeed. We therefore carry each of these terms forward in our analysis for completeness, but may find it useful to occasionally drop the nonlinearity to examine the behavior of the linear system.

Encouragingly, the collisionless V-Q system in (3.12) – (3.13) is exactly the normalized collisionless version of the simplified 1+1-D GK-Q system of (2.47) – (2.48) with the addition of the nonlinear term proportional to $E(\partial \delta f_{1i}/\partial v)$. This term does not appear in our second order gyrokinetics because the higher-dimensional electrostatic nonlinearities that appear in full-dimensional gyrokinetics are formally $O(\epsilon^3)$, but this phenomenon certainly does influence higher order gyrokinetics and is thus quite relevant. The dominant nonlinearity in the second order gyrokinetics presented here in (2.38) disappears in a single dimension because it is dependent on a cross product. We have thus shown that deriving the collisionless portion of a 1+1-D model of a quasineutral plasma from first principles agrees well with our reduction of the gyrokinetic model. The linear parts of the collisionless 1+1-D GK-Q and V-Q systems are the same, but we retain the electrostatic nonlinearity in the 1+1-D V-Q system

[1] This term is often omitted from less general single-species analyses.

defined above. We will later add collisionality to our 1+1-D V-Q system to approximate the $(\partial \delta f_{1i}/\partial t)_{coll}$ term in (2.48) that describes the effect of weak collisions in gyrokinetic plasmas.

At this point, we would like to transform (3.12) so that we can easily assess how fine scales develop in both position and velocity space over time. While a Fourier expansion of the distribution function in position space appears logical under our assumption of periodic boundary conditions, the appropriate transformation to apply in velocity space is less clear. Fortunately, following the work of Grad (1949), Armstrong (1967), Siminos et al. (2011), and others, it becomes apparent that a Hermite expansion in velocity space will yield particularly useful results. We utilize the Hermite functions $\phi^n(v)$ defined in terms of the Hermite polynomials $H_n(v)$ by,

$$\phi^n(v) \equiv \frac{H_n(v)}{\sqrt{2^n n!}}, \qquad H_n(v) \equiv (-1)^n e^{(v^2)} \frac{\mathrm{d}^n}{\mathrm{d}v^n}\left(e^{-v^2}\right). \tag{3.14}$$

We can take further advantage of the background distribution function being the normalized Maxwellian $F_0 = \pi^{-1/2} e^{-v^2}$ by defining the dual Hermite functions ϕ_n,

$$\phi_n(v) \equiv F_0 \phi^n(v). \tag{3.15}$$

The integral inner product of ϕ_n and ϕ^m satisfies the orthogonality relation,

$$\int_{-\infty}^{\infty} \phi_n \phi^m \mathrm{d}v = \int_{-\infty}^{\infty} \phi^n(v) \phi^m(v) F_0(v) \mathrm{d}v = \delta_{n,m} \ \forall \ n, m, \tag{3.16}$$

where the Hermite functions for $n \geq 0$ form a complete set.[2] Using these definitions, then, we accomplish our desired expansion of δf_{1i} in Fourier-Hermite space as,

$$\delta f_{1i}(z, v, t) = \sum_{\substack{n=0, \\ j=-\infty}}^{\infty} a_{n,j}(t) \phi_n(v) e^{i k_j z}, \tag{3.17}$$

where the $a_{n,j}$ are time dependent scalar coefficients and k_j is the wavenumber of the j^{th} spatial Fourier mode. We utilize a uniform Fourier grid such that $k_j = j\Delta k$ with $\Delta k = 2\pi/L_N$, where L_N is the length of the periodic box defined in units of l_0.

Before proceeding to advancing the $a_{n,j}$ in time, it is important to investigate the effect of our ansatz for δf_{1i} on the rest of the system. Combining (3.13) and (3.17) with $\eta = 1$ and using the fact that $\phi^0(v) = H_0(v)/\sqrt{2^0 0!} = 1$ gives a convenient expression for Φ in terms of the zeroth degree Hermite coefficients,[3]

$$\Phi = \int_{-\infty}^{\infty} \delta f_{1i} \mathrm{d}v = \sum_{\substack{n=0, \\ j=-\infty}}^{\infty} a_{n,j}(t) e^{i k_j z} \int_{-\infty}^{\infty} \phi_n(v) \, (1) \, \mathrm{d}v = \sum_{j=-\infty}^{\infty} a_{0,j}(t) e^{i k_j z}. \tag{3.18}$$

[2] We will often use this Kronecker delta notation where $\delta_{n,m} = 1$ for $n = m$ and $\delta_{n,m} = 0$ otherwise.
[3] A more detailed derivation of (3.18) may be found in Appendix D.1.

Using (3.18) to calculate the electric field from (3.13) gives an explicit expression,[4]

$$E = -\frac{\partial \Phi}{\partial z} = -i \sum_{j \neq 0} a_{0,j}(t) k_j e^{i k_j z}. \tag{3.19}$$

As in Armstrong (1967), we do not include the $j = 0$ term in the electric field summation because this term has wavenumber zero and thus does not contribute to $E = -\partial\Phi/\partial z$ because it is constant in z. We now substitute the expansion (3.17) into (3.12) to evolve the $a_{n,j}$ in time. In this substitution we have used a dot $\dot{}$ for the time derivative, indicated the velocity derivative with a prime $'$, and dropped explicit dependence on independent variables for convenience,

$$\sum_{\substack{n=0 \\ j=-\infty \\ h\neq 0}}^{\infty} \left(\dot{a}_{n,j} \phi_n e^{i k_j z} + i k_j a_{n,j} v \phi_n e^{i k_j z} - \frac{1}{2} i k_h a_{n,j} a_{0,h} \phi_n' e^{i(k_j + k_h) z} \right) = -\frac{1}{2} E F_0' \ . \tag{3.20}$$

We use h to index the electric field expression to distinguish this Fourier expansion from that used for δf_{1i}. We do not yet substitute (3.19) for the E term on the right hand side of (3.20) for compactness. We now use the two Hermite function recurrence relations (Abramowitz and Stegun, 1972; Parker and Dellar, 2012; Weisstein, 2012),

$$v\phi_n(v) = \sqrt{\frac{n+1}{2}} \phi_{n+1}(v) + \sqrt{\frac{n}{2}} \phi_{n-1}(v), \tag{3.21}$$

$$\phi^{n\prime}(v) = \sqrt{2n} \phi^{n-1}(v).^5 \tag{3.22}$$

We apply these relations to evaluate ϕ_n' using our previous expression $F_0 = \pi^{-1/2} e^{-v^2}$,

$$\begin{aligned} \phi_n' &= (F_0 \phi^n)' = F_0' \phi^n + F_0 \phi^{n\prime} = -2v F_0 \phi^n + \sqrt{2n} F_0 \phi^{n-1} = -2v\phi_n + \sqrt{2n}\phi_{n-1}, \\ &= -2 \left(\sqrt{\frac{n+1}{2}} \phi_{n+1} + \sqrt{\frac{n}{2}} \phi_{n-1} \right) + \sqrt{2n} \phi_{n-1}, \\ &= -\sqrt{2n+2} \phi_{n+1}. \end{aligned} \tag{3.23}$$

Substituting (3.21) and (3.23) into (3.20) and evaluating $F_0' = -2vF_0$ gives,

$$\sum_{\substack{n=0 \\ j=-\infty \\ h\neq 0}}^{\infty} \left\{ \dot{a}_{n,j} \phi_n e^{i k_j z} + i k_j a_{n,j} \left(\sqrt{\frac{n+1}{2}} \phi_{n+1} + \sqrt{\frac{n}{2}} \phi_{n-1} \right) e^{i k_j z} - \right.$$
$$\left. \frac{1}{2} i k_h a_{n,j} a_{0,h} \left[-\sqrt{2n+2} \phi_{n+1} \right] e^{i(k_j + k_h) z} \right\} = v E F_0. \tag{3.24}$$

[4]Our convention is that $\sum_{n=a}^{b}$ is an explicit sum from $n = a$ to $n = b$ while $\sum_{n \neq c} = \sum_{n=-\infty}^{n=\infty}$, $n \neq c$.
[5]This follows from the fact that $H_n'(v) = 2nH_{n-1}(v)$

We now project (3.24) onto both the g^{th} Fourier mode and the p^{th} Hermite mode by multiplying through by $\phi^p e^{-ik_g z}$ and integrating with respect to both z and v,[6]

$$\begin{aligned} \dot{a}_{p,g} + ik_g \left(a_{p-1,g}\sqrt{\frac{p}{2}} \quad + \quad a_{p+1,g}\sqrt{\frac{p+1}{2}} \right) + \\ \frac{1}{2} i \sqrt{2p} \sum_{j \neq g} a_{p-1,j} a_{0,g-j} k_{g-j} \quad = \quad \frac{1}{2L_g} \int_{-\infty}^{\infty} \int_{-L_g}^{L_g} v E F_0 e^{-ik_g z} \phi^p \mathrm{d}z \mathrm{d}v, \end{aligned} \tag{3.25}$$

where $L_g \equiv L_N/2$ represents the half length of the periodic box on which each g^{th} Fourier mode is defined. Note that (3.25) will hold true as long as the grid of Fourier wavenumbers is evenly spaced because $j + h = g$ then implies that $k_j + k_h = k_g$. As we will be using a uniform Fourier grid in this study, we can write $k_j = j\Delta k$ from hence forth.

Equation (3.25) holds for all possible values of p and g, leading to an infinite nonlinear system. For numerical applications, however, we must truncate both the Fourier and Hermite series representations. Thus, in reality, $p = 0...N$, with $N + 1$ the number of Hermite modes in a truncated Hermite series, and $g = 0...K$, with $K+1$ the number of modes in a truncated Fourier series. We now begin to format our expressions for numerical computation by writing the truncated version of the infinite linear system of (3.25) in matrix form. We write the Fourier-Hermite coefficients as an $(N + 1) \times (K + 1)$ vector,

$$\mathbf{a} = \{a_{0,0},\ a_{0,1}, ...\ a_{0,K},\ a_{1,0},\ a_{1,1}, ...\ a_{1,K},\ ...a_{N,0},\ ...\ a_{N,K}\}^T. \tag{3.26}$$

Defining an expression $y_{p,g}$ for the negated magnitude of the nonlinear term in (3.25) with $k_g = g\Delta k$ and prescribing an analogous $(N + 1) \times (K + 1)$ vector $\mathbf{y}$ yields,

$$y_{p,g} = -\sqrt{\frac{p}{2}} \Delta k \sum_{j \neq g} (g - j) a_{0,g-j} a_{p-1,j}, \tag{3.27}$$

$$\mathbf{y} = \{0,\ 0, ...\ 0,\ y_{1,0},\ y_{1,1}, ...\ y_{1,K},\ ...y_{N,0},\ ...\ y_{N,K}\}^T, \tag{3.28}$$

where we retain the $j \neq g$ notation to indicate that as many modal interactions as possible should be included for each spatial wavenumber at a given resolution in Fourier space. This expression correctly gives $y_{p,g} = 0$ for $p = 0$ (Armstrong, 1967). Finally, simplifying the expression for the integral term in (3.25) multiplied by i^{-1} while using $k_j = j\Delta k$ and invoking the Hermite recurrence relation of (3.21) gives,[7]

$$L_{p,g} \quad = \quad \frac{1}{2iL_g} \int_{-\infty}^{\infty} \int_{-L_g}^{L_g} v E F_0 e^{-ik_g z} \phi^p \mathrm{d}z \mathrm{d}v = -\frac{1}{\sqrt{2}} g \Delta k a_{0,g} \delta_{p,1} \bar{\delta}_{g,0}, \tag{3.29}$$

[6] A detailed derivation of (3.25) by integration in z and v may be found in Appendix D.2.
[7] A detailed derivation of (3.29) may be found in Appendix D.3.

where $\bar{\delta}_{i,j} \equiv (1 - \delta_{i,j})$. Since, $L_{p,g} \neq 0$ only if $p = 1$ and $g \neq 0$, we obtain a rather simple vector,

$$\mathbf{L} = \{0,\ 0, ...0,\ L_{1,1}, ...\ L_{1,K},\ 0, ...\ 0\}^T. \tag{3.30}$$

Only elements $K + 3$ through $2K + 2$ of $\mathbf{L}$ are nonzero as a result of the $\bar{\delta}_{g,0}$ and $\delta_{p,1}$ terms. Moreover, we rewrite (3.25) in the more convenient form,

$$\dot{a}_{p,g} = -ig\Delta k \left(a_{p-1,g}\sqrt{\frac{p}{2}} + a_{p+1,g}\sqrt{\frac{p+1}{2}} \right) + iy_{p,g} + iL_{p,g}, \tag{3.31}$$

with $p = 0...N$ and $g = 0...K$. Equation (3.31) allows us to easily write a matrix-vector equation to advance the coefficients of the distribution function in time,

$$\dot{\mathbf{a}} = i(\mathbf{Ma} + \mathbf{y} + \mathbf{L}). \tag{3.32}$$

The square matrix $\mathbf{M}$ of size $(N + 1) \times (K + 1)$ operates on $\mathbf{a}$ to evaluate the linear first term on the right hand side of (3.31) and $\mathbf{y}$ and $\mathbf{L}$ are as defined above. The order in which coefficients are placed in the relevant vectors and matrices can be found from (3.26), (3.28), and (3.30), respectively. As implied by (3.32), each row of the sparse bidiagonal matrix $\mathbf{M}$ contains only two coefficients, so evaluating necessary matrix-vector products with $\mathbf{M}$ is inexpensive. The $\mathbf{L}$ vector will also be quite simple to evaluate computationally given its simple linear dependence on the K coefficients wherein $p = 1$ and $g \neq 0$. The nonlinear vector $\mathbf{y}$, however, will require a specialized evaluation procedure. Necessary series truncations in these expressions effectively act as boundary conditions wherein cascade to wavenumbers higher than N or K is prohibited, which is not particularly physical and thus will require additional consideration (Parker and Dellar, 2012).

3.2 Implementing Collisionality

To observe sensible behavior commensurate with weakly collisional plasmas, we insert a collisionality term into the transformed Vlasov equation of (3.32) to obtain an analogous VFP equation. It has been shown that the linearized Dougherty collision operator of (1.12) can be written in Hermite space as (e.g. Parker and Dellar, 2012),

$$C[\delta f_{1i}] = \sum_{\substack{n=0,\\ j=-\infty}}^{\infty} -\nu n a_{n,j}\phi_n e^{ik_j z} + \nu a_{1,j}\phi_1 e^{ik_j z} + 2\nu a_{2,j}\phi_2 e^{ik_j z}. \tag{3.33}$$

To combine this collisionality expression with our transformed model of the collisionless V-Q system from (3.31), we must project (3.33) onto a single Hermite mode p and

single Fourier mode g by taking the appropriate integral inner products with respect to ϕ^p and $e^{-ik_g z}$, respectively. Performing these operations leads to the following expression for $C_{p,g}$,[8]

$$C_{p,g} = \frac{1}{2L_g}\int_{-\infty}^{\infty}\int_{-L_g}^{L_g} C[\delta f_{1i}]e^{-ik_g z}\phi^p \mathrm{d}z\mathrm{d}v = \nu\left(a_{1,g}\delta_{p,1} + 2a_{2,g}\delta_{p,2} - pa_{p,g}\right). \quad (3.34)$$

Finally, we add the last expression of (3.34) to the right hand side of (3.31) to obtain a VFP equation in Fourier-Hermite space that conserves mass, momentum, and energy,

$$\dot{a}_{p,g} = -ig\Delta k\left(a_{p-1,g}\sqrt{\frac{p}{2}} + a_{p+1,g}\sqrt{\frac{p+1}{2}}\right) + iy_{p,g} + iL_{p,g} + C_{p,g}. \quad (3.35)$$

Finally, defining $\mathbf{C}$ as the vector below,

$$\mathbf{C} = \{C_{0,0},\ C_{0,1}, \ldots\ C_{0,K},\ C_{1,0},\ C_{1,1}, \ldots\ C_{1,K},\ \ldots C_{N,0},\ \ldots\ C_{N,K}\}^T, \quad (3.36)$$

allows us to write,

$$\dot{\mathbf{a}} = i(\mathbf{M}\mathbf{a} + \mathbf{y} + \mathbf{L}) + \mathbf{C}. \quad (3.37)$$

Equation (3.37) differs from (3.32) by a real collisionality $\mathbf{C}$ that creates damping.

3.3 Truncation and Hypercollisionality

While the collisionality will certainly make the results of this model more physical and prevent reflection of disturbances off of the highest Hermite mode, the Dougherty collision operator with sufficiently large ν can cause problems by damping out the lower Hermite modes that contribute to accurate solution of the collisional VFP system (Parker and Dellar, 2012). What one would hope for from a numerical standpoint, then, is a method by which one could use collisionality to damp the highest Hermite modes without destroying useful modes in the middle ranges, effectively truncating the Hermite series much earlier than necessary. This task can be accomplished by implementing a framework known as "hypercollisionality" inspired by such earlier work as Joyce et al. (1971), Knorr and Shoucri (1974), and Shoucri and Gagné (1971). Hypercollisionality is similar in principle to hyperviscosity methods commonly used in spectral discretizations of Navier-Stokes turbulence (e.g. Passot and Pouqet, 1988).

Utilizing hypercollisions replaces the coefficients in the linearized Dougherty collision operator with adjusted coefficients that apply more selective damping to the highest Hermite modes. If, for instance, we conceptualize the transformed linearized

[8] A detailed derivation of (3.34) may be found in Appendix D.4.

Dougherty operator of (3.34) in terms of a Hermite mode dependent function $x(p) = \nu p$, we can rewrite it in the following form,

$$C_{p,g} = x(1)a_{1,g}\delta_{p,1} + x(2)a_{2,g}\delta_{p,2} - x(p)a_{p,g}. \tag{3.38}$$

To implement hypercollisions, we define a new function $x^{hyp}(p)$ to replace $x(p)$,

$$x^{hyp}(p) = \nu \left(\frac{p}{N}\right)^n, \tag{3.39}$$

where N is the maximum Hermite wavenumber and n is an arbitrary power that controls the relative severity of the damping undergone by the lower Hermite modes. This function takes a maximum value of ν at $p = N$ and values near zero at lower modes, which results in $O(\nu)$ damping of the highest modes and very little damping of the lower modes (Parker and Dellar, 2012). Setting $n = 1$ such that $x^{hyp}(p) = x(p)$ reduces the hypercollisional operator to the Dougherty operator. Writing the hypercollisional version of (3.38) with $x^{hyp}(p)$ replacing $x(p)$ defines $C^{hyp}_{p,g}$ as below,

$$\begin{aligned} C^{hyp}_{p,g} &= x^{hyp}(1)a_{1,g}\delta_{p,1} + x^{hyp}(2)a_{2,g}\delta_{p,2} - x^{hyp}(p)a_{p,g}, \\ &= \nu\left[\left(\frac{1}{N}\right)^n a_{1,g}\delta_{p,1} + \left(\frac{2}{N}\right)^n a_{2,g}\delta_{p,2} - \left(\frac{p}{N}\right)^n a_{p,g}\right]. \end{aligned} \tag{3.40}$$

Hence, we can write the hypercollisional version of the 1+1-D model in (3.37) as,

$$\dot{\mathbf{a}} = i(\mathbf{M}\mathbf{a} + \mathbf{y} + \mathbf{L}) + \mathbf{C}^{\mathbf{hyp}}. \tag{3.41}$$

3.4 1+1-D Model Computational Implementation

At this point, we have developed a viable 1+1-D numerical model of a collisional electrostatic V-Q system that is well suited for computational implementation. We use a carefully constructed MATLAB code based on a classical fourth-order fixed-timestep explicit Runge-Kutta (RK4) routine to execute the model in a manner that allows for relatively easy analysis while maintaining feasible runtimes. Detailed descriptions of input parameters, spectral filters, temporal solution advancement, numerical stability criteria, output parameters, potential weaknesses, and possible improvements can be found in Appendix E. All code used for these simulations was constructed solely by the author excepting three subroutines based on code from the public domain archive MATLAB Central.[9] While the several thousand lines of MATLAB code constituting this model are not reproduced here for brevity, all code is available from the author on request.

[9]These subroutines, *peakdet.m*, *HermitePoly.m*, and *faddeeva.m*, find peaks in oscillatory signals, define matrices used to efficiently evaluate Hermite polynomials $H_n(v)$, and numerically approximate the plasma dispersion function $Z(\zeta)$, respectively.

Chapter 4

Classical Electrostatic Validation

Before applying our numerical model to quasineutral fusion plasmas, we validate it against a comprehensive set of benchmark results for the single-species V-P system by Heath et al. (2012) using a discontinuous Galerkin discretization in phase space.

4.1 Adjustments for Classical Electrostatics

The Vlasov-Poisson system describes a single-species electron plasma that operates on different characteristic scales from our quasineutral two-species fusion plasma. Appropriate normalizations to recover an expression similar to (3.6) are,

$$t' = \omega_p t; \quad v' = v/v_{th_e}; \quad z' = z/\lambda_{De}; \quad E' = (e\lambda_{De}/2k_B T_e)E, \tag{4.1}$$

where the plasma frequency $\omega_p \equiv v_{th_e}/\lambda_{De}$ (Huba, 2009). These scalings are chosen to exactly reproduce the nondimensional system modeled by Heath et al. (2012).[1] Substituting these definitions into the Vlasov equation with $q_e = -e$ gives,

$$\frac{\partial \delta f_{1e}}{\partial t'} + \frac{v_{th_e}}{\omega_p \lambda_{De}} v' \frac{\partial \delta f_{1e}}{\partial z'} - \frac{2k_B T_e}{m_e v_{th_e} \lambda_{De} \omega_p} E' \frac{\partial \delta f_{1e}}{\partial v'} = \frac{2k_B T_e}{m_e v_{th_e} \lambda_{De} \omega_p} E' \frac{\partial F_0}{\partial v'}. \tag{4.2}$$

The leading coefficients in (4.2) all go to unity under this normalization, giving,

$$\frac{\partial \delta f_{1e}}{\partial t} + v \frac{\partial \delta f_{1e}}{\partial z} - E \frac{\partial \delta f_{1e}}{\partial v} = E \frac{\partial F_0}{\partial v}. \tag{4.3}$$

The only difference between (4.3) and (3.6) is the lack of factors of 1/2 on the electrostatic terms. However, we now couple (4.3) to the one dimensional Poisson's law (4.4) of Heath et al. (2012) instead of to the earlier quasineutrality condition (3.13),

$$\frac{\partial^2 \Phi}{\partial z^2} = \int_{-\infty}^{\infty} \delta f_{1e} \mathrm{d}v. \tag{4.4}$$

[1] These normalizations are in fact exactly the same as those in Section 3.1 other than the substitution of λ_{De} for l_0 as the characteristic length scale and the factor of two in the normalization of E, which results from the fact that we define $k_B T_e = m v_{th_e}^2/2$ whereas Heath et al. (2012) use $k_B T_e = m_e v_{th_e}^2$.

The only differences between (4.4) and (3.13) are the Laplacian on the left hand side and the implicit assumption that $\eta = 1$, which we maintain for simplicity in all of our V-P and V-Q numerical simulations. These changes ultimately result in a simple adjustment to terms of (3.12) involving the electric field E because we now multiply by ik_j instead of dividing by ik_j in the expression equivalent to (3.19). This difference arises because $E = -\partial\Phi/\partial z$ is now calculated by integrating $\Phi_{zz} = \sum_{j=-\infty}^{\infty} a_{0,j}(t)e^{ik_j z}$ rather than by differentiating $\Phi = \sum_{j=-\infty}^{\infty} a_{0,j}(t)e^{ik_j z}$ as before. Note that the Laplacian in (4.4) and negative electron charge in (4.3) together ensure that linear damping still occurs. The collisional matrix-vector expression (3.37) holds for classical electrostatics (superscript CE) with the electrostatic terms redefined as follows,

$$\dot{\mathbf{a}}^{\mathbf{CE}} = i(\mathbf{M}\mathbf{a}^{\mathbf{CE}} + \mathbf{y}^{\mathbf{CE}} + \mathbf{L}^{\mathbf{CE}}) + \mathbf{C}, \tag{4.5}$$

$$y_{p,g}^{CE} = -\frac{\sqrt{2p}}{\Delta k} \sum_{j \neq g} \frac{a_{0,g-j}^{CE}}{g-j} a_{p-1,j}^{CE}, \tag{4.6}$$

$$L_{p,g}^{CE} = -\frac{\sqrt{2}}{\Delta k} \frac{a_{0,g}^{CE}}{g} \delta_{p,1} \bar{\delta}_{g,0}. \tag{4.7}$$

The matrix $\mathbf{M}$ and general collision operator $\mathbf{C}$ are unaffected by these changes. A full set of calculations may be found in Appendix F.

4.2 Linear V-P Results

The following results were obtained by solving the ODE system (4.5) describing a collisional V-P system using the approach described in Section 3.4.

4.2.1 Dispersion Results

Our first set of results investigates the degree to which the numerical model we have derived for the V-P system agrees with the linear Landau damping theory of Section 1.3.1. We compare the electric field frequency and growth rate output by the Fourier-Hermite model with the results of a highly accurate numerical solution of the exact theoretical dispersion relation described in Appendix B.3. Because the electric field is directly proportional to the spatial variation of the distribution function for a single excited Fourier mode, we use the electric field growth rate and frequency to assess those of the distribution function. Numerical frequencies and growth rates from the Fourier-Hermite model are calculated by locating the peaks of the numerically computed electrical field and fitting a straight line to these points. The slope of

this line is taken as the numerical growth rate, and the time between successive peaks gives the frequency as in Heath et al. (2012). We use a scaled parallel length of $L_N = 4\pi$ and an initial amplitude $A = 10^{-1}$ for the single symmetric pair of analogous positive and negative Fourier modes we choose to excite. We generally activate spatial wavenumbers $k = 1$ and $k = -1$, representing an established sinusoidal wave within the plasma (Armstrong, 1967). We use hypercollisionality with $n = 8$ and $\nu = 75$ to illustrate that this selective damping of the Hermite spectrum does not alter the key features of the linear problem. We use 80 Hermite modes and 60 Fourier modes for these calculations. This choice gives a convenient compromise between accuracy and computational speed, the validity of which is confirmed by the good agreement between numerics and theory shown in Fig. 4.1. We see excellent agreement across a

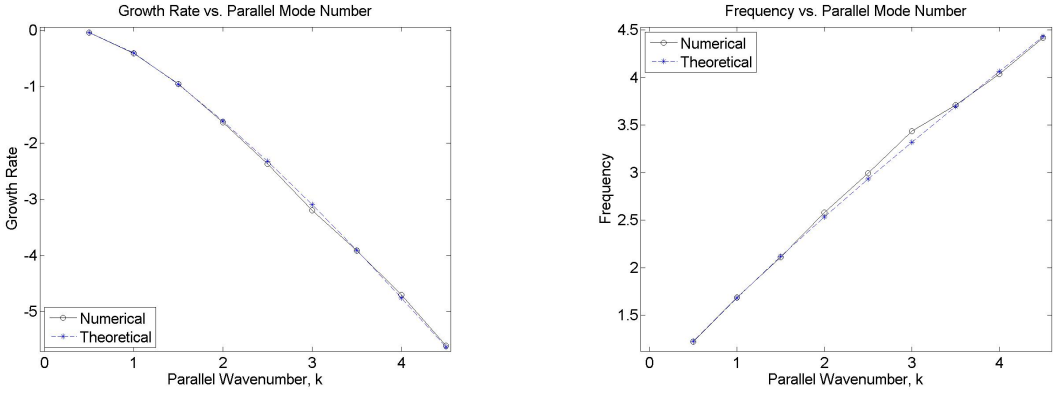

(a) Growth Rate (b) Frequency

Figure 4.1: V-P linear response with hypercollisions and exact dispersion function.

relatively large band of wavenumbers, suggesting that both our analysis of the Landau damping and our implementation of the Fourier-Hermite computational model of the linear V-P system are correct. Plots of the relative error between the linear V-P results of this Fourier-Hermite model and our numerical solution of the exact theoretical dispersion relation may be found in Appendix B.4.[2] The majority of our numerical values are within 2% of the exact dispersion values for both frequency and growth rates, with a few exceptions that do not deviate by more than 7% from the true value. The higher deviations in certain cases are likely artifacts of potential errors introduced both by the iterative method used to solve the exact dispersion relation and slight inaccuracies in the peak-finding algorithm that prescribes the data points used to extract dispersion results from the Fourier-Hermite model.

[2]Appendix B.5 contains analogous results that compare our linear V-P numerics to the weak damping series approximation of (1.24a) and (1.24b) for low k, showing that the series approximation becomes highly inaccurate for $k \sim 1$, as expected.

4.2.2 Collisionality and Recurrence Results

We now proceed to illustrating explicitly why hypercollisionality is necessary to achieve useful results over long time frames. Figure 4.2 shows the Hermite space representation of the distribution function over time in the collisionless case under the same initial conditions as the previous section except for the activation of the second Fourier modes wherein energy cascades more quickly to high Hermite modes. All values in Fig. 4.2 have been normalized by the maximum Hermite coefficient at each timestep.

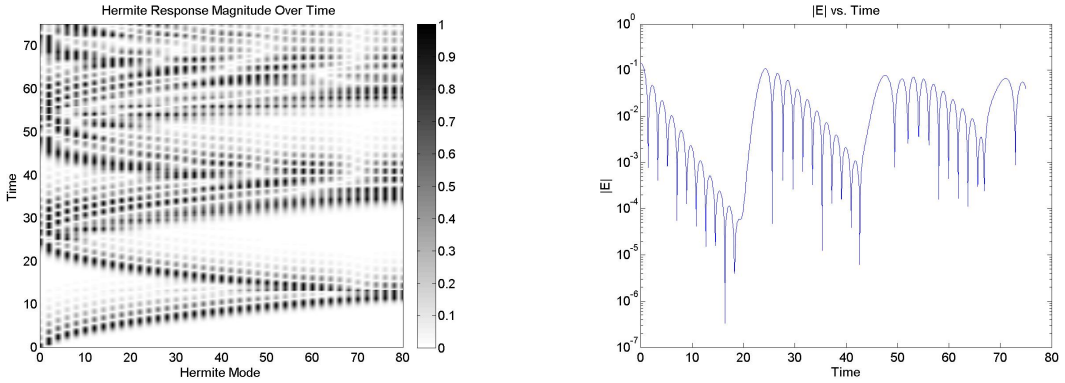

(a) δf_1 in Hermite Space

(b) Electric Field

Figure 4.2: Linear second Fourier mode collisionless V-P response.

Figure 4.2(a) shows the rapid movement of energy from the first Hermite mode to the very highest Hermite modes by approximately $t = 10$. The energy then reflects off the highest mode and returns towards the lowest modes by around $t = 20$. This behavior repeats as time goes forward. The return of reflected energy to the lowest mode leads to jumps in the electric field, a phenomenon known as "recurrence." Such behavior is a numerical artifact due to truncation of the Hermite spectrum, as opposed to a phenomenon with any physical meaning (such as plasma echoes). Fortunately, appropriately implemented hypercollisions appear to solve this problem rather nicely, as documented by Parker and Dellar (2012) and others. We see this behavior in our hypercollisional results presented in Fig. 4.3, where the electric field decays continuously without recurrence and the Hermite spectrum maintains a constant form after an initial period of transience. We therefore utilize this hypercollisional framework in all following numerical results to ensure that the highest modes are appropriately damped and that recurrence does not occur. This allows us to perform accurate linear and nonlinear calculations over long time periods.

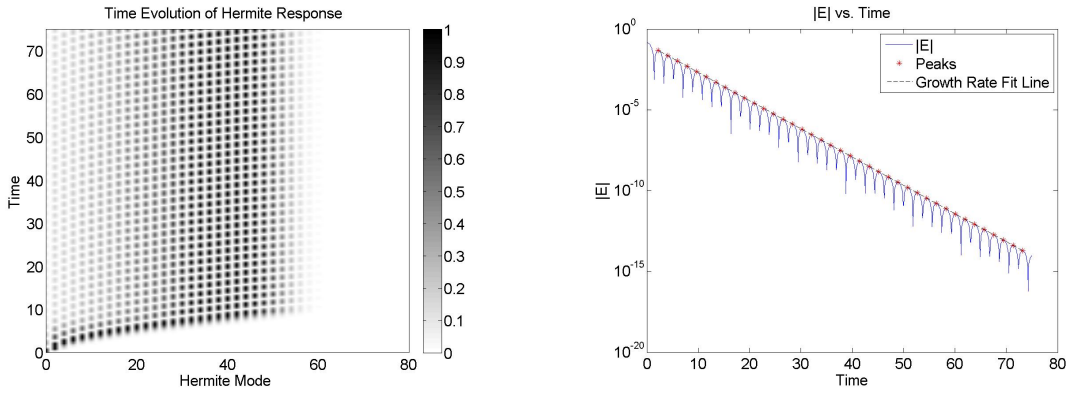

(a) δf_1 in Hermite Space

(b) Electric Field

Figure 4.3: Linear second Fourier mode hypercollisional V-P response.

4.2.3 Distribution Function Results

Finally, it is useful to visualize the effect that the onset of Landau damping and collisional interaction has on the time evolution of the distribution function, which requires us to perform inverse Fourier and Hermite transforms of our spectrally defined δf_{1e}. Computations akin to those used to create Figs. 4.2 and 4.3 reveal that the collisionless recurrence time is just under 40 normalized time units when the first Fourier modes are activated in place of the second pair.[3] All other parameters used in this calculation are the same as those in earlier simulations.[4]

The first important result we present is the full visualization of the distribution function evolution in the collisionless case found in Fig. 4.4. As time goes on, the distribution function develops continually finer scales in velocity space until the disturbance reaches the highest mode at approximately half of the recurrence time,[5] at which point the collisionless results cease to hold any validity. This development of successively finer scales as time goes on is a process generally known as "filamentation" (Heath et al., 2012). Analogous results for the hypercollisional case with $\nu = 75$ can be found in Fig. 4.5. The behavior at times just before and just after the disturbance reaches the highest mode is markedly different. Specifically, we see some fine scale structures remaining in velocity space after the onset of hypercollisions at the collisionless half-recurrence time $t \approx 20$, but a distinctly low wavenumber response remains as well. As expected, enforcing appropriate levels of hypercollisionality begins to pull energy out of the system through the highest Hermite modes as it smooths

[3]These results are omitted for brevity. The reader can find them in Appendix G.1.

[4]We do not present analogous results for normal Dougherty collisions here only for the sake of brevity. Such results and a brief analysis can, however, be found in Appendix G.2.

[5]We refer to this as the "half-recurrence time" from hence forth.

very fine scales in velocity space, as indicated by the fact that the δf_{1e} in the bottom right panel of Fig. 4.5 is of generally lower magnitude than at pre-half-recurrence times. It is likely that this hypercollisional energy bleedoff at the highest wavenumbers causes fine scale structures to become less important relative to the coarse scale velocity space structures at post-half-recurrence times.

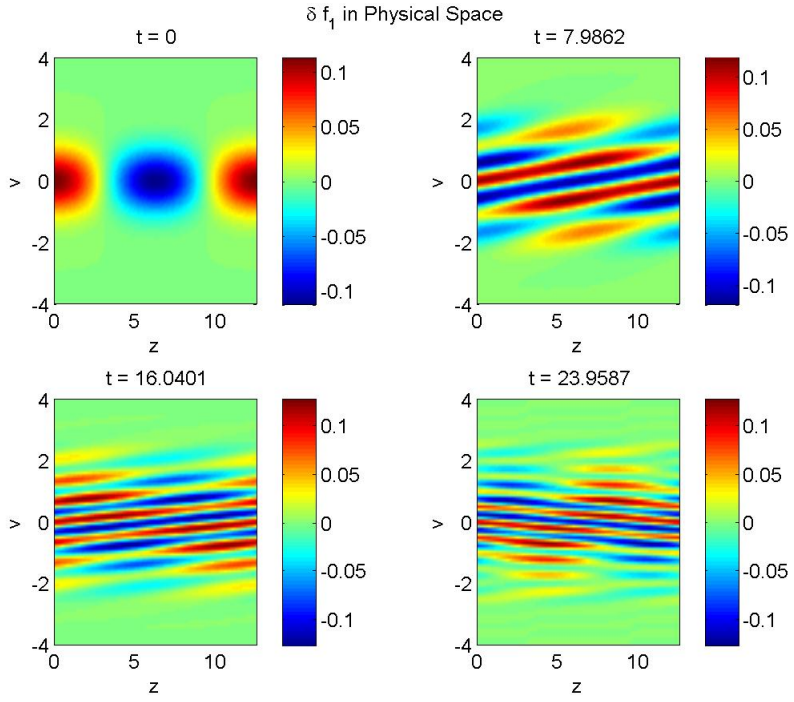

Figure 4.4: Linear collisionless time evolution of V-P δf_1.

As a final benchmark of this linear code, we compare the our results to similar ones calculated by a different numerical method in the work of Heath et al. (2012). Results computed for linear Landau damping of the V-P system with a background Maxwellian distribution in Figure 3 of Heath et al. (2012) display good qualitative agreement with those in Fig. 4.4 in terms of Landau damping behavior and development of fine velocity scales. Notable differences, however, are that Heath et al. (2012) develop much finer scales in velocity space and rely on a discontinuous Galerkin discretization to provide sufficient numerical dissipation. Any discrepancy in qualitative results is mostly due to Heath et al. (2012) using much higher position and velocity space resolutions than we do here. Transferring our model from MATLAB to a Fortran or C based code would likely allow us to use comparable resolution and obtain more similar results to Heath et al. (2012). Overall, however, our linear V-P results agree well with those obtained from both the literature and theoretical analysis.

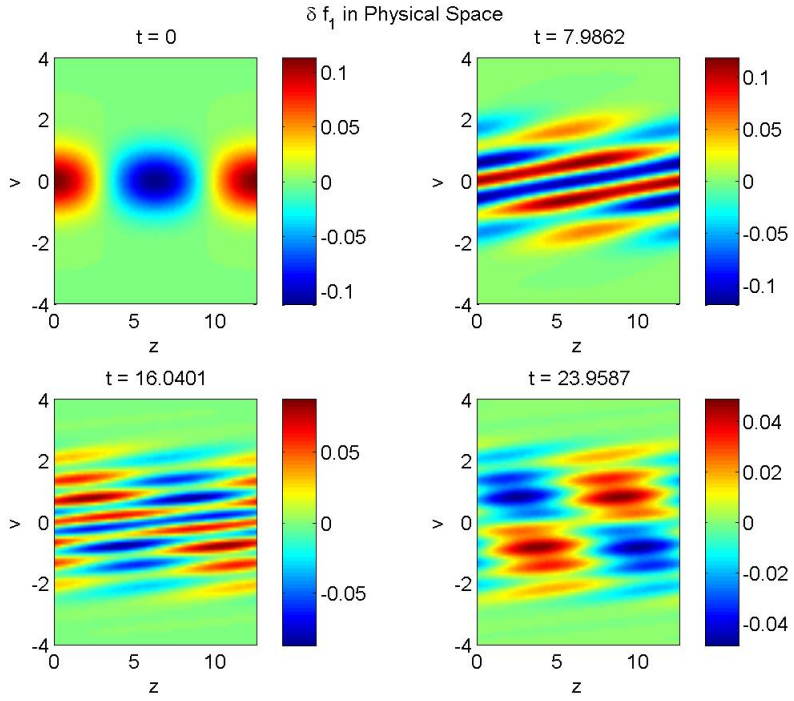

Figure 4.5: Linear hypercollisional time evolution of V-P δf_1.

4.3 Nonlinear V-P Results

We also verify our nonlinear code by comparing our results to those of Heath et al. (2012) using the same parameters as in the hypercollisional linear case. We see in Figs. 4.6(a) and 4.6(b) that energy moves throughout Hermite space in a complex pattern as time goes on, with a significant amount remaining trapped in several of the lowest modes. We also observe significant activity in a number of Fourier modes beyond the first mode that was initially excited, indicating that spatial nonlinearity has substantial effects on the system. This behavior leads to a significant contribution from higher Fourier modes to the overall electric field, as shown in Fig. 4.7. Finally, the Fourier space behavior is completely symmetric, meaning that our presentation of the first four positive wavenumber Fourier modes of the electric field is not omitting crucial behavior in the negative wavenumber modes. This symmetric behavior is in fact required to appropriately represent a real field with a complex Fourier expansion.

This particular simulation proves quite useful in validating our nonlinear code because our results can be directly qualitatively compared to Figure 6 of Heath et al. (2012), which shows analogous results generated under slightly different normalization and initial conditions. Our results in Fig. 4.7 appear to agree rather well with those of Figure 6 in Heath et al. (2012) in a qualitative sense, particularly in the first mode.

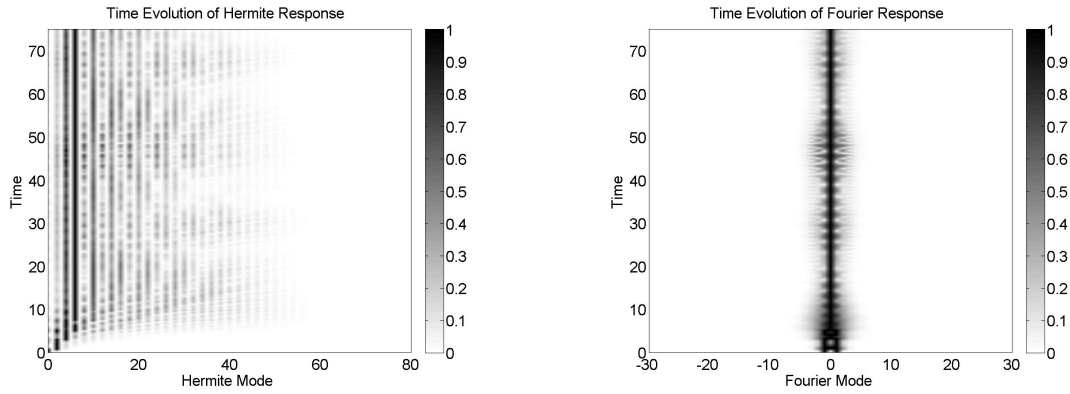

(a) δf_1 in Hermite Space

(b) δf_1 in Fourier Space

Figure 4.6: Nonlinear V-P response in Hermite and Fourier spaces.

While we do see significant activation of the higher modes in this case, Fig. 4.7 suggests that the first mode still dominates the behavior of the total electric field, which is, notably, not uniformly damped at large times but in fact appears to oscillate at a relatively constant magnitude over time, as also found by Heath et al. (2012). Modes two through four also show good qualitative agreement with Heath et al. (2012) in displaying a steep initial drop followed by an increase back to near the initial value before settling out to what appears to be a nonlinear oscillation about a weak long term damping trend. The absolute and relative magnitudes of the modal responses we see here also agree relatively well with Heath et al. (2012). Though our results do indicate a slightly lower overall damping rate in the higher modes over the long run, we see enough agreement between our computations and those of Heath et al. (2012) to be relatively confident in the accuracy of our results, particularly given aforementioned differences in resolution, normalization, and initial conditions.

As a final check of numerical validity, in Fig. 4.8 we plot the Fourier-Hermite coefficients of magnitude greater than 10^{-10} at various points in time to ensure that the coefficients we ignore through truncation are always indeed negligibly small. Objectively, we ensure that the maximum coefficient of the highest Hermite mode is always smaller than 10^{-7} in all nonlinear simulations by plotting the time evolution of this maximum highest Hermite coefficient. These highest Hermite coefficient plots are generally omitted for brevity, but the plot used for the current simulation can be found in Appendix G.3. While the results of this section are not particularly important in this study outside of the code benchmarking process, it will be useful to compare them to the quasineutral system modeled later to observe differences in the system dynamics resultant from changes in the electrostatic coupling.

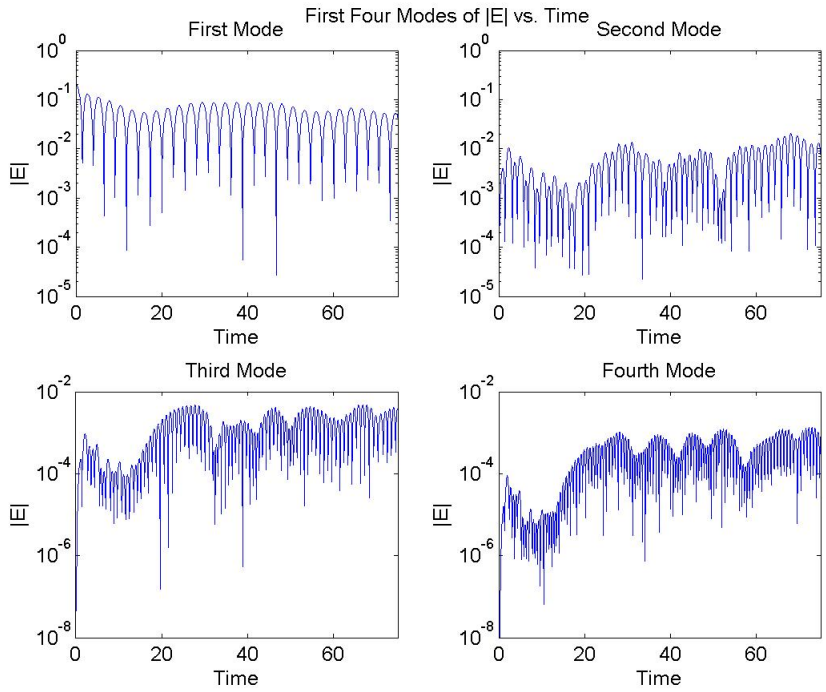

Figure 4.7: Nonlinear time evolution of V-P Fourier modal $|E|$.

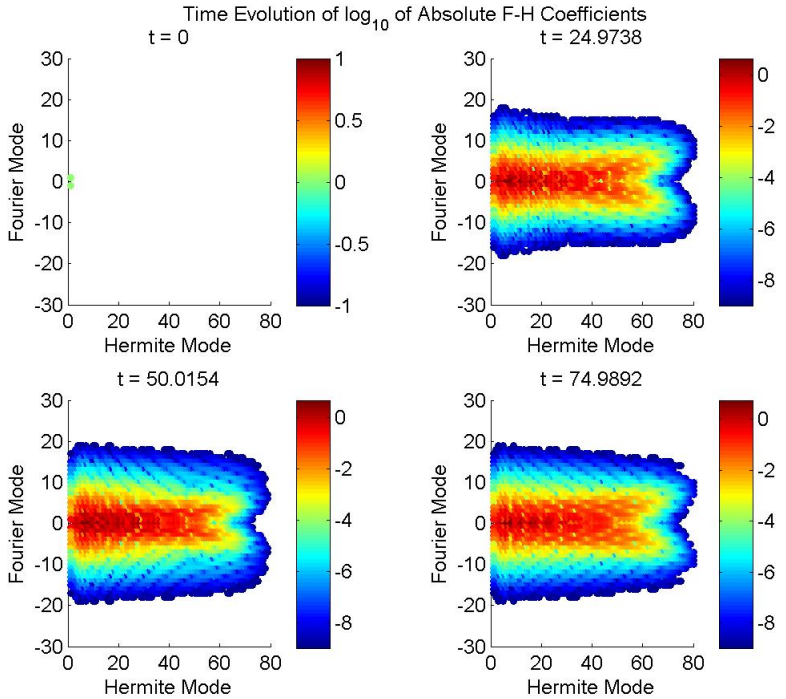

Figure 4.8: Nonlinear time evolution of V-P Fourier-Hermite coefficients.

Chapter 5

Simulations of 1+1-D Quasineutral Plasmas

Now that our computational methods have been validated for a collisional Vlasov-Poisson system, we proceed to use them to investigate the dissipative behavior of a two-species fusion plasma described by the collisional Vlasov-Quasineutral system.

5.1 Quasineutral Linear Theory

We must adjust our analysis of Landau damping in Section 1.3.1 for quasineutral plasmas. We first reformulate (1.17) for ions instead of electrons in a two-species plasma,

$$\delta f_{1i} = -\frac{ieE_z}{m_i}\frac{\partial F_0}{\partial v}\frac{1}{\omega - kv}, \tag{5.1}$$

where as usual we take $q_i = -q_e = e$. Similarly, we replace (1.18) with the following relation,

$$E_z = -\frac{\partial \Phi}{\partial z} = -\eta\frac{k_B T_i}{e}\int_{-\infty}^{\infty}\frac{\partial \delta f_{1i}}{\partial z}\mathrm{d}v = -ik\eta\frac{k_B T_i}{e}\int_{-\infty}^{\infty}\delta f_{1i}\mathrm{d}v, \tag{5.2}$$

as derived from the non-normalized version of the quasineutrality condition (3.13). Combining (5.1) and (5.2) gives the following dispersion relation in terms of v_{th_i},

$$1 \;=\; \eta\frac{v_{th_i}^2}{2}\int_{-\infty}^{\infty}\frac{\partial F_0/\partial v}{v - \frac{\omega}{k}}\mathrm{d}v. \tag{5.3}$$

We now use the same dispersion function analysis from Section 1.3.1 by changing variables to obtain the dispersion relation in terms of $\zeta \equiv \omega/kv_{th_i}$,

$$1 + \eta[1 + \zeta Z(\zeta)] = 0, \tag{5.4}$$

as in Howes et al. (2006). Equation (5.4) gives insight into the physical differences between the V-Q and V-P systems. The V-Q result reduces to the normalized version of the V-P dispersion relation (1.22) if one assumes a wavenumber-dependent temperature ratio $\eta = 2/k^2$. We can solve the exact dispersion relation numerically as before to assess the accuracy of our linear numerical simulations. It is also instructive to continue the analysis for the weak damping case. Again using the asymptotic expansion (1.23) for $|\zeta| \gg 1$, $|\mathrm{Im}(\zeta)| < |\mathrm{Re}(\zeta)|^{-1}$ and keeping only the leading term in both the real and imaginary parts ζ, we recover,

$$\mathrm{Re}(\omega) \approx \sqrt{\frac{\eta}{2}} k v_{th_i}, \ \mathrm{Im}(\omega) \equiv \gamma \approx -\frac{\eta^2}{4} i \pi^{1/2} k v_{th_i} e^{-\eta/2}. \tag{5.5}$$

While we omit detailed derivations of (5.4) and (5.5) for brevity, these calculations may be found in Appendix B.6.

We now see from (5.5) that both frequency and growth rate are directly dependent on the wavenumber and temperature ratio in a quasineutral plasma. It also becomes apparent that Landau damping of the quasineutral plasma is negligible in the cold ion case wherein $1 \ll \eta$ and $T_i \ll T_e$. This result is well aligned with established theory on the ion acoustic wave that generally dominates our V-Q system (Dendy, 1993). Importantly, these approximations suggest that we should expect the Landau damping rate of waves in the V-Q system to increase strongly at higher wavenumbers.

5.2 Linear V-Q Results

With these results in hand, we can proceed to evaluating the linear behavior of our model of the collisional V-Q system which, as previous sections have shown, closely resembles our well-validated collisional V-P model. We therefore expect accurate and insightful results from both the linear and nonlinear simulations.

5.2.1 Dispersion Results

The dispersion results we present here compare the numerical solution of the exact dispersion relation derived above to the numerical results of our Fourier-Hermite model of the V-Q system, which has been run under the exact same conditions as the V-P linear analysis in Section 4.2, except for a decrease in ν from 75 to 25. We observe excellent agreement between the theoretical and Fourier-Hermite results in Fig. 5.1, thereby validating our analysis of the quasineutral dispersion relation in addition to our derivation and implementation of the linear portion of our numerical

V-Q model. We again note that the hypercollisional numerics agree with the linear theory and present the relative error plots between our numerical Fourier-Hermite results and exact dispersion computations for the V-Q system in Appendix B.7.

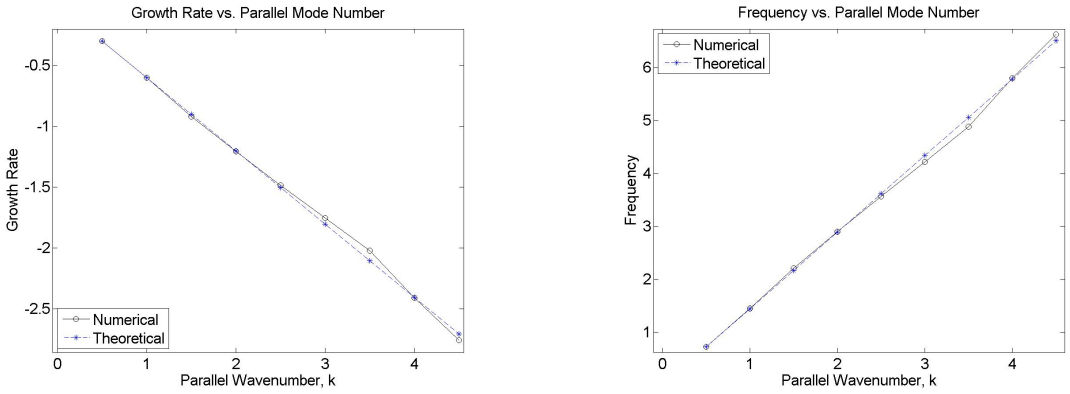

(a) Growth Rate (b) Frequency

Figure 5.1: V-Q linear response with hypercollisions and exact dispersion function.

5.2.2 Hermite Space Evolution

We also expect similar results to those in Section 4.2 in terms of how well hypercollisions prevent recurrence. Figure 5.2 illustrates the evolution of the distribution function in Hermite space, as well as that of the electric field, for initial conditions with the first Fourier modes $k = \pm 1$ activated. As hoped, recurrence does not occur.

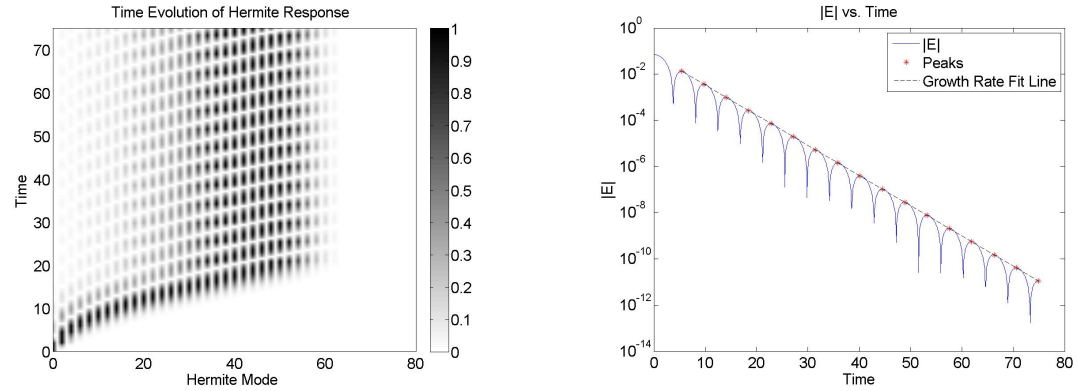

(a) δf_1 in Hermite Space (b) Electric Field

Figure 5.2: Linear first Fourier mode hypercollisional V-Q response.

5.2.3 Distribution Function Results

The distribution function results are perhaps the most insightful in illustrating how the V-Q system differs from the V-P system. We see sharper fine scale structures and similar levels of filamentation developing in the V-Q distribution function of Fig. 5.3. These fine scale structures are retained after hypercollisions become significant at the collisionless half-recurrence time at $t \approx 20$, indicating that, unlike in the classical V-P case, phase space shear remains important even in the presence of collisionality.

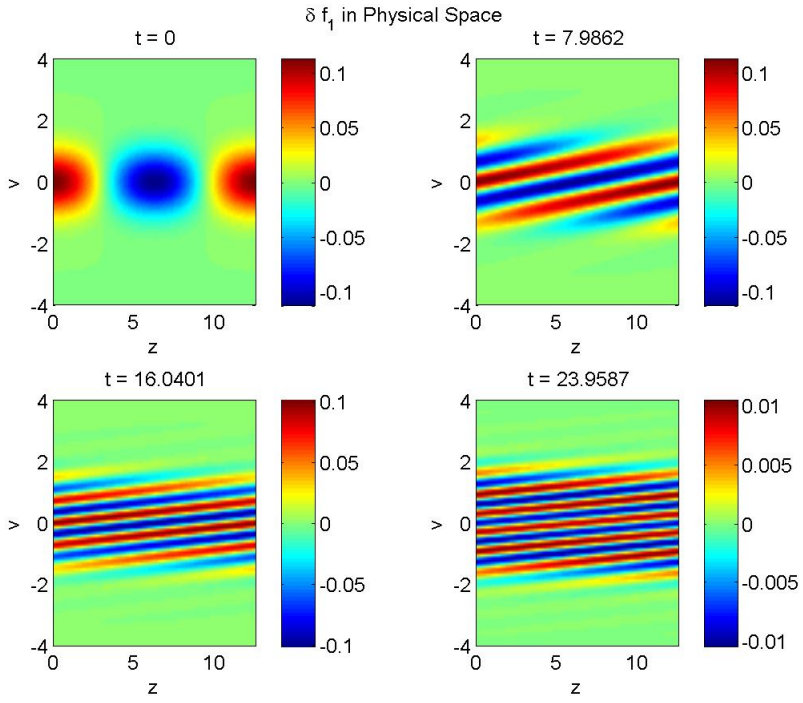

Figure 5.3: Linear hypercollisional time evolution of V-Q δf_1.

5.3 Nonlinear V-Q Results

Our previous validation of the linear V-Q and nonlinear V-P codes reflects encouragingly on the accuracy of our following nonlinear V-Q results. We use utilize exactly the same parameters as in the previous V-P simulations with the slight change that we can reduce hypercollisions to $\nu = 25$. Confirmation of appropriate truncation behavior in the numerical Hermite spectrum with $\nu = 25$ can be found in the Fourier-Hermite coefficient time evolution plots presented in Appendix D.5.

The nonlinear V-Q Hermite spectrum in Fig. 5.4 shows that a persistent eigenmode appears to develop at approximately $t = 25$. The Fourier spectrum collapses to its

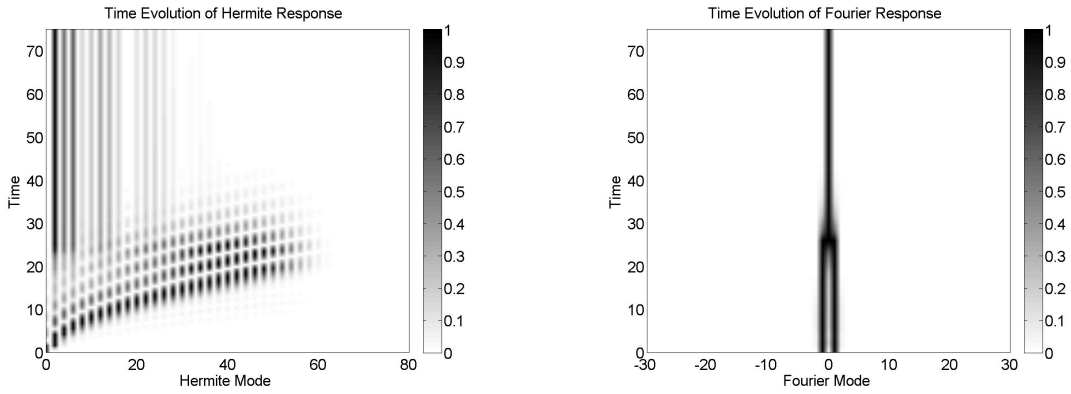

(a) δf_1 in Hermite Space

(b) δf_1 in Fourier Space

Figure 5.4: Nonlinear V-Q response in Hermite and Fourier spaces.

lowest modes exactly when this eigenmode develops. The lower electric field modes also appear to be significantly more damped in the V-Q case than in the classical V-P system. As shown in Fig. 5.5, all modes are Landau damped at a wavenumber-dependent rate that is relatively constant in time. These results are in agreement

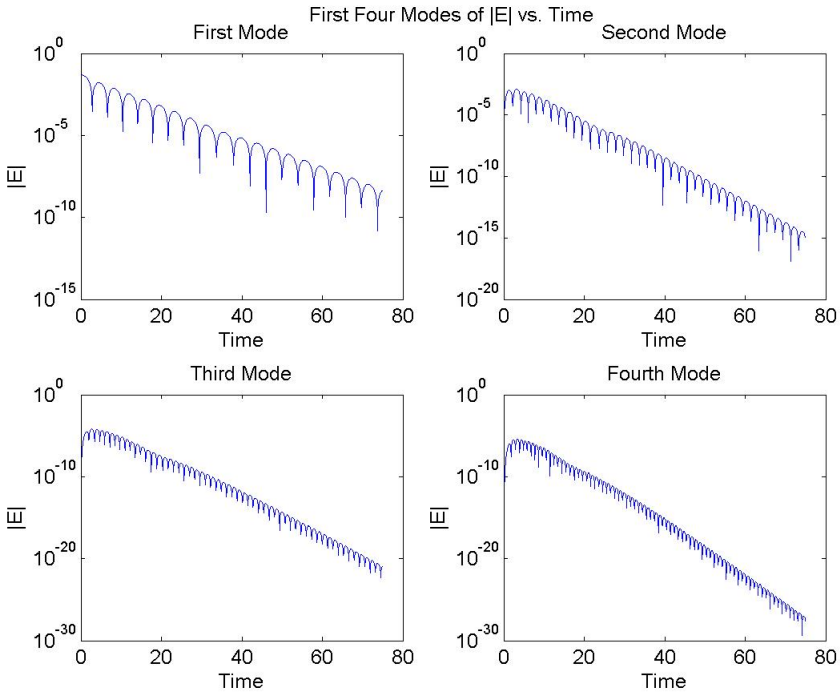

Figure 5.5: Nonlinear time evolution of V-Q Fourier modal $|E|$.

with the general fact that the ion acoustic wave, the dominant wave modeled by this particular V-Q system, is strongly Landau damped (Dendy, 1993).

The results of Fig. 5.6 give excellent insight into the development of a persistent eigenmode in this system. We have seen from Fig. 5.4 that the dominant eigenmode is beginning to emerge at $t = 25$ when the second distribution function snapshot is shown. We therefore see at $t = 25$ in Fig. 5.6 an intermediate point between the Landau damping profile we observe at earlier times and that of the later persistent eigenmode. The fact that the graphs at $t = 50$ and $t = 75$ are identical confirms that the eigenmode has constant structure over time. The z-independent steady state seen at $t = 50$ and $t = 75$ is in line with expected system behavior. Specifically, the second term in (3.12) explicitly vanishes and the two electrostatic terms vanish because $E \sim \partial \delta f_{1i}/\partial z$ from (3.13). Thus, if a z-independent state is ever reached, it remains as a steady state, like that seen in the two lower plots of Fig. 5.6.

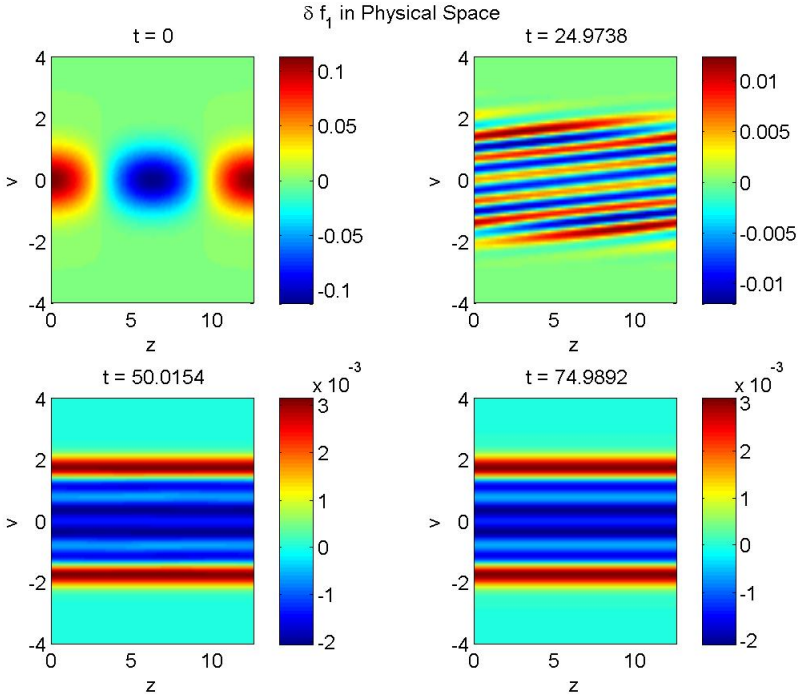

Figure 5.6: Nonlinear time evolution of V-Q δf_1.

Our nonlinear V-Q results, then, are well in line with established theory on ion sound waves, our expectation that Landau damping should dominate the dissipative dynamics of the quasineutral plasma, and basic implications of a z-independent V-Q system. We will use this physically and numerically validated nonlinear V-Q code as the basis of following simulations of the behavior of a forced quasineutral plasma, which represent the ultimate goal of this study.

Chapter 6

Driven Fusion Dynamics

We now investigate the response of a collisional, quasineutral two-species plasma to forcing from a neutral particle beam. In addition to representing the external apparatus that is often used to drive a tokamak, we use this forcing mechanism as a model for the omitted perpendicular dynamics.

6.1 Driving the Numerical Fourier-Hermite Model with Neutral Particles

We introduce an additional forcing term $\mathbf{F}$ to the right hand side of (3.37) so that the matrix-vector equation for our Fourier-Hermite model of the V-Q system becomes,

$$\dot{\mathbf{a}} = i(\mathbf{M}\mathbf{a} + \mathbf{y} + \mathbf{L}) + \mathbf{C} + \mathbf{F}. \tag{6.1}$$

A viable definition of $\mathbf{F}$, which of course has the same dimensions as all other vectors in (6.1), describes the drag resultant from plasma collisions with frequency $\bar{\nu}$ with a neutral particle beam with bulk velocity $\bar{u}$,

$$F = \bar{\nu}\frac{\partial}{\partial v}(v\delta f_{1i} - \bar{u}F_0). \tag{6.2}$$

This definition of F effectively corresponds to augmenting the VFP equation with an an additional Fokker-Planck drag term that can describe neutral particle forcing from both internal and external phenomena. We use the ansatz (3.17) to define δf_{1i} and use $F_0 = \phi_0$ to rewrite (6.1) as,

$$F = \bar{\nu}\left(\sum_{\substack{n=0,\\ j=-\infty}}^{\infty} a_{n,j}\phi_n e^{ik_j z} + \sum_{\substack{n=0,\\ j=-\infty}}^{\infty} a_{n,j} v\phi_n^{'} e^{ik_j z} + 2\bar{u}v\phi_0\right). \tag{6.3}$$

We then invoke the recurrence relations of (3.21) – (3.23) while writing $\bar{u} = \sum_{j=-\infty}^{\infty} \bar{U}_j(t) e^{ik_j z}$ as a Fourier series with time-dependent coefficients to obtain,

$$F = \bar{\nu} \sum_{\substack{n=0,\\ j=-\infty}}^{\infty} \left(a_{n,j}\phi_n - \sqrt{2n+2}a_{n,j} \left[\sqrt{\frac{n+2}{2}}\phi_{n+2} + \sqrt{\frac{n+1}{2}}\phi_n \right] + \sqrt{2}\bar{U}_j\phi_1 \right) e^{ik_j z}. \quad (6.4)$$

Taking the inner product with the p^{th} Hermite function and g^{th} Fourier mode gives,[1]

$$F_{p,g} = \frac{1}{2L_g} \int_{-\infty}^{\infty} \int_{-L_g}^{L_g} F\phi^p e^{-ik_g z} \mathrm{d}z\mathrm{d}v = \bar{\nu} \left(\sqrt{2}\bar{U}_g \delta_{p,1} - p a_{p,g} - \left[\sqrt{p^2 - p} \right] a_{p-2,g} \right). \quad (6.5)$$

6.2 Driven V-Q Simulation Results

We now investigate forcing with random white noise, with a single Fourier mode at the resonant frequency, and with white noise with an underlying resonant frequency. All parameters used here are exactly the same as those in Section 5.3, except for hypercollisions. These are increased to $\nu = 100$ in cases of white noise forcing because we are forcing even the highest Hermite modes, which we wish to ensure remain negligibly small. This parameter choice was made using numerical experiments and diagnostic plots akin to Fig. 4.8 to ensure that the highest modal coefficients always remain below 10^{-7}. We also set a relatively small $\bar{\nu} = \nu/200$ in each of these simulations so that the behavior is not dominated by the additional linear damping imposed by the forcing operator of (6.5).[2] We generally set the total magnitude of the vector $\bar{U}$ to $A/100$ so that our forcing is significant, but not comparable to the initial condition. Finally, additional plots of Fourier modal decompositions of the electric field for each case may be found in Appendix H.

6.2.1 Forcing with Random White Noise

Understanding how the V-Q system responds to random white noise forcing may give insight into the response of the parallel dynamics to turbulence taking place in the perpendicular dimensions. We force the system with white noise by initiating $\bar{U}$ as a randomly generated vector of numbers between 0 and 1 and multiplying by a normalization factor appropriate to our choice of ν and $\bar{\nu}$. This initial vector defines the amplitude of each $\bar{U}_g$. We next assign to each $\bar{U}_g$ a random frequency generated in a similar fashion. Our time-dependent forcing is then defined by multiplying each

[1] A detailed derivation of (6.5) may be found in Appendix H.1.
[2] This comes out to $\bar{\nu} = 0.5$ for white noise forcing and $\bar{\nu} = 0.125$ otherwise.

$\bar{U}_g$ by the analogous random frequency sinusoid at each point in time. As we see in Fig. 6.1, the V-Q response to random white noise is usually simple decay to a persistent eigenmode, but one that differs from the unforced case. In the end, random white noise forcing still ultimately results in a z-independent eigenmode that changes very little over time.

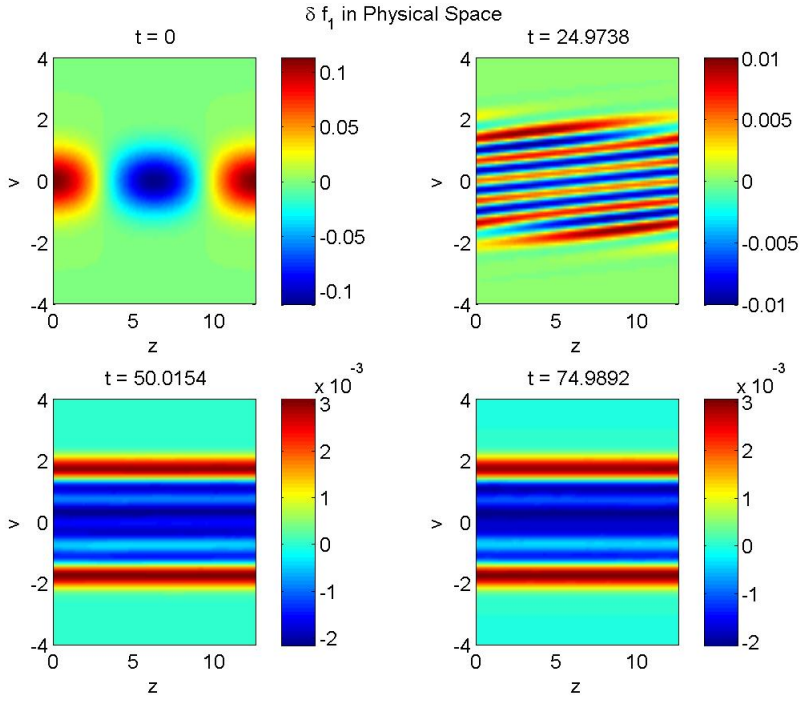

Figure 6.1: Nonlinear time evolution of V-Q δf_1 under white noise forcing.

6.2.2 Forcing at Linear Resonance

Driving the V-Q system at its natural linear oscillation frequency yields a more interesting response. Such a perturbation should cause a higher amplitude response through resonance behavior, and could perhaps cause enough disturbance to overcome dominance of the system dynamics by Landau damping to a z-independent eigenmode. The results presented in Fig. 6.2 are generated by numerically solving the exact V-Q dispersion relation (5.4) for the characteristic frequency of the linear system and then inserting that frequency directly into the forcing term for the first pair of Fourier modes, denoted by $\bar{U}_1$ and $\bar{U}_{-1}$, with amplitudes as designated above. In these results, we see a persistent response of significantly higher amplitude than in the previous white noise case after Landau damping has occurred for the first 25 normalized time units and, moreover, we observe a distinctly different structure evolving

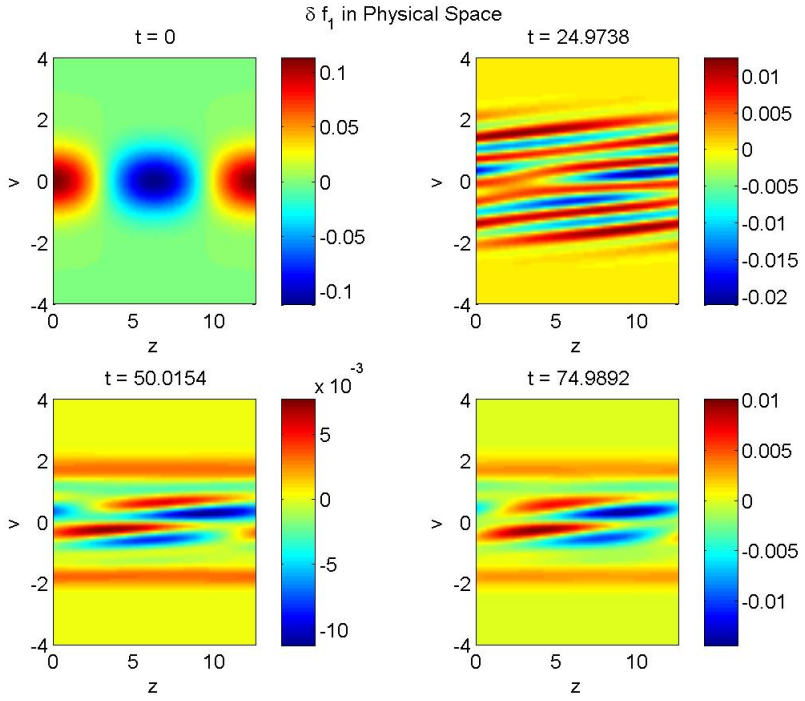

Figure 6.2: Nonlinear time evolution of V-Q δf_1 under resonant forcing.

in the distribution function. Specifically, while the distribution function at $t = 25$ displays filamentation vaguely reminiscent of that caused by pure Landau damping, it is in a state of transition towards a persistent response dominated by the resonant forcing, which appears for $t > 25$. The bottom two panels of Fig. 6.2 in particular illustrate that a z and t dependent response develops in the large time limit.

6.2.3 White Noise Forcing with Linear Resonance Activation

Thus, while it is possible that resonant single mode forcing could incite behavior desired by tokamak engineers, it is also difficult to practically implement such precise single mode forcing with external mechanisms. We therefore perform a last study of the V-Q response to the same white noise signal utilized above, except that $\bar{U}_1$ and $\bar{U}_{-1}$ are overlaid with the resonant forcing of the previous section at a magnitude similar to that of the other modes in the white noise signal. As we see in Figs. 6.3 and 6.4, the imposition of white noise forcing containing an underlying resonant signal causes the magnitude of the persistent electric field to decrease over time until the resonant response dominates in the large time limit. Even with resonant forcing acting in concert with many forcing waves of different frequencies and similar amplitudes, it does eventually come to dominate the persistent response around $t = 50$. Moreover,

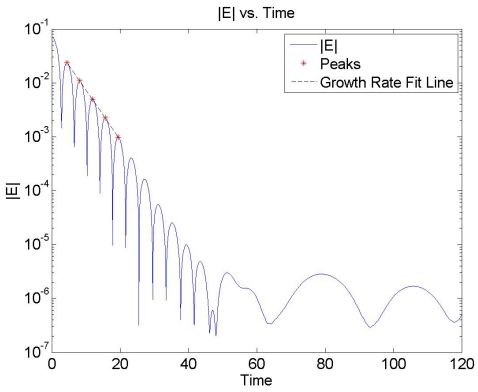

Figure 6.3: Nonlinear time evolution of V-Q $|E|$ under resonant white noise forcing.

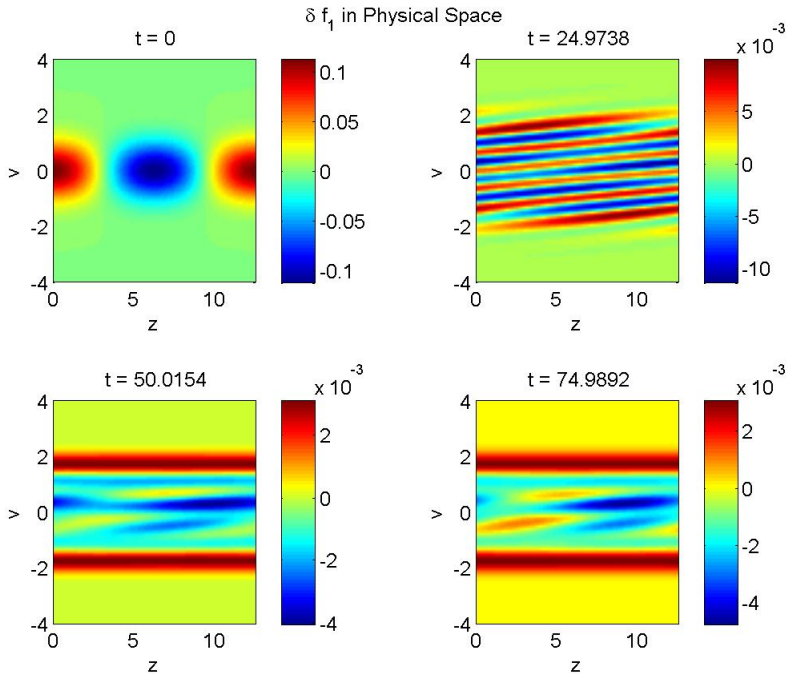

Figure 6.4: Nonlinear time evolution of V-Q δf_1 under resonant white noise forcing.

the bottom two panels of Fig. 6.4 show that even this relatively small level of forcing at linear resonance can cause persistent z and t dependence in the distribution function.

Ultimately, then, neutral particle forcing as implemented here represents a model for the effects of both external system excitation and missing dynamics in the perpendicular degrees of freedom. Our results indicate that even a small resonance component in a forcing signal may be sufficient to substantially affect long term system response by causing persistent spatiotemporal dependence in the distribution function. This finding could hold significant import in further studies of fusion plasmas.

Chapter 7

Conclusions and Future Work

We have shown that it is possible to use a 1+1-D model of a multidimensional plasma to obtain useful insights into its dissipative characteristics. Beginning with the Vlasov-Maxwell equations for a two-species plasma comprising ions coupled to adiabatic electrons, we have derived the fully electromagnetic 5-D gyrokinetic framework. We have then further reduced these modeling equations to form a low dimensional system consisting of a collisional ion Vlasov equation coupled to the quasineutrality condition. Translation of this model to Fourier-Hermite space in concert with the use of hypercollisionality to ensure appropriate dissipation at the finest resolved scales has yielded promising results confirming that the 1+1-D quasineutral plasma is heavily Landau damped. Successful benchmarking of the model code against both rigorous linear theory and known nonlinear results lends significant credibility to these computations. Visualization of the distribution function has yielded a number of insightful conclusions about the true effects of hypercollisions and electrostatic coupling on the system dynamics.

Extension of the 1+1-D Vlasov-Quasineutral model to include various patterns of neutral particle forcing represents a significant addition to the current literature. We observe Landau damping to persistent spatially homogeneous eigenmodes under random white noise forcing. When even a weak signal near linear resonance is added to this noise, however, we observe a distinct change in the system dynamics that maintains persistent spatiotemporal dependence and stops the system from reaching a spatially homogeneous state. These results suggest that a detailed investigation of the effect of both perpendicular system dynamics and external forcing on the behavior of the parallel system using higher dimensional models would be a valuable use of resources. If these phenomena could indeed be understood more thoroughly using complicated, but more accurate multidimensional models, it could well lead to advances in turbulence mitigation in tokamak reactors.

Appendix A

List of Symbols

All quantities presented here are in terms of the Gaussian CGS unit system. Note that bold quantities denote vectors while normal text denotes scalars.

Symbol	Units	Description
0	-	Equilibrium subscript
$\mathbf{A}$	statV s cm^{-1}	Electromagnetic vector potential
α	cm^2 s^{-1}	Turbulent thermal diffusivity
$\mathbf{B}$	G	Magnetic field
β	-	Ratio of magnetic to gas pressure in a plasma
c	cm s^{-1}	Speed of light
η	-	Ion-electron temperature ratio
e	statC	Electron charge modulus and electron subscript
$\mathbf{E}$	statV cm^{-1}	Electric field
$\mathbf{F}_{EM}$	dyn	Electromagnetic force
f	-	Normalized velocity distribution function
γ	-	Growth rate
h	-	Perturbed gyrokinetic distribution function
H	-	Hermite polynomial
i	-	Ion species subscript
$\hat{\mathbf{j}}$	statC s^{-1} cm^{-3}	Current density
k	cm^{-1}	Spatial wavenumber
k_B	erg K^{-1}	Boltzmann constant
l_0	cm	Parallel fluctuation characteristic wavelength
L	cm	Macroscopic equilibrium plasma length scale
L_N	-	Length of periodic box in terms of l_0
λ_{De}	cm	Debye length
m	g	Particle mass
n	particles $\mathrm{cm}^{-\mathrm{D}}$	Particle number density with D spatial dimensions
ν	rad s^{-1}	Collision frequency
ω	rad s^{-1}	Parallel fluctuation frequency
ω_p	rad s^{-1}	Electron plasma frequency

ω_{pi}	rad s^{-1}	Ion plasma frequency
Ω	rad s^{-1}	Cyclotron frequency (gyrofrequency)
ϕ	-	Hermite function
Φ	statV	Scalar electric potential
q	statC	Particle charge
ρ	cm	Larmor radius (gyroradius)
$\hat{\rho}$	statC cm^{-3}	Charge density
$\mathbf{r}$	cm	Particle position (guiding center framework)
$\mathbf{R}$	cm	Guiding center position (guiding center framework)
s	-	General charged species subscript
t	s	Time
T	K	Temperature
τ	s	Turbulent heating timescale
θ	rad	Gryophase angle
u	cm s^{-1}	Bulk velocity
$\mathbf{v}$	cm s^{-1}	Particle velocity
$\mathbf{x}$	cm	Particle position
χ	statV	Gyrokinetic electric potential
$\hat{\mathbf{z}}$	-	Unit vector parallel to mean magnetic field

Appendix B

Analysis of Plasma Dispersion Relations

B.1 Expression of the V-P Dispersion Relation by Means of the Plasma Dispersion Function

We begin by combining (1.19) and (1.20) to obtain,

$$1 = \frac{\omega_p^2}{k^2}\frac{1}{v_{th_e}^3}\frac{1}{\sqrt{\pi}}\int_{-\infty}^{\infty}\frac{-2ve^{-v^2/v_{th_e}^2}}{v-\frac{\omega}{k}}\mathrm{d}v. \tag{B.1}$$

Changing variables within the integral to $u \equiv v/v_{th_e}$ and $\zeta \equiv \omega/kv_{th_e}$ gives,

$$1 = \left(\frac{\omega_p^2}{k^2 v_{th_e}^2}\right)\left(-2\left[\frac{1}{\sqrt{\pi}}\int_{-\infty}^{\infty}\frac{ue^{-u^2}}{u-\zeta}\mathrm{d}u\right]\right). \tag{B.2}$$

Temporarily changing variables in (B.2) to $y = u - \zeta$ and using the well known result that $\int_{-\infty}^{\infty} e^{-x^2}\mathrm{d}x = \sqrt{\pi}$ gives an expression for the quantity in square brackets in (B.2) in terms of the plasma dispersion function,

$$\begin{aligned}
\frac{1}{\sqrt{\pi}}\int_{-\infty}^{\infty}\frac{ue^{-u^2}}{u-\zeta}du &= \frac{1}{\sqrt{\pi}}\int_{-\infty}^{\infty}\frac{(y+\zeta)e^{-(y+\zeta)^2}}{y}\mathrm{d}y, \\
&= \frac{1}{\sqrt{\pi}}\int_{-\infty}^{\infty}e^{-(y+\zeta)^2}dy + \zeta\frac{1}{\sqrt{\pi}}\int_{-\infty}^{\infty}\frac{e^{-(y+\zeta)^2}}{y}\mathrm{d}y, \\
&= 1 + \zeta\frac{1}{\sqrt{\pi}}\int_{-\infty}^{\infty}\frac{e^{-u^2}}{u-\zeta}\mathrm{d}u, \\
&= 1 + \zeta Z(\zeta).
\end{aligned} \tag{B.3}$$

We can therefore rewrite (B.1) in terms of the dispersion function as,

$$1 = \left(\frac{\omega_p^2}{k^2 v_{th_e}^2}\right)\left(-2\left[1+\zeta Z(\zeta)\right]\right), \tag{B.4}$$

which is exactly the result we use in (1.22).

B.2 Detailed Analysis of the Series Approximation to the V-P Dispersion Relation

Truncating the expansion of (1.23) after the first three terms gives (B.5) in the original variables of Section 1.3.1 (Chen, 1984),

$$1 \approx \frac{\omega_p^2}{k^2}\left(\frac{k^2}{\omega^2} + 3\frac{k^4}{\omega^4}\frac{k_B T_e}{m_e} - 2i\pi^{1/2}\frac{\omega}{k}\left(\frac{m_e}{2k_B T_e}\right)^{3/2} e^{-\omega^2 m_e/(2k^2 k_B T_e)}\right). \tag{B.5}$$

Considering the real part of (B.5) while temporarily neglecting the small imaginary part approximately yields the well known electron dispersion relation (Chen, 1984),

$$\omega^2 \approx \omega_p^2 + \frac{3}{2}k^2\frac{\omega_p^2}{\omega^2}v_{th_e}^2, \tag{B.6}$$

where the response frequency is determined both by the plasma frequency ω_p itself and by a thermal correction of the form $(3/2)(\omega_p^2/\omega^2)k^2 v_{th_e}^2$. For long waves, it is acceptable to neglect the thermal correction on the right hand side of (B.6) and set $\omega^2 = \omega_p^2$ in the second term of (B.6) to form the common explicit approximation for the response frequency $\mathrm{Re}(\omega)$ (Chen, 1984),

$$\mathrm{Re}(\omega) \approx \sqrt{\omega_p^2 + \frac{3}{2}k^2 v_{th_e}^2}. \tag{B.7}$$

Moreover, it is allowable to neglect this thermal correction in evaluating the coefficient of the imaginary part of ω, which has already been assumed to be quite small, but not necessarily in evaluating the exponent (Chen, 1984). Thus, returning to (B.5) with this approximation in hand, we can write,

$$1 \approx \frac{\omega_p^2}{\omega^2} - 2i\pi^{1/2}\left(\frac{\omega_p}{kv_{th_e}}\right)^3 e^{-\omega_p^2/k^2 v_{th_e}^2} e^{-3/2}, \tag{B.8}$$

which leads directly to,

$$\omega_p^2 \approx \omega^2\left(1 + 2i\pi^{1/2}\left(\frac{\omega_p}{kv_{th_e}}\right)^3 e^{-\omega_p^2/k^2 v_{th_e}^2} e^{-3/2}\right). \tag{B.9}$$

We now take the square root of the entire equation using the approximate Taylor expansion $\sqrt{1+x} \approx 1 + x/2$, divide by the coefficient on ω, and use the approximate Taylor expansion $1/(1+x) \approx 1 - x$ to obtain an estimate for ω as in Chen (1984),

$$\omega \approx \omega_p\left(1 - i\pi^{1/2}\left(\frac{\omega_p}{kv_{th_e}}\right)^3 e^{-\omega_p^2/k^2 v_{th_e}^2} e^{-3/2}\right). \tag{B.10}$$

Finally, the imaginary part of ω is (Chen, 1984),

$$\mathrm{Im}(\omega) \approx -\pi^{1/2}\omega_p\left(\frac{\omega_p}{kv_{th_e}}\right)^3 e^{-\omega_p^2/k^2 v_{th_e}^2} e^{-3/2}. \tag{B.11}$$

Equations (B.7) and (B.11) give the exact results used in (1.24a) and (1.24b).

B.3 A Numerical Solution Method for the V-P Plasma Dispersion Relation

To begin, we discuss a method by which the V-P plasma dispersion relation (1.22) can be solved numerically to recover an accurate estimate of the ω value predicted by our theoretical analysis. This method, which we utilize several times in this study, is originally due to Wiedeman (1994), and is summarized here for the benefit of the reader. Under the normalization of Section 4.1, the V-P dispersion relation becomes,

$$1 + \frac{2}{k^2}[1 + \zeta Z(\zeta)] = 0, \tag{B.12}$$

with $\zeta = \omega/k$. We solve this expression numerically using highly accurate approximations of the analytic dispersion function (1.21). The basis of these approximations comes from assuming an expansion of the form (Wiedeman, 1994),

$$[W(x)]^{-1} e^{-x^2} = \sum_{n=-\infty}^{\infty} a_n \alpha_n(x), \ x \in \mathbb{R}, \tag{B.13}$$

where $\{\alpha_n(x)\}$ represents an orthogonal basis for the function space $L_2(\mathbb{R}; W(x))$ with weight function $W(x)$. In such a framework, we can write the integrand of the plasma dispersion function as (Wiedeman, 1994),

$$\frac{e^{-x^2}}{x - \zeta} = \sum_{n=-\infty}^{\infty} a_n \left[W(x) \frac{\alpha_n(x)}{x - \zeta} \right], \tag{B.14}$$

and integrate term by term to obtain,

$$Z(\zeta) = \sum_{n=-\infty}^{\infty} a_n \psi_n(\zeta), \tag{B.15}$$

where,

$$\psi_n(\zeta) = \pi^{-\frac{1}{2}} \int_{-\infty}^{\infty} W(x) \frac{\alpha_n(x)}{x - \zeta} \mathrm{d}x. \tag{B.16}$$

Extant literature proposes and evaluates a number of possible definitions for $\{\alpha_n(x)\}$, and reports several that give quite accurate results. In particular, the work of Wiedeman (1994) suggests the use of $\alpha_n(x)$ of the form,

$$\alpha_n(x) = \left(\frac{L + ix}{L - ix} \right)^n, \tag{B.17}$$

where L is a real, positive parameter chosen to maximize the accuracy of the approximation and $W(x) = 1/(L^2 + x^2)$. The *faddeeva.m* MATLAB function can be

used to evaluate $Z(\zeta)$ with such an approximation, which allows us to numerically solve the dispersion relation of (B.12). The author is indebted to Kesh Ikuma for the *faddeeva.m* function, which is maintained in the public domain on MATLAB Central.[1]

B.4 Relative Error in V-P Dispersion Results

In this section we present Fig. B.1, which illustrates the deviation between the growth rate and frequency results extracted from the Fourier-Hermite model of the V-P system and those calculated by numerically solving the exact V-P dispersion relation. Errors are normalized by the values obtained from the exact dispersion relation.

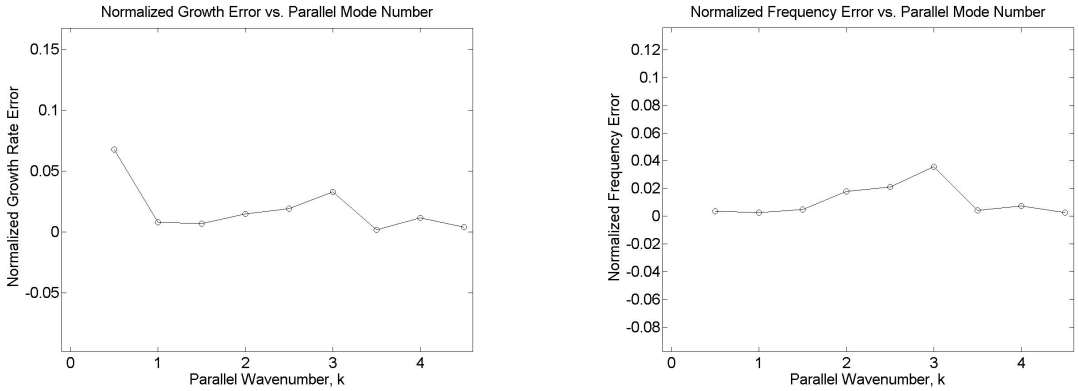

(a) Normalized Growth Rate Error (b) Normalized Frequency Error

Figure B.1: Normalized linear response error in the hypercollisional V-P system.

B.5 Assessment of the Series Approximation to the V-P Dispersion Relation

We can also investigate how well the weak damping approximation of (1.24a) and (1.24b) performs in the low wavenumber case wherein the damping is in fact relatively weak. Under our plasma wave normalizations, we can express the frequency $\mathrm{Re}(\omega)$ and the growth rate γ as,

$$\mathrm{Re}(\omega) = \sqrt{1 + \frac{3}{2}k^2}, \tag{B.18}$$

$$\gamma = -\pi^{\frac{1}{2}} \left(\frac{1}{k}\right)^3 e^{-1/k^2} e^{-3/2}. \tag{B.19}$$

[1]The *faddeeva.m* function can be found at http://www.mathworks.com/matlabcentral/fileexchange/22207-faddeeva-function-fft-based/content/faddeeva.m.

As a first computationally simple approximation, we assess the agreement between the weak damping approximation of (B.18) and (B.19) and our Fourier-Hermite numerics in the low wavenumber case where this approximation is valid. Figure B.2 presents both our numerical results and the weak damping approximation to the dispersion relation. We observe that the approximation displays marginal agreement at best with the numerics at low wavenumbers and begins to significantly break down as $k \to 1$ and damping becomes non-negligible. This lack of agreement for $k \sim 1$ motivates our attempts to solve the exact dispersion relation numerically, a procedure which gives good agreement between our V-P model and results derived from analytic linear theory for all k.

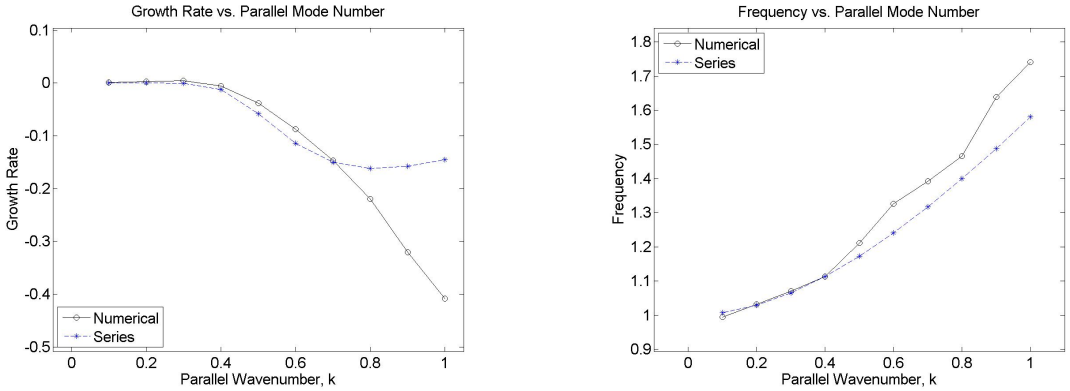

(a) Growth Rate (b) Frequency

Figure B.2: Hypercollisional V-P linear response and low k series approximation.

B.6 Detailed Analysis of the Series Approximation to the V-Q Dispersion Relation

Beginning from (5.3), we write out $\partial F_0/\partial v$ to obtain,

$$1 = \eta \frac{v_{th_i}^2}{2} \frac{1}{v_{th_i}^3} \frac{1}{\sqrt{\pi}} \int_{-\infty}^{\infty} \frac{-2ve^{-v^2/v_{th_i}^2}}{v - \frac{\omega}{k}} \mathrm{d}v. \tag{B.20}$$

Changing variables to $u \equiv v/v_{th_i}$ and $\zeta \equiv \omega/kv_{th_i}$ gives,

$$1 = \frac{\eta}{2} \left(-2 \left[\frac{1}{\sqrt{\pi}} \int_{-\infty}^{\infty} \frac{ue^{-u^2}}{u - \zeta} \mathrm{d}u \right] \right). \tag{B.21}$$

Using the identity (B.3) then allows us to rewrite the dispersion relation as,

$$1 + \eta \left[1 + \zeta Z(\zeta) \right] = 0, \tag{B.22}$$

which is exactly the result we use in (5.4). Now, using the series approximation to the dispersion function (1.23) to leading order in both real and imaginary parts gives,

$$1 \approx \eta \left[\frac{1}{2\zeta^2} - i\pi^{1/2} \zeta e^{-\zeta^2} \right]. \tag{B.23}$$

Note that we have assumed $|\zeta| \gg 1$ and $|\mathrm{Im}(\zeta)| < |\mathrm{Re}(\zeta)|^{-1}$ to use this series expansion. Neglecting the small imaginary part of (B.23) gives the approximate result,

$$1 \approx \frac{\eta}{2\zeta^2}, \tag{B.24}$$

which directly implies,

$$\mathrm{Re}(\omega) \approx \sqrt{\frac{\eta}{2}} k v_{th_i}, \tag{B.25}$$

as in (5.5). We can now perform the same analysis as in the V-P case by inserting (B.25) into (B.23) and estimating $\mathrm{Im}(\omega)$. Executing this procedure using our definition of ζ while neglecting the small $\mathrm{Im}(\omega)$ term in the imaginary part of the dispersion function expansion gives,

$$1 \approx \frac{\eta}{2} \left[\frac{k^2 v_{th_i}^2}{\omega^2} - 2i\pi^{1/2} \sqrt{\frac{\eta}{2}} e^{-\eta/2} \right]. \tag{B.26}$$

We can rewrite (B.26) as,

$$\omega^2 \left(1 + \frac{\eta^{3/2}}{\sqrt{2}} i\pi^{1/2} e^{-\eta/2} \right) \approx \frac{\eta}{2} k^2 v_{th_i}^2. \tag{B.27}$$

Using the Taylor series approximations $\sqrt{1+x} \approx 1 + x/2$ and $1/(1+x) \approx 1 - x$ as in Appendix (B.2) yields,

$$\omega \approx \sqrt{\frac{\eta}{2}} k v_{th_i} \left(1 - \frac{\eta^{3/2}}{2\sqrt{2}} i\pi^{1/2} e^{-\eta/2} \right). \tag{B.28}$$

Thus, we obtain the second result of (5.5) by evaluating the imaginary part of (B.28) as below,

$$\mathrm{Im}(\omega) \approx -\frac{\eta^2}{4} i\pi^{1/2} k v_{th_i} e^{-\eta/2}, \tag{B.29}$$

where we note that the negative sign in (B.29) unambiguously indicates that the ion acoustic waves in this system are Landau damped. We now return to our assumptions on ζ. First, $1 \ll |\zeta| = |\eta k v_{th_i}/2|$ implies that $1 \ll \eta$. Using this result, we see that the Landau damping rate of (B.29) is exponentially small, thereby validating our second assumption that $|\mathrm{Im}(\zeta)| < |\mathrm{Re}(\zeta)|^{-1}$. This also confirms our original assumption that we are dealing with the weak damping case. Thus, in alignment with known theory, the approximate expression (B.29) implies that Landau damping of the ion acoustic wave is indeed small in the case of cold ions where $T_i \ll T_e$ and therefore $1 \ll \eta$.

B.7 Relative Error in V-Q Dispersion Results

In this section we present Fig. B.3, which illustrates the deviation between the growth rate and frequency results extracted from the Fourier-Hermite model of the V-Q system and those calculated by numerically solving the exact V-Q dispersion relation. Errors are normalized by the values obtained from the exact dispersion relation.

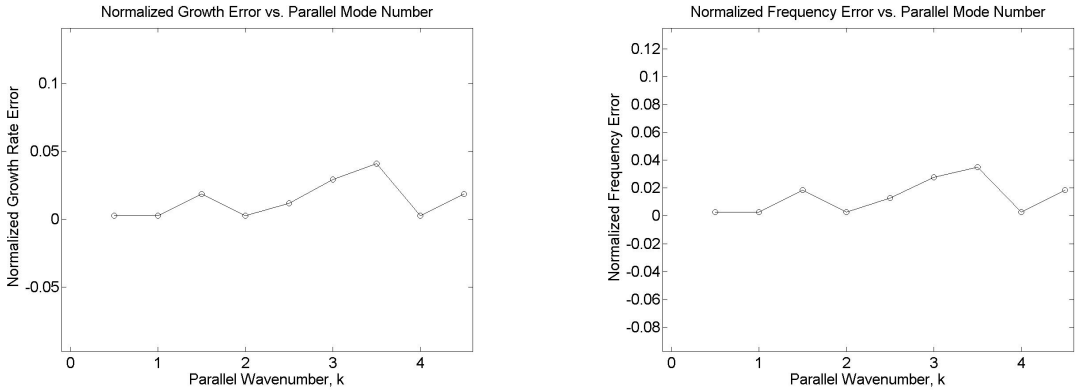

(a) Normalized Growth Rate Error

(b) Normalized Frequency Error

Figure B.3: Normalized linear response error in the hypercollisional V-Q system.

Appendix C

Derivation of the Gyrokinetic Equation

As mentioned in Section 2.4, we present a detailed derivation of the gyrokinetic modeling equations below by looking at subsequently higher orders of the expanded VFP equation with respect to ϵ. The derivation below was written by the author in order to concisely, but closely, follow the combined work of Howes et al. (2006) and Abel et al. (2012) in a manner accessible to a reader with little background in gyrokinetics or plasma physics. It is included for the benefit of the reader as opposed to representing original work by the author.

To derive the gyrokinetic equation for general charged particles of species s, we first write the VFP equation in terms of the gyrokinetic framework. Specifically, we can substitute (2.28c) into (1.6) to obtain the following for a multi-species plasma,

$$\frac{\partial f_s}{\partial t} + \mathbf{v} \cdot \nabla f_s + \frac{q_s}{m_s c} \left(-c\nabla\Phi - \frac{\partial \mathbf{A}}{\partial t} + \mathbf{v} \times \mathbf{B} \right) \cdot \nabla_{\mathbf{v}} \; f_s = C[f_s, f_s], \tag{C.1}$$

where the $C[f_s, f_s]$ shorthand can describe collisions both between like particles and different particles (Howes et al., 2006). Now, invoking the ordering of (2.10) – (2.16) allows us to separate (C.1) into three different equations for each of the three orders of the asymptotic parameter ϵ relative to the leading order quantity $\Omega_s F_0$ (Abel et al., 2012). While the explicit ordering of each term in the expansion is omitted here for brevity, a full explanation can be found in Appendix A of Howes et al. (2006).

C.1 Zeroth Order Terms of the VFP Expansion

As there is only one term in (C.1) that is of $O(\epsilon^0 = 1)$ with respect to $\Omega_s F_0$, we recover the simple equation,

$$(\mathbf{v} \times \mathbf{B}_0) \cdot \frac{\partial F_0}{\partial \mathbf{v}} = 0, \tag{C.2}$$

at zeroth order. Physically, (C.2) implies that the change in the background distribution function in the direction of the particle gyrations about the background magnetic field is zero. In gyrokinetic coordinates where $\mathbf{v}$ is defined by the coordinates $(v_\parallel, v_\perp, \theta)$ with $|\mathbf{v}| \equiv \sqrt{v_\perp^2 + v_\parallel^2}$, we can reduce (C.2) to,

$$\frac{\partial F_0}{\partial \theta} = 0, \tag{C.3}$$

which implies that the background equilibrium distribution function F_0 depends only on $v_\parallel, v_\perp$, and t with no dependence on the gyrophase angle θ (Howes et al., 2006).

C.2 First Order Terms of the VFP Expansion

Consideration of the $O(\epsilon)$ terms in (C.1) gives,

$$\mathbf{v}_\perp \cdot \nabla \delta f_{1s} + \frac{q_s}{m_s c} \left(-c\nabla\Phi + \mathbf{v} \times \delta\mathbf{B}\right) \cdot \frac{\partial F_0}{\partial \mathbf{v}} - \Omega_s \frac{\partial \delta f_{1s}}{\partial \theta} = C[F_0, F_0]. \tag{C.4}$$

At this point, we follow the work of Howes et al. (2006) by substituting (C.3) into (C.4), multiplying the resultant form of (C.4) by the quantity $1+\ln F_0$, and integrating over all spatial and velocity coordinates. Under the assumption that all perturbations average to zero in physical space, we recover the integral equation (Howes et al., 2006),

$$\int \mathrm{d}^3\mathbf{r} \int \mathrm{d}^3\mathbf{v} (\ln F_0) C[F_0, F_0] = 0. \tag{C.5}$$

This result provides a very useful piece of information because it has been shown that F_0 must be a Maxwellian distribution in order to satisfy (C.5) (Howes et al., 2006). While this analysis is not a focus of the current study and will thus not be replicated here, a full discussion of the relevant mathematics and assumptions may be found in Abel et al. (2012).

Now, rewriting (C.4) with $C[F_0, F_0] = 0$ and F_0 explicitly defined as the Maxwellian distribution gives,

$$\mathbf{v}_\perp \cdot \nabla \delta f_{1s} - \Omega_s \frac{\partial \delta f_{1s}}{\partial \theta} = -\mathbf{v} \cdot \nabla \left(\frac{q_s \Phi}{k_B T_s} \right) F_0, \tag{C.6}$$

which represents an inhomogeneous first order hyperbolic differential equation for δf_{1s}. The analysis of Howes et al. (2006) shows that a particular solution to this problem is $\delta f_{ps} = -\left(q_s\Phi/k_BT_s\right) F_0 + O(\epsilon^2 F_0)$, meaning that we can write δf_{1s} as $\delta f_{1s} = -(q_s\Phi/k_BT_s)F_0 + h_s$, where h_s represents the solution to the homogeneous problem,

$$\mathbf{v}_\perp \cdot \nabla h_s - \Omega_s \left(\frac{\partial h_s}{\partial \theta} \right)_{\mathbf{r}} = -\Omega_s \left(\frac{\partial h_s}{\partial \theta} \right)_{\mathbf{R}} = 0. \tag{C.7}$$

We can thus write the complete solution of the distribution function as the following under the realization that $1 - q_s\Phi/k_BT_s = \exp\left(-q_s\Phi/k_BT_s\right) + O(\epsilon^2)$ and that terms of $O(\epsilon^2)$ can be incorporated into δf_2 (Howes et al., 2006),

$$\begin{aligned} f_s &= F_0 + \delta f_{1s} + \delta f_{2s} + ..., \\ &= F_0(|\mathbf{v}|, \epsilon^2 t)\left(1 - \frac{q_s\Phi(\mathbf{r},t)}{k_BT_s}\right) + h_s(\mathbf{R}, |\mathbf{v}|, v_\perp, t) + \delta f_{2s}..., \\ &= F_0(|\mathbf{v}|, \epsilon^2 t)e^{-q_s\Phi(\mathbf{r},t)/k_BT_s} + h_s(\mathbf{R}, |\mathbf{v}|, v_\perp, t) + \delta f_{2s}... \end{aligned} \tag{C.8}$$

The first order equation, then, yields two important results. Firstly, it requires that the background distribution function of the gyrokinetic model be Maxwellian. Secondly, it implies that the most useful results from such a model will come from the second order terms of the asymptotic expansion wherein the distribution function perturbation h_s can be explicitly solved.

C.3 Second Order Terms of the VFP Expansion

The terms in (C.1) that are of $O(\epsilon^2)$ ultimately give rise to the expression canonically known as the "gyrokinetic equation," which forms the basis of this model by giving the evolution of the perturbation h_s to the background distribution function F_0. To begin, we substitute the form of f_s from (C.8) into the second order terms of (C.1) while changing variables to the velocity space coordinates $(v_\parallel, v_\perp, \theta)$ and the spatial coordinates defined around the guiding center in Section 2.3. The result of these operations yields the following restatement of the second order VFP equation (Howes et al., 2006),[1]

$$\begin{aligned} &\frac{\partial h_s}{\partial t} + \frac{\mathrm{d}\mathbf{R}}{\mathrm{d}t}\cdot\frac{\partial h_s}{\partial \mathbf{R}} + \frac{q_s}{m_s c}\left(-c\nabla_\perp\Phi + \mathbf{v}\times\delta\mathbf{B}\right)\cdot\left(\frac{\mathbf{v}}{v}\frac{\partial h_s}{\partial v} + \frac{\mathbf{v}_\perp}{v_\perp}\frac{\partial h_s}{\partial v_\perp}\right) - \\ &C[h_s, F_0] - C[F_0, h_s] = \Omega_s\left(\frac{\partial \delta f_{2s}}{\partial\theta}\right)_{\mathbf{R}} + \frac{q_s}{k_BT_s}\left(\frac{\partial\Phi}{\partial t} - \frac{\mathbf{v}}{c}\cdot\frac{\partial\mathbf{A}}{\partial t}\right)F_0, \end{aligned} \tag{C.9}$$

where,

$$\frac{\mathrm{d}\mathbf{R}}{\mathrm{d}t} = v_\parallel\hat{\mathbf{z}} + \frac{1}{B_0}\left(-c\nabla\Phi - \frac{\partial\mathbf{A}}{\partial t} + \mathbf{v}\times\delta\mathbf{B}\right)\times\hat{\mathbf{z}}. \tag{C.10}$$

We now simplify (C.9) by gyroaveraging the entire equation over θ with $\mathbf{R}$ held constant, which yields several important results. Firstly, it becomes clear that δf_{2s} must be periodic in θ due to the fact that it describes the second order perturbation to the background distribution function. This second order perturbation is governed

[1] In the interest of brevity, the mechanics of these transformations are left to the reader.

only by the gyromotion, and when averaged over θ both δf_{2s} and its derivative with respect to θ should be zero. We can also use the powerful identity that for any arbitrary function a (Howes et al., 2006),

$$\begin{aligned}
\langle \mathbf{v}_\perp \cdot \nabla a \rangle_{\mathbf{R}} &= -\Omega_s \left\langle (\mathbf{v} \times \hat{\mathbf{z}}) \cdot \left(\frac{\partial}{\partial \mathbf{v}} \frac{\mathbf{v} \times \hat{\mathbf{z}}}{\Omega_s} \right) \cdot \nabla a \right\rangle_{\mathbf{R}}, \\
&= \Omega_s \left\langle (\mathbf{v} \times \hat{\mathbf{z}}) \cdot \left(\frac{\partial \mathbf{r}}{\partial \mathbf{v}} \right)_{\mathbf{R}} \cdot \nabla a \right\rangle_{\mathbf{R}}, \\
&= \Omega_s \left\langle (\mathbf{v} \times \hat{\mathbf{z}}) \cdot \left(\frac{\partial a}{\partial \mathbf{v}} \right)_{\mathbf{R}} \right\rangle_{\mathbf{R}}, \\
&= -\Omega_s \left\langle \left(\frac{\partial a}{\partial \theta} \right)_{\mathbf{R}} \right\rangle_{\mathbf{R}}, \\
&= 0, \qquad \text{(C.11)}
\end{aligned}$$

to significantly reduce the complexity of the equation. Specifically, this identity requires both that,

$$\langle \mathbf{v} \cdot \nabla_\perp \Phi \rangle_{\mathbf{R}} = 0, \qquad \text{(C.12)}$$

and also that, in combination with (2.28b) (Howes et al., 2006),

$$\langle \mathbf{v}_\perp \cdot (\mathbf{v} \times \delta \mathbf{B}) \rangle_{\mathbf{R}} = v_\parallel \langle \mathbf{v}_\perp \cdot (\hat{\mathbf{z}} \times \delta \mathbf{B}) \rangle_{\mathbf{R}} = v_\parallel \langle \mathbf{v}_\perp \cdot \nabla_\perp A_\parallel \rangle_{\mathbf{R}} = 0. \qquad \text{(C.13)}$$

Effectively, then, this gyroaveraging causes the complicated third term on the left hand side of (C.9) to vanish as a direct consequence of (C.12) and (C.13). In light of these cancellations, then, the gyroaveraged form of (C.9) can be rewritten as,

$$\frac{\partial h_s}{\partial t} + \left\langle \frac{\mathrm{d}\mathbf{R}}{\mathrm{d}t} \right\rangle_{\mathbf{R}} \cdot \frac{\partial h_s}{\partial \mathbf{R}} - \left(\frac{\partial h_s}{\partial t} \right)_{coll} = \frac{q_s}{k_B T_s} \frac{\partial \langle \chi \rangle_{\mathbf{R}}}{\partial t} F_0, \qquad \text{(C.14)}$$

where we have defined the gyrokinetic potential (Howes et al., 2006),

$$\chi = \Phi - \mathbf{v} \cdot \frac{\mathbf{A}}{c}, \qquad \text{(C.15)}$$

and the gyrokinetic collision operator,

$$\left(\frac{\partial h_s}{\partial t} \right)_{coll} = \langle C[h_s, F_0] + C[F_0, h_s] \rangle_{\mathbf{R}}. \qquad \text{(C.16)}$$

As a final step, we disambiguate the expression $\langle \mathrm{d}\mathbf{R}/\mathrm{d}t \rangle_{\mathbf{R}}$ by working through the ring average of (C.10) while substituting in (2.28b) for the magnetic field and using

the identity $\langle \mathbf{v}_\perp \delta B_\parallel \rangle_{\mathbf{R}} = -\langle \nabla_\perp (\mathbf{v}_\perp \cdot \mathbf{A}_\perp) \rangle_{\mathbf{R}}$ (Howes et al., 2006),

$$\begin{aligned}
\left\langle \frac{\mathrm{d}\mathbf{R}}{\mathrm{d}t} \right\rangle_{\mathbf{R}} &= v_\parallel \hat{\mathbf{z}} + \frac{1}{B_0} \left(-c \langle \nabla_\perp \Phi \rangle_{\mathbf{R}} \times \hat{\mathbf{z}} + v_\parallel \langle \nabla_\perp A_\parallel \rangle_{\mathbf{R}} \times \hat{\mathbf{z}} - \langle \mathbf{v}_\perp \delta B_\parallel \rangle_{\mathbf{R}} \right), \\
&= v_\parallel \hat{\mathbf{z}} + \frac{1}{B_0} \left(-c \langle \nabla_\perp \Phi \rangle_{\mathbf{R}} \times \hat{\mathbf{z}} + v_\parallel \langle \nabla_\perp A_\parallel \rangle_{\mathbf{R}} \times \hat{\mathbf{z}} + \langle \nabla_\perp (\mathbf{v}_\perp \cdot \mathbf{A}_\perp) \rangle_{\mathbf{R}} \right), \\
&= v_\parallel \hat{\mathbf{z}} + \frac{c}{B_0} \left\langle \nabla_\perp \left(-\Phi + \frac{\mathbf{v} \cdot \mathbf{A}}{c} \right) \right\rangle \times \hat{\mathbf{z}}, \\
&= v_\parallel \hat{\mathbf{z}} - \frac{c}{B_0} \frac{\partial \langle \chi \rangle_{\mathbf{R}}}{\partial \mathbf{R}} \times \hat{\mathbf{z}}. \qquad \text{(C.17)}
\end{aligned}$$

Substituting the result of (C.17) into the ring-averaged second order VFP equation of (C.14), then, gives an expression generally known as the gyrokinetic equation,

$$\frac{\partial h_s}{\partial t} + v_\parallel \hat{\mathbf{z}} \cdot \frac{\partial h_s}{\partial \mathbf{R}} + \frac{c}{B_0} \{ \langle \chi \rangle_{\mathbf{R}}, h_s \} - \left(\frac{\partial h_s}{\partial t} \right)_{coll} = \frac{q_s}{k_B T_s} \frac{\partial \langle \chi \rangle_{\mathbf{R}}}{\partial t} F_0, \qquad \text{(C.18)}$$

in which nonlinear effects are captured via the Poisson bracket (Howes et al., 2006),

$$\{ \langle \chi \rangle_{\mathbf{R}}, h_s \} = \hat{\mathbf{z}} \cdot \left(\frac{\partial \langle \chi \rangle_{\mathbf{R}}}{\partial \mathbf{R}} \times \frac{\partial h_s}{\partial \mathbf{R}} \right). \qquad \text{(C.19)}$$

This completes our presentation of the derivation of the gyrokinetic modeling equations discussed in Section 2.4.

Appendix D

Additional Unforced V-Q Derivations and Results

D.1 Detailed Calculation of Φ from (3.18)

$$\begin{aligned}
\Phi &= \int_{-\infty}^{\infty} \delta f_{1i} \mathrm{d}v, \\
&= \int_{-\infty}^{\infty} \sum_{\substack{n=0, \\ j=-\infty}}^{\infty} a_{n,j}(t)\phi_n(v)e^{ik_j z}\mathrm{d}v, \\
&= \sum_{\substack{n=0, \\ j=-\infty}}^{\infty} a_{n,j}(t)e^{ik_j z} \int_{-\infty}^{\infty} \phi_n(v)\mathrm{d}v, \\
&= \sum_{\substack{n=0, \\ j=-\infty}}^{\infty} a_{n,j}(t)e^{ik_j z} \int_{-\infty}^{\infty} \phi_n(v)\,(1)\,\mathrm{d}v, \\
&= \sum_{\substack{n=0, \\ j=-\infty}}^{\infty} a_{n,j}(t)e^{ik_j z} \int_{-\infty}^{\infty} \phi_n(v)\left(\phi^0(v)\right)\mathrm{d}v, \\
&= \sum_{\substack{n=0, \\ j=-\infty}}^{\infty} a_{n,j}(t)e^{ik_j z}\delta_{0,n}, \\
&= \sum_{j=-\infty}^{\infty} a_{0,j}(t)e^{ik_j z}. \qquad \text{(D.1)}
\end{aligned}$$

D.2 Detailed Derivation of Equation (3.25)

We begin by projecting (3.24) onto the g^{th} Fourier mode as below,

$$\int_{-L_g}^{L_g} \sum_{\substack{n=0 \\ j=-\infty \\ h\neq 0}}^{\infty} \left\{ \dot{a}_{n,j}\phi_n e^{ik_j z} + ik_j a_{n,j}\left(\sqrt{\frac{n+1}{2}}\phi_{n+1} + \sqrt{\frac{n}{2}}\phi_{n-1}\right) e^{ik_j z} - \right.$$

$$\left. \frac{1}{2} ik_h a_{n,j} a_{0,h} \left[-\sqrt{2n+2}\phi_{n+1}\right] e^{i(k_j+k_h)z} \right\} e^{-ik_g z}\mathrm{d}z = \frac{1}{2L_g}\int_{-L_g}^{L_g} vEF_0 e^{-ik_g z}\mathrm{d}z,$$

$$\int_{-L_g}^{L_g} \sum_{\substack{n=0 \\ j=-\infty \\ h\neq 0}}^{\infty} \left\{ \dot{a}_{n,j}\phi_n e^{i(k_j-k_g)z} + ik_j a_{n,j}\left(\sqrt{\frac{n+1}{2}}\phi_{n+1} + \sqrt{\frac{n}{2}}\phi_{n-1}\right) e^{i(k_j-k_g)z} - \right.$$

$$\left. \frac{1}{2} ik_h a_{n,j} a_{0,h} \left[-\sqrt{2n+2}\phi_{n+1}\right] e^{i(k_j+k_h-k_g)z} \right\} \mathrm{d}z = \frac{1}{2L_g}\int_{-L_g}^{L_g} vEF_0 e^{-ik_g z}\mathrm{d}z,$$

$$\sum_{\substack{n=0 \\ j\neq g}}^{\infty} \left\{ \dot{a}_{n,g}\phi_n + ik_g a_{n,g}\left(\sqrt{\frac{n+1}{2}}\phi_{n+1} + \sqrt{\frac{n}{2}}\phi_{n-1}\right) - \right.$$

$$\left. \frac{1}{2} ik_{g-j} a_{n,j} a_{0,g-j} \left[-\sqrt{2n+2}\phi_{n+1}\right] \right\} = \frac{1}{2L_g}\int_{-L_g}^{L_g} vEF_0 e^{-ik_g z}\mathrm{d}z. \tag{D.2}$$

Note that $L_g \equiv L_N/2$ represents the half length of the periodic box on which each g^{th} Fourier mode is defined, and that (D.2) will hold true as long as the grid of Fourier wavenumbers is evenly spaced, as $j + h = g$ implies that $k_j + k_h = k_g$ in such a case. Thus, projecting (D.2) onto a single Hermite mode ϕ^p in a similar manner gives,

$$\int_{-\infty}^{\infty} \sum_{\substack{n=0 \\ j\neq g}}^{\infty} \left\{ \dot{a}_{n,g}\phi_n + ik_g a_{n,g}\left(\sqrt{\frac{n+1}{2}}\phi_{n+1} \quad + \quad \sqrt{\frac{n}{2}}\phi_{n-1}\right) - \right.$$

$$\left. \frac{1}{2} ik_{g-j} a_{n,j} a_{0,g-j} \left[-\sqrt{2n+2}\phi_{n+1}\right] \right\} \phi^p \mathrm{d}v \quad = \quad \frac{1}{2L_g}\int_{-\infty}^{\infty}\int_{L_g}^{L_g} vEF_0 e^{-ik_g z}\phi^p \mathrm{d}z\mathrm{d}v,$$

$$\dot{a}_{p,g} + ik_g \left(a_{p-1,g}\sqrt{\frac{p}{2}} + a_{p+1,g}\sqrt{\frac{p+1}{2}} \right) \quad +$$

$$\frac{1}{2} i\sqrt{2p} \sum_{j\neq g} a_{p-1,j} a_{0,g-j} k_{g-j} \quad = \quad \frac{1}{2L_g}\int_{-\infty}^{\infty}\int_{-L_g}^{L_g} vEF_0 e^{-ik_g z}\phi^p \mathrm{d}z\mathrm{d}v. \tag{D.3}$$

Equation (D.3) gives the exact result used in (3.25).

D.3 Detailed Calculation of $L_{p,g}$ from (3.29)

$$
\begin{aligned}
L_{p,g} &= \frac{1}{2iL_g}\int_{-\infty}^{\infty}\int_{-L_g}^{L_g} vEF_0 e^{-ik_g z}\phi^p \mathrm{d}z\mathrm{d}v, \\
&= -\frac{1}{i}\int_{-\infty}^{\infty} vF_0\phi^p \sum_{j\neq 0} ik_j a_{0,j}\left(\frac{1}{2L_g}\int_{-L_g}^{L_g} e^{ik_j z}e^{-ik_g z}\mathrm{d}z\right)\mathrm{d}v, \\
&= -\int_{-\infty}^{\infty} v\phi_p \sum_{j\neq 0} k_j a_{0,j}\delta_{j,g}\mathrm{d}v, \\
&= -\bar{\delta}_{g,0}k_g a_{0,g}\int_{-\infty}^{\infty} v\phi_p\phi^0\mathrm{d}v = -\bar{\delta}_{g,0}k_g a_{0,g}\int_{-\infty}^{\infty}\left(\sqrt{\frac{p+1}{2}}\phi_{p+1}+\sqrt{\frac{p}{2}}\phi_{p-1}\right)\phi^0\mathrm{d}v, \\
&= -g\Delta k a_{0,g}\left(\sqrt{\frac{p+1}{2}}\delta_{p+1,0}+\sqrt{\frac{p}{2}}\delta_{p-1,0}\right)\bar{\delta}_{g,0}, \\
&= -g\Delta k a_{0,g}\left(\sqrt{\frac{p+1}{2}}\delta_{p,-1}+\sqrt{\frac{p}{2}}\delta_{p,1}\right)\bar{\delta}_{g,0}, \\
&= -g\Delta k a_{0,g}\sqrt{\frac{1}{2}}\delta_{p,1}\bar{\delta}_{g,0} = -\frac{1}{\sqrt{2}}g\Delta k a_{0,g}\delta_{p,1}\bar{\delta}_{g,0}. \qquad \text{(D.4)}
\end{aligned}
$$

D.4 Detailed Calculation of $C_{p,g}$ from (3.34)

$$
\begin{aligned}
C_{p,g} &= \frac{1}{2L_g}\int_{-\infty}^{\infty}\int_{-L_g}^{L_g} C[\delta f_{1i}]e^{-ik_g z}\phi^p\mathrm{d}z\mathrm{d}v, \\
&= \frac{1}{2L_g}\int_{-\infty}^{\infty}\int_{-L_g}^{L_g}\left(\sum_{\substack{n=0,\\ j=-\infty}}^{\infty}\nu a_{1,j}\phi_1 e^{ik_j z}+2\nu a_{2,j}\phi_2 e^{ik_j z}-\nu n a_{n,j}\phi_n e^{ik_j z}\right)e^{-ik_g z}\phi^p\mathrm{d}z\mathrm{d}v, \\
&= \nu\int_{-\infty}^{\infty}\phi^p\frac{1}{2L_g}\int_{-L_g}^{L_g}\left(\sum_{\substack{n=0,\\ j=-\infty}}^{\infty} a_{1,j}\phi_1+2a_{2,j}\phi_2-n a_{n,j}\phi_n\right)e^{i(k_j-k_g)z}\mathrm{d}z\mathrm{d}v, \\
&= \nu\int_{-\infty}^{\infty}\left(\sum_{n=0}^{\infty} a_{1,g}\phi_1+2a_{2,g}\phi_2-n a_{n,g}\phi_n\right)\phi^p\mathrm{d}v, \\
&= \nu\left(a_{1,g}\delta_{p,1}+2a_{2,g}\delta_{p,2}-p a_{p,g}\right). \qquad \text{(D.5)}
\end{aligned}
$$

D.5 Truncation of the Fourier-Hermite Spectrum for an Unforced Nonlinear V-Q Simulation

We now present plots detailing the time evolution of the Fourier-Hermite coefficients during our nonlinear V-Q simulations. We see from Figs. (D.1) and (D.2) that these coefficients are indeed exponentially small and never greater than $O(10^{-8})$ in the highest Hermite mode, which validates our truncation of the Hermite spectrum.

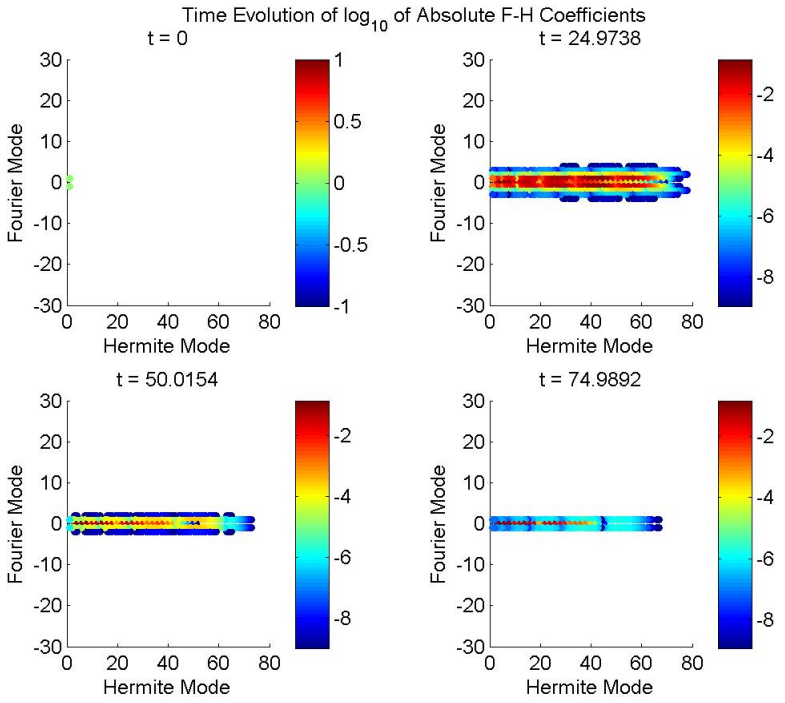

Figure D.1: Nonlinear time evolution of V-Q Fourier-Hermite coefficients.

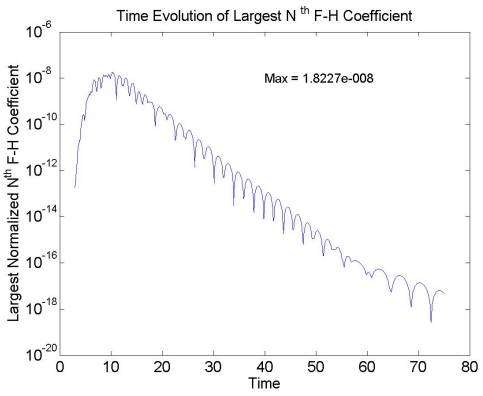

Figure D.2: Nonlinear time evolution of largest V-Q N^{th} modal coefficient.

Appendix E

Details of Computational Implementation

E.1 Input Parameters

The user is required to choose several important parameters for each run, including the normalized length of the spatial domain, the number of Fourier modes, the number of Hermite modes, and the final normalized time. The Fourier grid spacing is by default defined as $2\pi/L_N$, where L_N is the normalized length in terms of l_0, as required for Fourier orthonormality in the above model while the Hermite grid spacing is kept at unity for similar reasons. The numbers of Fourier and Hermite modes are generally kept to relatively small values of around 60 and 80, respectively, because current 5-D gyrokinetic codes only use resolutions of this size. Thus, by maintaining reasonable resolutions, we calculate results that will be very similar to those of the gyrokinetic codes we hope to approximate. While these parameters can generally be increased to an arbitrarily high value, 32-bit systems begin having trouble storing the very large $2^n n!$ values in the Hermite function normalization when transforming the spectral solution back to physical space at Hermite mode numbers of around 200. The user can also make several choices about the fundamental physics of the system, including which type of collisionality to use, the value at which to set the collision frequency ν, and whether to use a linear or nonlinear mathematical model. All input parameters listed here can be changed by the adjustment of a single variable value, be it a physical value or numerical function handle indicator.

E.2 Spectral Filters

As this model uses a spectral method to solve the V-Q system in time, it is important to understand the details of how these methods are implemented. In Hermite space, we have already discussed the truncation of the velocity space Hermite series at wavenumber N, which means that if energy should propagate as far as wavenumber N, it may begin to build up there or reflect back down into lower modes in a distinctly non-physical behavior known as recurrence. While collisionality will certainly address this issue by damping moderate to high Hermite wavenumbers, it is often more useful to implement a hypercollisional model to retain resolution gained by having nontrivial contributions from more moderate modes. In effect, the x^{hyp} function of (3.39) functions as a low-pass spectral filter in velocity space that severely damps the highest modes. The strength of this filter is controlled by the parameter n that defines the exponent of the x^{hyp} function of (3.39). The default value of this parameter is set to $n = 8$, which is quite similar to the value of $n = 6$ used in Parker and Dellar (2012), but can be adjusted to the user's modeling specifications. A similar truncation issue, moreover, can occur in Fourier space when energy moves into the K^{th} Fourier mode. This is particularly true in a fully nonlinear model, where energy from one mode can move into another mode as a result of the $\mathbf{y}$ term in (3.41). Linear models do not suffer from such issues, as the lack of nonlinearity causes energy to remain only in the Fourier modes that were activated at the initial simulation time. To address this issue in our nonlinear simulations, we have implemented a Fourier spectral filter that damps only the highest Fourier modes in the user-defined spectrum. The form of this filter is drawn from the extensive work of Hou and Li (2007) on computing nearly singular solutions using pseudo-spectral methods. This filter is defined by the function ρ and parameters α and m as below (Hou and Li, 2007),

$$\rho(k/N) = e^{-\alpha(|k|/N)^m}, \tag{E.1}$$

and is typically applied to the Fourier coefficients by direct multiplication at every timestep. In the work of Hou and Li (2007), α and m are both chosen as 36, which we utilize here by default. This value can, of course, be easily changed by the user at any time.

E.3 Temporal Solution Advancement

The main purpose of this computational model is to advance the $\mathbf{a}$ vector in time in order to calculate how the distribution function changes over time. The code accom-

plishes this task by using a classical fourth-order fixed-timestep explicit Runge-Kutta (RK4) scheme. This method was chosen not only due to its relatively high convergence order, but also because as an explicit method it greatly reduces computation time. A statement of the RK4 numerical method in the context of our matrix equations is,

$$\begin{aligned}
\mathbf{k_1} &= \dot{\mathbf{a}}(t_n, \mathbf{a}_n)\Delta t, \\
\mathbf{k_2} &= \dot{\mathbf{a}}\left(t_n + \frac{\Delta t}{2}, \mathbf{a}_n + \frac{\mathbf{k_1}}{2}\right)\Delta t, \\
\mathbf{k_3} &= \dot{\mathbf{a}}\left(t_n + \frac{\Delta t}{2}, \mathbf{a}_n + \frac{\mathbf{k_2}}{2}\right)\Delta t, \\
\mathbf{k_4} &= \dot{\mathbf{a}}(t_n + \Delta t, \mathbf{a}_n + \mathbf{k_3})\Delta t, \\
\mathbf{a}_{n+1} &= \mathbf{a}_n + \left(\frac{\mathbf{k_1}}{6} + \frac{\mathbf{k_2}}{3} + \frac{\mathbf{k_3}}{3} + \frac{\mathbf{k_4}}{6}\right) + O\left(\Delta t^5\right),
\end{aligned} \tag{E.2}$$

where t_n denotes the absolute time at step n and $n = 1, 2...N-1$ with initial condition $\mathbf{a}_0$ at $t = t_0$.

RK4 is also useful in that it exhibits favorable stability characteristics for an explicit method. The major challenge in implementing such a method is, of course, defining a timestep that maintains reasonable runtimes while ensuring numerical stability. This can be accomplished by performing a stability analysis on the linear portion of the system $\mathbf{a}^L$ where $\dot{\mathbf{a}}^L = \lambda \mathbf{a}^L$ for a general eigenvalue λ and determining the condition that must be satisfied to ensure that $|\mathbf{a}^L_{n+1}| \leq |\mathbf{a}^L_n| \ \forall \ n$. For the version of RK4 we use here, it has been shown that this condition can be defined in terms of the stability polynomial $R(z)$, where $\mathbf{a}^L$ obeys $\mathbf{a}^L_{n+1} = R(z)\mathbf{a}^L_n$ and $z = \lambda \Delta t$, as below (Butcher, 2000),

$$|R(z)| = \left|1 + z + \frac{z^2}{2} + \frac{z^3}{6} + \frac{z^4}{24}\right| \leq 1. \tag{E.3}$$

Note that in our system λ represents one of the eigenvalues of the effective linear portion of the system defined both by the matrix $\mathbf{M}$ and any linear contributions coming from other terms in the definition of $\dot{\mathbf{a}}$. Examining the region in $\lambda \Delta t$ defined by (E.3) leads to two potential stability conditions in our model. First, we note that the stability region intersects the imaginary axis at $z \approx \pm 2.82i$ and the real axis at $z \approx -2.79$. Realizing that the matrix $i\mathbf{M}$ defining the explicitly linear system has nearly imaginary eigenvalues λ_M, we conservatively require (Durran, 1991),

$$\Delta t \leq \frac{2.7}{\max\left(|\lambda_M|\right)}. \tag{E.4}$$

We must also consider the effect of the collisionality vector $\mathbf{C}$, which contributes to the linear portion of the system. Specifically, because $\mathbf{C}$ essentially adds elements to the zero-valued diagonal of $\mathbf{M}$ (e.g. Parker and Dellar, 2012), the maximum possible eigenvalue contribution from $\mathbf{C}$ will effectively be its largest "linear" coefficient on an element of $\mathbf{a}$. Given the structure of $\mathbf{C}$, we know that its largest linear contribution will always be that of the fastest decaying mode, which in this case is the Hermite mode with largest wavenumber. Thus, considering that all eigenvalue contributions of $\mathbf{C}$ are real-valued results of evaluating $x^c(p)$ functions such as (3.39), we can write a second conservative stability condition as (Durran, 1991),

$$\Delta t \leq \frac{2.7}{|x^c(N)|}, \tag{E.5}$$

where $x^c(p)$ is equal to 0 in the collisionless case, $x(p)$ in the collisional case, and $x^{hyp}(p)$ in the hypercollisional case. Our code therefore conservatively defines the RK4 timestep as,

$$\Delta t = 0.9 \times \min\left(\frac{2.7}{\max\left(|\lambda_M|\right)}, \frac{2.7}{|x^c(N)|}\right), \tag{E.6}$$

where we take the timestep to be 90% of the minimum timestep defined by our stability conditions. Such a definition allows us to be confident in the accuracy of our numerical results while significantly decreasing computation time. An important consequence of this algorithm is that the size of the Hermite spectrum is quite closely related to the timestep. Hypercollisionality therefore becomes extremely convenient computationally in that it requires many fewer Hermite modes than normal Dougherty collisionality to obtain equivalent effective modal resolution.

As a final step, we present pseudo-code defining the computational algorithm for efficiently advancing our Fourier-Hermite representation of the Vlasov-Poisson system in time as below,

1. Initialize variables, initial conditions, and boundary conditions.

   Define δf_{1s} at t_0 with initial values of all Fourier-Hermite coefficients in $\mathbf{a}$

   Periodic boundary conditions on Φ implicitly enforced by periodic ansatz

2. Perform time invariant calculations.

   Compute $\mathbf{M}$, eigenvalues of $\mathbf{M}$, and $x^c(N)$.

   Define timestep Δt.

3. for $n = 0, 1, 2...$

   Compute $\mathbf{L}(t_n)$, $\mathbf{y}(t_n)$, and $\mathbf{C}(t_n)$.

   Compute $\dot{\mathbf{a}}(t_n) = i\left(\mathbf{M}\mathbf{a}(t_n) + \mathbf{y}(t_n) + \mathbf{L}(t_n)\right) + \mathbf{C}(t_n)$.

   Compute $\mathbf{a}(t_{n+1})$ from $\mathbf{a}(t_n)$ and $\dot{\mathbf{a}}(t_n)$ using RK4.

   $t = t_{n+1} = t_n + \Delta t$

4. If $t < T$, go to step 3; else, end.

E.4 Outputs

As far as outputs are concerned, the major result of this code is the evolved vector $\mathbf{a}$, the values of which are saved at a multitude of different time points. This allows the user to not only visualize the evolution of the distribution function in both Fourier and Hermite space over time, but also to directly calculate the electric field, electric potential, and Fourier modal decompositions of each of these important quantities over time. In this way, our results allow for the user to make useful conclusions about the evolution of the distribution function in time as well as allowing for important phenomena such as Landau damping to be visualized in an effective manner. The evolution of the distribution function in both Fourier and Hermite space is critical to our understanding of fine scale development within fusion plasmas and ultimately enables our assessment of the relative importance of various dissipation mechanisms in these plasmas.

E.5 Potential Improvements

A number of improvements could be made to the code as currently constituted. Firstly, MATLAB is not the optimal language for constructing a code such as this if one requires very high modal resolution. Transferring this code to Fortran or C would likely represent a good start towards both speeding up the code and avoiding inbuilt limits such as maximum variable size that are intrinsic to MATLAB run on conventional computers. It would certainly be desirable to perform these operations for very high modal resolutions to see what effect this has on the results obtained. As mentioned earlier, however, it makes sense to keep our resolution relatively low in this study because 5-D gyrokinetic codes will not have very large velocity space resolution, as the large phase space dimensionality makes additional resolution in any one dimension particularly expensive. A major weakness of the current code is that

it does not use a Fast Fourier Transform (FFT) routine to compute the nonlinearity. Rather, a sum of modal products is calculated explicitly. Given that we use relatively low resolution, it is likely that such an FFT routine would not yield enormous improvements in terms of computational performance because our system is likely not far above the breakeven size wherein the additional expense of the FFT becomes mitigated by the improved efficiency of calculating the nonlinear term through direct multiplication in physical space. If the reader should desire to use this code as the basis of a high resolution study, it is recommended that such an FFT routine be implemented. Despite these potential improvements, however, the code as currently constituted performs quite well in accomplishing the types of accurate low resolution computations required for this study.

Appendix F

Derivation of Benchmarking Equations for the V-P System

The current section contains a detailed derivation of a model for the the classically electrostatic V-P system that is analogous to that in Section 3.1 for the quasineutral V-Q case. These modeling equations for the V-P system are used to benchmark our numerical code against a comprehensive set of existing results from the work of Heath et al. (2012). Because collisionality is unaffected by the electrostatic coupling, we only deal with the collisionless case in the derivation presented below. Recalling (4.3) gives a normalized version of the Vlasov equation as,

$$\frac{\partial \delta f_{1e}}{\partial t} + v\frac{\partial \delta f_{1e}}{\partial z} - E\frac{\partial \delta f_{1e}}{\partial v} = E\frac{\partial F_0}{\partial v}, \tag{F.1}$$

where we are modeling the electron plasma wave. At this point, a slight change from the V-Q framework occurs in that we couple to the normalized Poisson's law for the electric potential Φ, which is shown below (Heath et al., 2012),

$$-\nabla^2\Phi = 1 - \int_{-\infty}^{\infty} f_e \mathrm{d}v. \tag{F.2}$$

The major difference between this case and that of Section 3.1 is, of course, the Laplacian on Φ on the left hand side of (F.2). Writing (F.1) – (F.2) as a one dimensional system with $E = -\nabla\Phi$ gives the following, which is in exact agreement with Heath et al. (2012),

$$\frac{\partial \delta f_{1e}}{\partial t} + v\frac{\partial \delta f_{1e}}{\partial z} - E\frac{\partial \delta f_{1e}}{\partial v} = E\frac{\partial F_0}{\partial v}, \tag{F.3}$$

$$E = -\frac{\partial \Phi}{\partial z}, \tag{F.4}$$

$$\frac{\partial^2 \Phi}{\partial z^2} = \int_{-\infty}^{\infty} \delta f_{1e} \mathrm{d}v. \tag{F.5}$$

The major impact this change has, of course, is on terms involving the electrostatic field E. Computing this expression from Φ_{zz} using the classical electrodynamic expressions and a Fourier-Hermite ansatz of the form (3.17) for δf_{1e} gives,

$$\begin{aligned}
\Phi_{zz} &= \int_{-\infty}^{\infty} \delta f_{1e} \mathrm{d}v, \\
&= \int_{-\infty}^{\infty} \sum_{\substack{n=0, \\ j=-\infty}}^{\infty} a_{n,j}^{CE}(t) \phi_n(v) e^{ik_j z} \mathrm{d}v, \\
&= \sum_{\substack{n=0, \\ j=-\infty}}^{\infty} a_{n,j}^{CE}(t) e^{ik_j z} \int_{-\infty}^{\infty} \phi_n(v) \mathrm{d}v, \\
&= \sum_{\substack{n=0, \\ j=-\infty}}^{\infty} a_{n,j}^{CE}(t) e^{ik_j z} \int_{-\infty}^{\infty} \phi_n(v) \left(1\right) \mathrm{d}v, \\
&= \sum_{\substack{n=0, \\ j=-\infty}}^{\infty} a_{n,j}^{CE}(t) e^{ik_j z} \int_{-\infty}^{\infty} \phi_n(v) \left(\phi^0(v)\right) \mathrm{d}v, \\
&= \sum_{\substack{n=0, \\ j=-\infty}}^{\infty} a_{n,j}^{CE}(t) e^{ik_j z} \delta_{0,n}, \\
&= \sum_{j=-\infty}^{\infty} a_{0,j}^{CE}(t) e^{ik_j z}. \qquad \text{(F.6)}
\end{aligned}$$

Next, computing E yields,

$$\begin{aligned}
E &= -\frac{\partial \Phi}{\partial z}, \\
&= -\int \Phi_{zz} \mathrm{d}z, \\
&= -\int \sum_{j=-\infty}^{\infty} a_{0,j}^{CE}(t) e^{ik_j z} \mathrm{d}z, \\
&= -\sum_{j=-\infty}^{\infty} a_{0,j}^{CE}(t) \int e^{ik_j z} \mathrm{d}z, \\
&= -\sum_{j \neq 0} \frac{a_{0,j}^{CE}(t)}{ik_j} e^{ik_j z}, \qquad \text{(F.7)}
\end{aligned}$$

where we again neglect the $j = 0$ term as in Armstrong (1967) because it contains no spatial dependence. Note that the only difference between (3.19) and (F.7) is the fact that the ik_j term has moved from the numerator of (3.19) to the denominator of (F.7) because we now integrate to find E from Φ_{zz} as opposed to taking a derivative to

compute E from Φ as before. Rederiving the rest of the model gives the following results. First, inserting our Fourier-Hermite ansatz into the collisionless Vlasov-Poisson system gives,

$$\begin{aligned}\sum_{\substack{n=0\\j=-\infty}}^{\infty} \dot{a}_{n,j}^{CE}\phi_n e^{ik_jz} + i\sum_{\substack{n=0\\j=-\infty}}^{\infty} k_j a_{n,j}^{CE} v\phi_n e^{ik_jz} + \\ \sum_{h\neq 0}\frac{a_{0,h}^{CE}}{ik_h}e^{ik_hz}\sum_{\substack{n=0\\j=-\infty}}^{\infty} a_{n,j}^{CE}\phi_n' e^{ik_jz} &= EF_0', \\ \sum_{\substack{n=0\\j=-\infty}}^{\infty} \dot{a}_{n,j}^{CE}\phi_n e^{ik_jz} + i\sum_{\substack{n=0\\j=-\infty}}^{\infty} k_j a_{n,j}^{CE} v\phi_n e^{ik_jz} \\ + \sum_{\substack{n=0\\j=-\infty\\h\neq 0}}^{\infty} a_{n,j}^{CE}\frac{a_{0,h}^{CE}}{ik_h}\phi_n' e^{i(k_j+k_h)z} &= EF_0'. \end{aligned} \tag{F.8}$$

Next, utilizing Hermite recurrence, we recover,

$$\begin{aligned}\sum_{\substack{n=0\\j=-\infty\\h\neq 0}}^{\infty}\Bigg\{\dot{a}_{n,j}^{CE}\phi_n e^{ik_jz} + ik_j a_{n,j}^{CE}\left(\sqrt{\frac{n+1}{2}}\phi_{n+1} + \sqrt{\frac{n}{2}}\phi_{n-1}\right)e^{ik_jz} + \\ a_{n,j}^{CE}\frac{a_{0,h}^{CE}}{ik_h}\left[-\sqrt{2n+2}\phi_{n+1}\right]e^{i(k_j+k_h)z}\Bigg\} &= -2vEF_0. \end{aligned} \tag{F.9}$$

Projecting (F.9) onto a single Fourier mode yields,

$$\begin{aligned}\int_{-L_g}^{L_g}\sum_{\substack{n=0\\j=-\infty\\h\neq 0}}^{\infty}\Bigg\{\dot{a}_{n,j}^{CE}\phi_n e^{ik_jz} + ik_j a_{n,j}^{CE}\left(\sqrt{\frac{n+1}{2}}\phi_{n+1} + \sqrt{\frac{n}{2}}\phi_{n-1}\right)e^{ik_jz} + \\ a_{n,j}^{CE}\frac{a_{0,h}^{CE}}{ik_h}\left[-\sqrt{2n+2}\phi_{n+1}\right]e^{i(k_j+k_h)z}\Bigg\}e^{-ik_gz}\mathrm{d}z &= \int_{-L_g}^{L_g} -2vEF_0e^{-ik_gz}\mathrm{d}z, \end{aligned}$$

$$\begin{aligned}\int_{-L_g}^{L_g}\sum_{\substack{n=0\\j=-\infty\\h\neq 0}}^{\infty}\Bigg\{\dot{a}_{n,j}^{CE}\phi_n e^{i(k_j-k_g)z} + ik_j a_{n,j}^{CE}\left(\sqrt{\frac{n+1}{2}}\phi_{n+1} + \sqrt{\frac{n}{2}}\phi_{n-1}\right)e^{i(k_j-k_g)z} + \\ a_{n,j}^{CE}\frac{a_{0,h}^{CE}}{ik_h}\left[-\sqrt{2n+2}\phi_{n+1}\right]e^{i(k_j+k_h-k_g)z}\Bigg\}\mathrm{d}z &= \int_{-L_g}^{L_g} -2vEF_0e^{-ik_gz}\mathrm{d}z, \end{aligned}$$

$$\sum_{\substack{n=0\\ j\neq g}}^{\infty}\left\{\dot{a}^{CE}_{n,g}\phi_n + ik_g a^{CE}_{n,g}\left(\sqrt{\frac{n+1}{2}}\phi_{n+1}+\sqrt{\frac{n}{2}}\phi_{n-1}\right)+\right.$$
$$\left. a^{CE}_{n,j}\frac{a^{CE}_{0,g-j}}{ik_{g-j}}\left[-\sqrt{2n+2}\phi_{n+1}\right]\right\} = \frac{1}{2L_g}\int_{-L_g}^{L_g} -2vEF_0 e^{-ik_g z}\mathrm{d}z. \tag{F.10}$$

Projecting (F.10) onto a single Hermite mode ϕ^p and remembering that $i^{-1} = -i$ gives,

$$\int_{-\infty}^{\infty}\sum_{\substack{n=0\\ j\neq g}}^{\infty}\left\{\dot{a}^{CE}_{n,g}\phi_n \;+\; ik_g a^{CE}_{n,g}\left(\sqrt{\frac{n+1}{2}}\phi_{n+1}+\sqrt{\frac{n}{2}}\phi_{n-1}\right)-\right.$$
$$\left. ia_{n,j}\frac{a^{CE}_{0,g-j}}{k_{g-j}}\left[-\sqrt{2n+2}\phi_{n+1}\right]\right\}\phi^p\mathrm{d}v \;=\; \frac{1}{2L_g}\int_{-\infty}^{\infty}\int_{-L_g}^{L_g} -2vEF_0 e^{-ik_g z}\phi^p\mathrm{d}z\mathrm{d}v,$$

$$\dot{a}^{CE}_{p,g} + ik_g\left(a^{CE}_{p-1,g}\sqrt{\frac{p}{2}} \;+\; a^{CE}_{p+1,g}\sqrt{\frac{p+1}{2}}\right)+$$
$$i\sqrt{2p}\sum_{j\neq g}\frac{a^{CE}_{0,g-j}}{k_{g-j}}a^{CE}_{p-1,j} \;=\; \frac{1}{2L_g}\int_{-\infty}^{\infty}\int_{-L_g}^{L_g} -2vEF_0 e^{-ik_g z}\phi^p\mathrm{d}z\mathrm{d}v. \tag{F.11}$$

As in the fusion case, the classical analog (F.11) of (3.25) holds for all possible values of p and g, leading to an infinite nonlinear system. Recalculating the necessary vector definitions yields,

$$\mathbf{a^{CE}} = \{a^{CE}_{0,0},\ a^{CE}_{0,1},\ldots\ a^{CE}_{0,K},\ a^{CE}_{1,0},\ a^{CE}_{1,1},\ldots\ a^{CE}_{1,K},\ \ldots a^{CE}_{N,0},\ \ldots\ a^{CE}_{N,K}\}^T, \tag{F.12}$$

$$y^{CE}_{p,g} = -\frac{\sqrt{2p}}{\Delta k}\sum_{j\neq g}\frac{a^{CE}_{0,g-j}}{g-j}a^{CE}_{p-1,j}, \tag{F.13}$$

$$\mathbf{y^{CE}} = \{0,\ 0,\ldots\ 0,\ y^{CE}_{1,0},\ y^{CE}_{1,1},\ldots\ y^{CE}_{1,K},\ \ldots y^{CE}_{N,0},\ \ldots\ y^{CE}_{N,K}\}^T, \tag{F.14}$$

$$
\begin{aligned}
L_{p,g}^{CE} &= \frac{1}{2iL_g}\int_{-\infty}^{\infty}\int_{-L_g}^{L_g} -2vEF_0 e^{-ik_g z}\phi^p \mathrm{d}z\mathrm{d}v, \\
&= -\frac{1}{i}\int_{-\infty}^{\infty} -2vF_0\phi^p \sum_{j\neq 0}\frac{a_{0,j}^{CE}}{ik_j}\left(\frac{1}{2L_g}\int_{-L_g}^{L_g} e^{ik_j z}e^{-ik_g z}\mathrm{d}z\right)\mathrm{d}v, \\
&= \frac{2}{i^2}\int_{-\infty}^{\infty} v\phi_p \sum_{j\neq 0}\frac{a_{0,j}^{CE}}{k_j}\delta_{j,g}\mathrm{d}v, \\
&= -2\bar{\delta}_{g,0}\frac{a_{0,g}^{CE}}{k_g}\int_{-\infty}^{\infty} v\phi_p\phi^0\mathrm{d}v = \bar{\delta}_{g,0}\frac{a_{0,g}^{CE}}{k_g}\int_{-\infty}^{\infty}\left(\sqrt{\frac{p+1}{2}}\phi_{p+1}+\sqrt{\frac{p}{2}}\phi_{p-1}\right)\phi^0\mathrm{d}v, \\
&= -\frac{2}{\Delta k}\frac{a_{0,g}^{CE}}{g}\left(\sqrt{\frac{p+1}{2}}\delta_{p+1,0}+\sqrt{\frac{p}{2}}\delta_{p-1,0}\right)\bar{\delta}_{g,0}, \\
&= -\frac{2}{\Delta k}\frac{a_{0,g}^{CE}}{g}\left(\sqrt{\frac{p+1}{2}}\delta_{p,-1}+\sqrt{\frac{p}{2}}\delta_{p,1}\right)\bar{\delta}_{g,0}, \\
&= -\frac{2}{\Delta k}\frac{a_{0,g}^{CE}}{g}\sqrt{\frac{1}{2}}\delta_{p,1}\bar{\delta}_{g,0} = -\frac{\sqrt{2}}{\Delta k}\frac{a_{0,g}^{CE}}{g}\delta_{p,1}\bar{\delta}_{g,0}.
\end{aligned} \tag{F.15}
$$

Again, $L_{p,g}^{CE} \neq 0$ only if $p = 1$ and $g \neq 0$, which gives,

$$
\mathbf{L^{CE}} = \{0,\ 0, ..0,\ L_{1,1}^{CE}, ...\ L_{1,K}^{CE},\ 0, ...\ 0\}^T, \tag{F.16}
$$

where only elements $K+3$ through $2K+2$ of $\mathbf{L}$ are nonzero as a result of the $\bar{\delta}_{g,0}$ and $\delta_{p,1}$ terms. We can again rewrite (F.11) as below,

$$
\dot{a}_{p,g}^{CE} = -ig\Delta k\left(a_{p-1,g}^{CE}\sqrt{\frac{p}{2}}+a_{p+1,g}^{CE}\sqrt{\frac{p+1}{2}}\right)+iy_{p,g}^{CE}+iL_{p,g}^{CE}, \tag{F.17}
$$

as well as its analogous matrix-vector formulation,

$$
\dot{\mathbf{a}}^{CE} = i(\mathbf{M}\mathbf{a^{CE}}+\mathbf{y^{CE}}+\mathbf{L^{CE}}). \tag{F.18}
$$

These adjustments to the collisionless part of the V-Q system will allow us to validate our code using known results from the V-P system with classical electrostatics before making relatively minor changes to implement the version that is most valid for the electrostatic coupling appropriate for quasineutral plasmas.

Appendix G

Additional V-P Results

G.1 Recurrence Time Results for First Fourier Mode Activation from Section 4.2.3

As mentioned in Section 4.2.3, we see from Fig. G.1 that the half-recurrence time for activation of the first Fourier mode is just under 20 normalized time units. We use this conclusion to investigate how the behavior of the distribution function changes as Landau damping begins to interact with collisional damping.

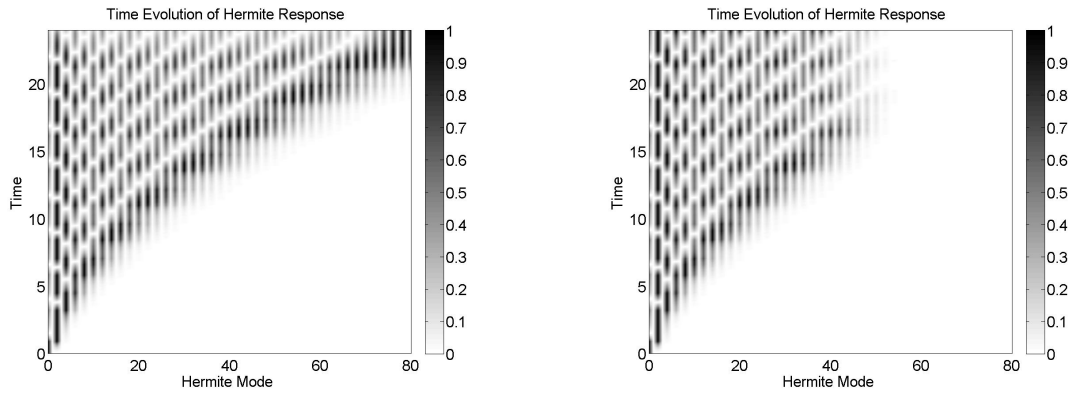

(a) Collisionless

(b) Hypercollisional

Figure G.1: First mode Hermite response for collisionless and hypercollisional cases.

G.2 Dougherty Collision Results

The following results were obtained by running the linear V-P code with Dougherty collisions with the same parameter settings stated in Section 4.2.3. Note that, as expected, the Dougherty collision operator severely damps all but the first few Hermite modes of the distribution function and thus suppresses much of the Landau damping

phenomenon. The results in Figs. (G.2) and (G.3) demonstrate this reality quite clearly, and thus illustrate the need for hypercollisionality when modeling Landau damping numerically.

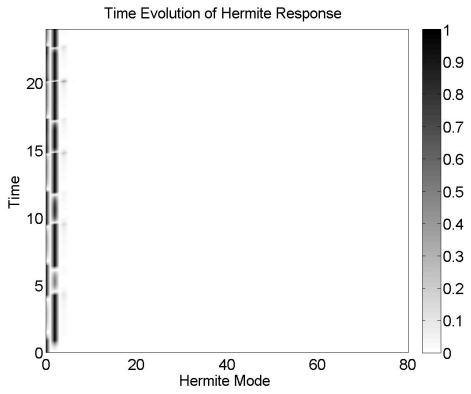

Figure G.2: Linear V-P response in Hermite space with Dougherty collisions.

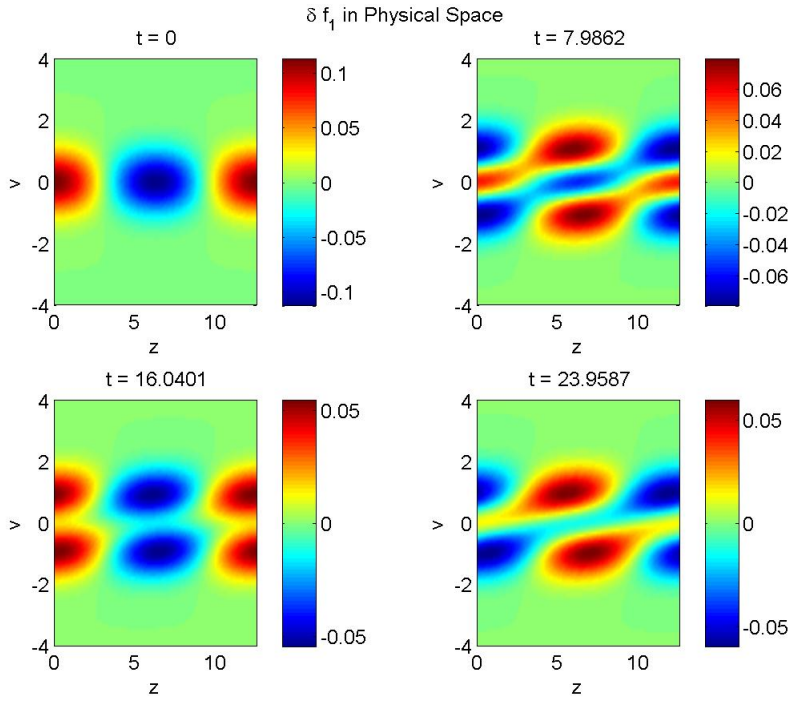

Figure G.3: Time evolution of V-P δf_1 with Dougherty collisions.

G.3 Sample Time Evolution Plot of the Largest N^{th} Hermite Coefficient

In this section we present Fig. G.4, which illustrates the time evolution of the maximum Fourier-Hermite coefficient on the highest Hermite mode in time. We use plots such as this throughout this study to ensure that the Fourier-Hermite coefficients we neglect through truncation of the Hermite spectrum are indeed exponentially small. In this case, we see that no coefficient on the N^{th} Hermite mode ever has a magnitude greater than $O(10^{-8})$, meaning that our truncation of the Hermite spectrum at the N^{th} mode should not cause us to ignore any important behavior in Hermite modes higher than N.

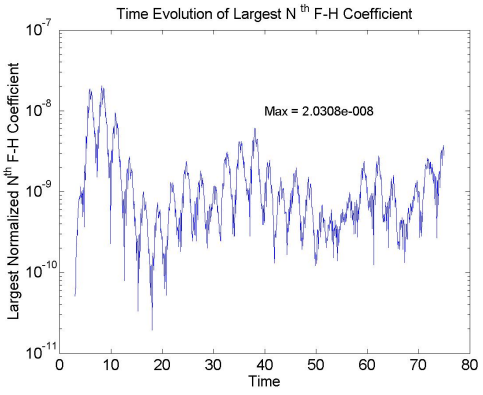

Figure G.4: Nonlinear time evolution of largest V-P N^{th} Hermite coefficient.

Appendix H

Additional Forced V-Q Derivations and Results

This appendix contains an additional set of detailed calculations for the forcing term and a set of results illustrating the time evolution of the Fourier modal electric fields for each forced nonlinear V-Q simulation in Chapter 6.

H.1 Detailed Calculation of $F_{p,g}$ from (6.5)

$$
\begin{aligned}
F_{p,g} &= \frac{1}{2L_g}\int_{-\infty}^{\infty}\int_{-L_g}^{L_g} F\phi^p e^{-ik_g z}\mathrm{d}z\mathrm{d}v, \\
&= \bar{\nu}\int_{-\infty}^{\infty}\sum_{n=0}^{\infty}\left(a_{n,g}\phi_n - \sqrt{2n+2}a_{n,g}\left[\sqrt{\frac{n+2}{2}}\phi_{n+2} + \sqrt{\frac{n+1}{2}}\phi_n\right] + \sqrt{2}\bar{U}_g\phi_1\right)\phi^p\mathrm{d}v, \\
&= \bar{\nu}\left(a_{p,g} - \sqrt{2p-2}\sqrt{\frac{p}{2}}a_{p-2,g} - \sqrt{2p+2}\sqrt{\frac{p+1}{2}}a_{p,g} + \sqrt{2}\bar{U}_g\delta_{p,1}\right), \\
&= \bar{\nu}\left(a_{p,g} - \left[\sqrt{p^2-p}\right]a_{p-2,g} - [p+1]a_{p,g} + \sqrt{2}\bar{U}_g\delta_{p,1}\right), \\
&= \bar{\nu}\left(-pa_{p,g} - \left[\sqrt{p^2-p}\right]a_{p-2,g} + \sqrt{2}\bar{U}_g\delta_{p,1}\right). \qquad \text{(H.1)}
\end{aligned}
$$

H.2 Modal Electric Fields for White Noise Forcing

We here present the time evolution of the Fourier modal electric fields for white noise forcing in Fig. H.1. Note that each mode of the electric field appears to decay until the forcing patterns with which its interacts dominate in the large time limit.

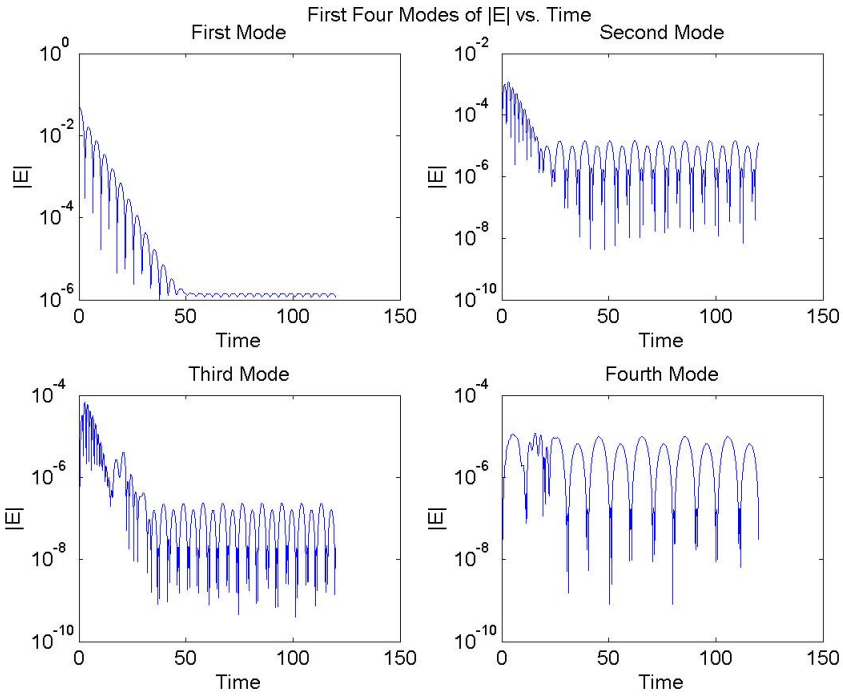

Figure H.1: Evolution of V-Q Fourier modal $|E|$ under white noise forcing.

H.3 Modal Electric Fields for Resonant Forcing

In this section, we present the time evolution of the Fourier modal electric field for resonant forcing in Fig. H.2. As expected, we see a particularly high-amplitude response in the first mode, which undergoes direct resonant forcing. Note also that each mode of the electric field generally decays to the point at which interaction with the resonant forcing mode comes to dominate each modal response.

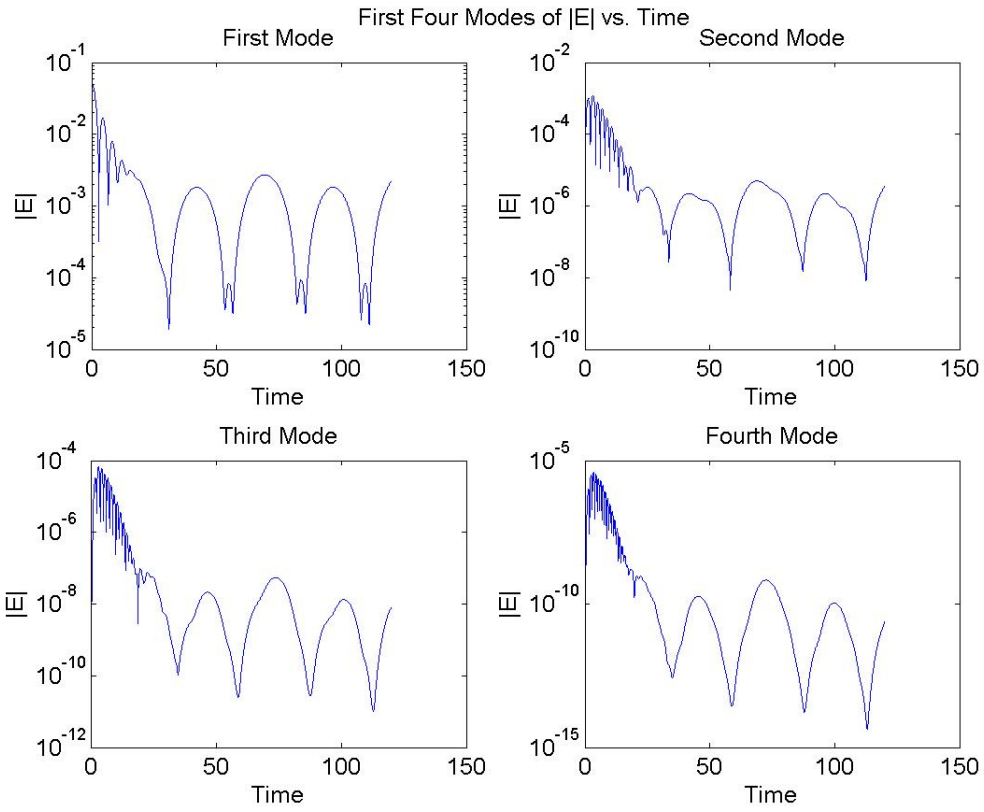

Figure H.2: Evolution of V-Q Fourier modal $|E|$ under resonant forcing.

H.4 Modal Electric Fields for Resonant White Noise Forcing

In this section, we present the time evolution of the Fourier modal electric field for resonant white noise forcing in Fig. H.3. Note that we see a combination of the two previous responses wherein the first mode, which is forced at resonance, appears to undergo a relatively high amplitude response after initial decay while the higher modes decay until the relevant white noise signal dominates the long term dynamics. This marks an important difference from the resonant forcing case in which all modes are dominated by high-amplitude interaction with the resonant mode.

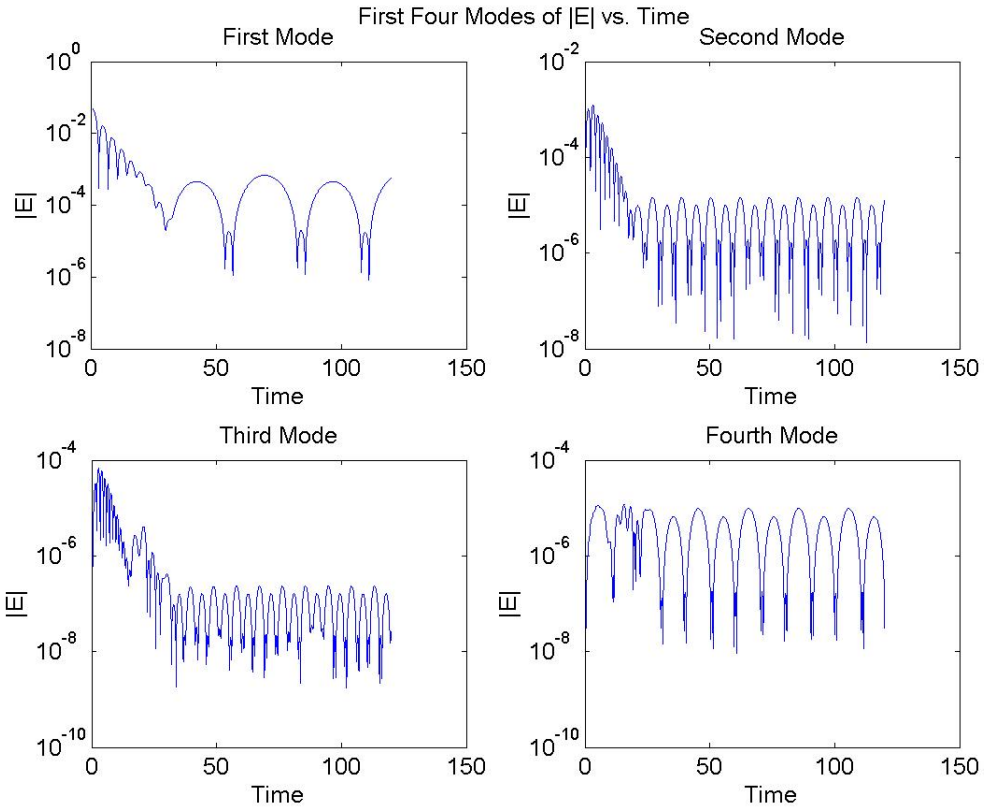

Figure H.3: Evolution of V-Q Fourier modal $|E|$ under resonant white noise forcing.

Bibliography

Abel, I.G., Plunk, G. G., Wang, E., Barnes, M. Cowley, S. C., Dorland, W., Schekochihin, A. A., 2012. Multiscale Gyrokinetics for Rotating Tokamak Plasmas I: Fluctuations, Transport and Energy Flows. Reports of Progress in Physics, Submitted.

Abramowitz, M., Stegun, I.A. Handbook of Mathematical Functions. Dover, New York, 1972.

Armstrong, T. P., 1967. Numerical Studies of the Nonlinear Vlasov Equation. Physics of Fluids 10, 1269-1280.

Belli, E.A., Hammett, G.W., 2005. A Numerical Instability in an ADI Algorithm for Gyrokinetics. Computer Physics Communications 172, 119-132.

Bhatnagar, P.L., Gross, E.P., Krook, M., 1954. A Model for Collision Processes in Gases. I. Small Amplitude Processes in Charged and Neutral One-Component Systems. Physical Review 94, 511-525.

Butcher, J.C., 2000. Numerical Methods for Ordinary Differential Equations in the 20th Century. Journal of Computational and Applied Mathematics 125, 1-29.

Chen, F. F. Introduction to Plasma Physics and Controlled Fusion, 2nd Edition. Volume 1, Plasma Physics. Springer, New York, 1984.

Dendy, R. Plasma Physics: An Introductory Course. Cambridge University Press, Cambridge, 1993.

Dimits, A. M., Bateman, G., Beer, M. A., Cohen, B. I., Dorland, W., Hammett, G. W., Kim, C., Kinsey, J. E., Kotschenreuther, M., Kritz, A. H., Lao, L. L., Mandrekas, J., Nevins, W. M., Parker, S. E., Redd, A. J., Schumaker, D. E., Sydora, R., Weiland, J., 2000. Comparisons and Physics Basis of Tokamak Transport Models and Turbulence Simulations, I. Theory. Physics of Plasmas 7, 969-983.

Dougherty, J.P., 1964. Model Fokker-Planck Equation for a Plasma and its Solution, Physics of Fluids 7, 1788-1799.

Durran, D.R., 1991. The Third-Order Adams-Bashforth Method: An Attractive Alternative to Leapfrog Time Differencing. Monthly Weather Review 119, 702-720.

Fried, B.D., Conte, S.D. The Plasma Dispersion Function. Academic Press, New York, 1961.

Frieman, E. A., Chen, L., 1982. Nonlinear Gyrokinetic Equations for Low Frequency Electromagnetic Waves in General Plasma Equilibria. Physics of Fluids 25, 502-508.

Ganesh, R., Lee, W. W., Ethier, S., Manickam, J., 2010. Properties of Freely Decaynig and Driven Turbulence of Fusion Plasmas Using Gyrokinetic Particle Simulation. Journal of Plasma Fusion and Research 9, 517-522.

Grad, H.,1949. On the Kinetic Theory of Rarefied Gases. Communications on Pure and Applied Mathematics 2, 331-407.

Griffiths, D. J. Introduction to Electrodynamics, 3rd Edition. Prentiss Hall, Upper Saddle River, 1999.

Hae-Kwan, D., 2011. Quasineutral Limit of the Vlasov-Poisson System with Massless Electrons. Communications in Partial Differential Equations 36, 1385-1425.

Heath, R. E., Gamba, I. M., Morrison, P. J., Michler, C., 2012. Journal of Computational Physics 231, 1140-1174.

Hou, T. Y., Li, R., 2007. Computing Nearly Singular Solutions Using Pseudo-Spectral Methods. Journal of Computational Physics 226, 379-397.

Howes, G. G., Cowley, S. C., Dorland, W., Hammett, G. W., Quatert, E., Schekochihin, A. A., 2006. Astrophysical Gyrokinetics: Basic Equations and Linear Theory. The Astrophysical Journal 651, 590-614.

Huba, J.D. NRL Plasma Formulary. Naval Research Laboratory, Washington, D.C., 2009.

Joyce, G., Knorr, G., Meier, K., 1971. Numerical Integration Methods of the Vlasov Equation. Journal of Computational Physics 8, 53-63.

Knorr, G., Shoucri, M., 1974. Plasma Simulation as Eigenvalue Problem. Journal of Computational Physics 14, 1-7.

Krommes, J.A., 2012. The Gyrokinetic Description of Microturbulence in Magnetized Plasmas. Annual Review of Fluid Mechanics 44, 175-201.

Landau, L.D., 1936. The Transport Equation in the Case of Coulomb Interactions. Journal of Physics (U.S.S.R.) 10. Reproduced in Collected Papers of L.D. Landau, Editor D. ter Haar, Pergamon Press, Oxford, 1981, 163-170.

Landau, L.V., 1946. On the Vibration of the Electronic Plasma. Journal of Physics (USSR) 10. Reproduced in Collected Papers of L.D. Landau, Editor D. ter Haar, Pergamon Press, Oxford, 1981, 445-460.

Lénard, A., Bernstein, I.B., 1958. Plasma Oscillations with Diffusion in Velocity Space, Physical Review 112, 1456-1459.

Liboff, R.L. Kinetic Theory: Classical, Quantum, and Relativistic Descriptions, 3rd Edition. Springer, New York, 2003.

Lifshitz, E. M., Pitaevskii, L. P. Physical Kinetics, 3rd Edition. Course of Theoretical Physics, Volume 10. Edited by L.D. Landau and E.M. Lifshitz. Butterworth-Heinemann, New York, 1980.

Littlejohn, R.G., 1983. Variational Principles of Guiding Centre Motion. Journal of Plasma Physics 29, 111-125.

Miura, Y., et al., 2003. Study of Improved Confinement Modes with Edge and/or Internal Transport Barriers on the Japan Atomic Energy Research Institute Tokamak-60 Upgrade (JT-60U). Physics of Plasmas 10, 1809-1815.

Mouhot, C., Villani, C., 2011. On Landau Damping. Acta Mathematica 207, 29-201.

Ng., C.S., Bhattacharjee, A., Skiff, F., 2006. Weakly Collisional Landau Damping and Three-Dimensional Bernstein-Greene-Kruskal Modes: New Results on Old Problems. Physics of Plasmas 13, 055903-1 - 055903-9.

Numata, R., Howes, G. G., Tatsuno, T., Barnes, M., Dorland, W., 2010. AstroGK: Astrophysical Gyrokinetics Code. Journal of Computational Physics 229, 9347-9372.

Parker, J. T., Dellar, P. J., 2012. Hermite Expansions with Hypercollisionality for Velocity Space Degrees of Freedom in Ion-Temperature-Gradient Driven Instabilities. Journal of Computational Physics, In Preparation.

Passot, T., Pouqet, A., 1988. Hyperviscosity for Compressible Flows Using Spectral Methods. Journal of Computational Physics 75, 300-313.

Platzman, P.M., Buchsbaum, S.J., 1961. Effect of Collisions on the Landau Damping of Plasma Oscillations. Physics of Fluids 4, 1288-1292.

Pueschel, M.J., Dannert, T., Jenko, F., 2010. On the Role of Numerical Dissipation in Gyrokinetic Vlasov Simulations of Plasma Microturbulence. Computer Physics Communications 181, 1428-1437.

Schroeder, D.V. An Introduction to Thermal Physics. Addison Wesley, New York, 2000.

Shoucri, M.M., Gagné, R.R.J., 1977. Numerical Solution of a Two-Dimensional Vlasov Equation. Journal of Computational Physics 25, 94-103.

Siminos, E., Benisti, D., Gremillet, L., 2011. Stability of Nonlinear Vlasov-Poisson Equilibria Through Spectral Deformation and Fourier-Hermite Expansion. Physical Review E 83, 056402-1 - 056402-13.

Thomas, A.G.R., Tzoufras, M., Robinson, A.P.L., Kingham, R.J., Ridgers, C.P., Sherlock, M., Bell, A.R., 2012. A Review of Vlasov-Fokker-Planck Numerical Modeling of Inertial Confinement Fusion Plasma. Journal of Computational Physics 231, 1051-1079.

Wesson, J. Tokamaks, 4th Edition. Oxford University Press, Oxford, 1997.

Weisstein, E. W., 2012. "Hermite Polynomial." Wolfram MathWorld. Retrieved from http://mathworld.wolfram.com/HermitePolynomial.html. 28 June 2012.

Wiedeman, J.A.C., 1994. Computation of the Complex Error Function. SIAM Journal of Numerical Analysis 31, 1497-1518.